# Cavity-enhanced emission from Germanium Vacancy centers in Diamond

Rasmus Høy Jensen

A thesis submitted in partial fulfillment of the
requirements for the PhD degree in Physics


Section for Quantum Physics and Information Technology
Department of Physics
Technical University of Denmark

April 2019

Main supervisor:

Professor Ulrik Lund Andersen

Supervisor:

Associate Professor Alexander Huck

PhD committee:

Professor Jesper Mørk
Professor Dr. Christoph Becher
Professor Dr. David Hunger

# Abstract

The unique correlations in quantum systems, i.e. superposition and entanglement, enable quantum technologies to outperform classical technologies. Quantum networks is a quantum technology in fast development with many promising applications. An essential building block in a quantum network is the interface between matter nodes and quantum channels. A color center in diamond coupled to a micro-cavity is a promising route to achieve an efficient interface.

In this thesis we investigate the coupling of a single germanium vacancy (GeV) center to a Fabry-Pérot optical micro-cavity at room temperature. The Fabry-Pérot optical micro-cavity was formed by a macroscopic flat mirror and a fiber-based concave microscopic mirror. The concave mirror was created on the end-facet of a fiber with short high power laser pulses from a $CO_2$-laser. High qulity dielectric coating allowed us to achieve a finesse of 11,000 with a $\sim$1 µm thin diamond membrane incorporated in the cavity. We achieved a cavity length of only a few µm and a small mode volume $V = 2.7$µm, which was essential for good coupling between the GeV center and the optical cavity mode.

By studying the same GeV center in a confocal microscope setup, i.e. outside of the micro-cavity, and in the micro-cavity setup, we were able to measure an improved optical coherence of the GeV emission in the cavity. We determined an enhancement of the spectral density by a factor of $\sim$15. Furthermore, we determined the emission efficiency into the cavity mode $\beta$ and compared it with the theoretical modelling. From the theoretical modelling, we predict the expected Purcell factor $F_p = 200$ for the zero phonon line in future experiments at cryogenic temperatures.

Going to cryogenic temperatures is necessary to achieve efficient spin-photon interfaces. This work provides valuable information for realizing efficient spin-photon interfaces, which is critical for the practical implementation of a quantum network.

# Dansk Resumé

Kvantesystemers unikke korrelationer, dvs. superposition og entanglement, gør kvanteteknologier i stand til at udkonkurrere visse af de klassiske teknologier. Kvantenetværk er en kvanteteknologi under hurtig udvikling og har mange lovende anvendelsesmuligheder. En essentiel bestanddel af et kvantenetværk er et interface mellem faststof kvantebits og fotoniske kvantekanaler. En lovende metode til at opnå et sådan effektiv interface er ved at anvende et farvecenter i en diamant, som er koblet til en mikrokavitet.

I denne Ph.d.-afhandling undersøger vi koblingen mellem et enkelt germanium vacancy (GeV) center og en optisk Fabry-Pérot mikrokavitet ved stuetemperatur. Den optiske Fabry-Pérot mikrokavitet bestod af et makroskopisk fladt spejl og et fiberbaseret mikroskopisk konkavt spejl. Det konkave spejl blev formet ved at skyde korte laserpulser med høj effekt fra en $CO_2$ laser ind på enden af en fiber. Dielektriske coating af høj kvalitet muliggjorde, at vi kunne opnå en finesse på 11.000 med en $\sim$1 µm tynd diamantmembran i kaviteten. Vi var i stand til at opnå en kavitetslængde på nogle få µm samt et lille mode volumen på $V = 2.7\mu m$, hvilket markant var essentielt for at opnå god kobling mellem GeV centeret og den optiske kavitetsmode.

Ved at studere det samme GeV center i en konfokal mikroskop dvs. udenfor kaviteten, samt i en mikrokavitets var vi i stand til at måle en forbedret optisk kohærents af emissionen fra GeV centeret i kaviteten. Vi kunne måle en forbedring af den spektrale tæthed med en faktor på $\sim$15. Vi kunne yderligere bestemme effektiviteten af emissionen til kavitetsmoden $\beta$ og sammenligne denne med teoretiske beregninger. Ud fra de teoretiske beregninger er vi i stand til at forudsige Purcell faktoren $F_p = 200$ for zero phonon linen ved fremtidige eksperimenter ved kryogene temperaturer.

I fremtiden er det nødvendigt at udføre lignende eksperimenter ved kryogene temperaturer for at opnå et effektiv spin-foton interface. Arbejdet i denne Ph.d.-afhandling bidrager med værdifuld information til at realisere effektive spin-foton interfaces, hvilket er essentielt for at implementere kvantenetværk i praksis.

## Acknowledgements

During my PhD time I have enjoyed to collaborate with and learn from the incredibly smart and dedicated people from the groups of Lillian Childress and Ulrik L. Andersen. First, I would like to thank my main supervisor Ulrik L. Andersen, whose hard work and ambitious goals have been an inspiration to me. Thank you to Ulrik for giving me the opportunity to do a PhD within his group and for the full support along the way. Next, I would like to thank my supervisor Alexander Huck for thoughtful and encouraging guidance during the entire three years of my PhD.

I would like to thank Erika Janitz from McGill University, Canada. It has been a lot of fun to work with her and very encouraging to share the challenges of the project presented in this thesis with her. My stay at McGill University was a very pleasant experience and I undoubtedly learned a lot from working together with Erika, Yannik and Lillian.

Thank you to the optical diamond team at DTU: Olivier, Maxime, Mads, Yuriy and Ilya with whom I have shared countless hours in the lab and enjoyed cheerful lunches. It has been a great pleasure to work with you.

Thank you to Ilya and Haitham for providing useful code to the simulations in this work. Thank you to all the people in the QPIT group, in which there now are too many people to mention by name.

Special thanks to my friends and family for their support during the past three years. Thank you to Anders for advice in the writing phase. Finally, I would like to thank my wife, Mette, for her dedicated and invaluable support.

# Contents

# List of Abbreviations

| | |
|---|---|
| AFM | atomic force microscope |
| AL | air-like |
| APD | avalanche photo diode |
| CVD | chemical vapor deposition |
| CW | continuous wave |
| DBR | distributed Bragg reflectors |
| DL | diamond-like |
| DM | dichoric mirror |
| FIB | focused ion beam |
| FWHM | full width half maximum |
| GeV | germanium vacancy |
| HR | high reflective |
| HTHP | high temperature high pressure |
| MM | multi mode |
| NA | numerical aperture |
| NI | National Instruments |
| NV | nitrogen vacancy |
| PD | photodetector |
| PSB | phonon side band |
| PSD | peak spectral density |
| pzt | piezo |
| QE | quantum emitter |
| RMS | root mean square |
| ROC | radius of curvature for a spherical mirror |
| SB | sideband |
| SD | spectral density |
| SEM | scanning electron microscope |
| SiV | silicon vacancy |
| SM | single mode |
| SNR | signal to noise ratio |
| TLP | tunable long pass |
| TSP | tunable short pass |
| ZPL | zero phonon line |

# Chapter 1

# Introduction

## 1.1 Motivation

Quantum technology has the potential to revolutionize and transform our lives and societies by utilizing quantum properties to outperform classical technologies. To further the development of quantum technology, the European Union launched the Quantum Flagship project as the third large-scale research initiative (1 billion euros, 10+ years, 5000+ researchers) following the Graphene Flagship and the Human Brain Project [1].

Superposition and entanglement are two quantum properties which the quantum technology utilizes to solve problems unattainable by classical technology. One quantum information technology is the quantum network [2–4]. Quantum networks facilitate the transmission of quantum information and have many promising applications, such as:

- Distributed quantum computing [5].
- Long distance secure communication [6].
- Synchronizing atomic clocks [7].

In classical networks, such as the internet, the bit (0 and 1) is the unit of information. In a quantum network the unit of information is the quantum bit (qubit - a superposition of 0 and 1). The transmission of qubits enables entanglement distribution and teleportation of quantum states between nodes, which is critical for the applications mentioned above.

The most common proposals for a quantum network consist of matter nodes connected by photonic quantum channels. The matter nodes consist of one or a register of qubits which can store and process quantum information. The quantum channels consist of light particles (photons), which can distribute quantum information over large distances fast. The delicate nature of a quantum network enforces strict requirements on the properties of the matter node material, the quantum channel and the interface between them.

Solid state matter nodes are attractive since they are highly scalable and allow for integration into nanofabricated devices [8]. Spins in diamond color centers have been proposed as candidates for solid state matter nodes. A color center is an optical active defect in the diamond crystal lattice. The nitrogen vacancy (NV) center is the most

well studied color center, but other color centers, such as the silicon vacancy (SiV) center and the germanium vacancy (GeV) center are also being studied.

Scalability, initialization of pure states, coherent state manipulation, long coherence time and high fidelity readout are all essential properties of a qubit for quantum information processing at the nodes [9]. The spins in color centers fulfill all these requirements. The spins can be initialized in the spin ground state by optical pumping. Further, optical readout of the spin state is possible due to spin dependent fluorescence. Coherent manipulation of the spin states can be done with mircowaves [10]. The NV electron and nuclear spins have a very long coherence time, which is the time scale that the spins preserve their quantum information [11]. Importantly, the coherence times are orders of magnitudes longer than the coherent state manipulation times.

Interfacing the nodes with the quantum channels is critical to distribute qubits in the quantum network. For the NV center, spin-photon entanglement has already been demonstrated at cryogenic temperatures [12, 13]. Impressively, the NV center has been used to demonstrate the first loop-hole free Bell tests [14]. However, these measurements were taken over several weeks due to poor optical properties of the NV center. The optical properties of the NV center limit the entanglement distribution rate, which is an essensiental protocol in a quantum network. The entanglement distribution rate is currently limited to tens of hertz [15] due to low flux of identical photons from the NV centers zero phonon line (ZPL). Four factors can explain the low photon flux: relatively long excited state lifetime (12 ns), low branching ratio into the ZPL (3%), spectral diffusion (due to a permanent electrical dipole) and emission into undesirable spatial optical modes.

The optical properties of the SiV center and GeV center have sparked a lot of interest due to their strong ZPL transition compared to the NV center. The electron spin system in the SiV center has recently also shown a 13 ms long coherence time at mK temperature [16], which means that the SiV center is also a candidate for nodes in a network. Currently, the coherence time of the electron spin associated with the GeV center is measured to be $\sim$20 ns at 2 K limited by lattice vibrations [17].

The optical properties of the color centers can be enhanced by changing the photonic environment. This can be achieved by placing the color centers in a small mode volume optical cavity with a high quality factor [18]. The ZPL emission rate can be enhanced via the Purcell effect [19], which means that the overall flux of photons from the emitter increases and a larger fraction of the emitted light is in the ZPL. The light emitted into the cavity mode can be guided in a confined spatial mode and conveniently directed into a detector.

Coupling a single NV center to a micro-cavity was first accomplished using a diamond ring resonator, where a Purcell enhancement factor of 10 of the ZPL was measured [20]. A lot of work has also been put into building integrated photonic crystal nanocavities [21–23]. A Purcell enhancement factor of $\sim$70 has been measured for an NV center, however, spectral diffusion of the NV center increases to several GHz in such a nanofabricated device, which limits the applications of the device. In the future, spectral diffusion might be reduced in fabricated devices by feedback techniques [24] and fabrication techniques [25].

Tunable open Fabry-Pérot optical micro-cavities can be used to enhance the optical properties of color centers. The name micro-cavity refers to the microscale mode volume of the electrical field inside the cavity. Compared to the photonic crystal cavity, this approach allows us to use minimally processed diamonds reducing spectral diffusion and linewidth broadening. Further, the open cavity design allows for *in situ* spectral and spatial tuning leading to good coupling between the cavity mode and the color center. A higher quality factor can be achieved using state of the art dielectric coating, at the cost of higher mode volume than the integrated nanocavites. The cavity modes are Gaussian, which allows for higher mode matching to a propagating mode, e.g. in a fiber, leading to high photon flux going into the detector. A lot of work has already been done in the coupling of Fabry-Pérot micro-cavities to color centers in diamond, which is described in the following section.

## 1.2 State-of-the-art

During the past years, different approaches have been used to couple color center to Fabry-Pérot based micro-cavities. These cavities consist of at least one concave mirror to ensure a stable cavity mode. The mirrors are typically coated onto a fiber tip or a bulk substrate. An important parameter for open tunable cavities is the finesse $F$, which describes the average number of round trips a photon makes inside the cavity before it is lost. The mode volume $V$ determines the interaction strength of the cavity mode and the color center and it is important to have a small mode volume to achieve a high coupling rate to the cavity mode.

The first open and tunable micro-cavities used one or two coated fiber mirrors [26, 27] to make a stable cavity with $F \sim$1000 and mode volumes of 600 $\mu m^3$. Focused ion beam (FIB) milling was later used to machine concave mirrrors into bulk substrates achieving mode volumes of only 2.2 $\mu m^3$ [28] and a Finesse around 500. Later, concave dimples were $CO_2$ laser machined on the fiber end-facet mirror achieving $F \sim$40000 and mode volumens of 3 $\mu m^3$ [29, 30].

The NV center was the first color center to be coupled to a fiber based micro-cavity. Nanodiamonds containing single NV centers were studied in fiber cavities with $F \sim 1000$ and a mode volume of 6 $\mu m^3$ [31]. Due to the broadband emission from the NV center no Purcell enhancement factor was observed. However, an increase in spectral density due to phonon assisted emission (also known as cavity funnelling) was shown, which can be important for room temperature single photon sources. Enhancement of the spectral density of ∼300 with an ensemble of NV centers was also shown in a fiber cavity with a mode volume of 16 $\mu m^3$ [32].

At cryogenic temperature, a single NV center in a nanodiamond coupled to a microcavity showed a Purcell enhancement factor of the ZPL ∼6 [33]. In a room temperature experiment for a microcavity with metallic mirrors a broadband Purcell enhancement factor of 2 for a single NV center in a nanodiamond was shown [34]. Also, SiV center has been coupled to mircocavities with a mode volume of 1.4 $\mu m^3$ and a finesse $\sim$ 4000 at room temperature yielding a Purcell enhancement factor of ∼10 [35].

All of the experiments listed above use nanodiamonds, which are good for achieving very small mode volumes and excellent for applications like a single photon gun at room temperature. However, color centers in nano-sized diamonds undergo large spectral diffusion due to charge traps at the surface [36]. Using bulk-like color centers is therefore necessary for efficient spin-photon interfaces. Hence, a lot of effort is put into making high quality diamond membranes that can be incorporated into micro-cavities. The surface of such membranes need to be ultra smooth since scattering losses are devastating for high finesse cavities.

Such a high quality diamond membrane was demonstrated in a fiber-based microcavity with a finesse of 17000 [37]. Impressivly, a Purcell enhancement of $\sim 40$ for the ZPL was measured for a single NV center in a diamond membrane at low temperature [38]. An ensemble of SiV centers has been studied in thin diamond membranes ($\sim$200 nm) [39].

Other interesting steps towards using an open micro-cavity as interface between the spin in color centers are the inclusion of microwave antennas for coherent spin manipulation [40] and active cavity length stabilization [41–43].

## 1.3 Thesis outline

The purpose of this thesis is to characterize the interaction of a single GeV center in a diamond membrane with an optical micro-cavity at room temperature. As evidence of the cavity coupling we aim to observe an enhancement of the spectral density of the GeV emission. Furthermore, we aim to quantify the cavity coupling by measuring the $\beta$-factor, which is the efficiency of the GeV emission into the cavity mode. The $\beta$-factor is measured by studying the emission of a single GeV center in two different optical environments. First, a GeV center is characterized in free space, i.e. out of the micro-cavity, using a confocal microscope. Second, by building a fiber based micro-cavity we study the emission of the GeV center in the micro-cavity. The emission coherence and emission rate from the GeV center are compared for the GeV center in and out of the micro-cavity.
This study enables us to predict the expected Purcell enhancement for a future experiment at cryogenic temperature.

The work presented in this thesis was a collaboration between the group of Lillian Childress at McGill University in Canada and the group of Ulrik L. Andersen at the Technical University of Denmark (DTU). The author of this PhD thesis visited McGill University during this project.

The thesis is divided into the following chapters:

**Chapter 2** provides the theoretical framework for the experiments in this thesis. First, the color centers in diamond are described. Second, the techniques to describe the optical cavity and the modes in the cavity are presented. Third, the interaction of the quantum emitter and an optical cavity is described in the framework of cavity electrodynamics. Lastly, the dipole emission from a GeV center on a dielectric mirror is studied

**Chapter 3** gives detailed explanation of the experimental setups of the confocal microscope and of the micro-cavity setup. The fabrication techniques of the

cavity mirrors and diamond membrane are also presented.

**Chapter 4** presents the experimental results of this work. We study a single GeV center in a diamond membrane both in free space and in a micro-cavity. We compare the emission rates for the two scenarios, and compare the results with theory.

**Chapter 5** concludes on the work presented in this thesis.

# Chapter 2

# Theory

In this chapter the background theory and concepts to explain our experiments are introduced. First, color centers in diamond are described, which is followed by an explanation of optical cavities. Lastly, the interaction between the cavity and color centers are described.

## 2.1 Color centers in diamond

Some of the lattice defects in a diamond crystal lattice are optically active. Since the optical transition is spin dependent, the color centers can act as a spin photon interface. In the following, we will describe two important color centers in diamond. First, the nitrogen vacancy (NV) center is described since it is very well known and already has been coupled to optical micro-cavities. Therefore, the NV center is a useful reference for other color centers. Next, the germanium vacancy (GeV) center is described, which is the color center we have used in our experiments.

### 2.1.1 The NV center

The most famous color center in diamond is the NV center. Long spin coherence times at room temperature and optically initialization to the ground spin state in solid state platforms are the main properties that make the NV center very attractive for quantum information technology [44] and as a magnetic sensor [45–47].

#### Atomic structure of the NV center

The diamond lattice is formed by carbon atoms. Carbon atoms in diamond have $sp^3$-hybridized bonds with four neighbouring carbon atoms, which give the tetrahedral molecular geometry. The NV center is a lattice defect and it is formed by removing two adjacent carbon atoms and inserting a substitutional nitrogen atom, see figure 2.1. The NV center has $C_{3V}$ symmetry and the NV center's symmetry axis lies along the [111] axis, which means that there are four possible crystal orientations of the NV center in diamond.

There are two common charge states of the NV center; the neutral $NV^0$ state and the negative $NV^{-1}$ state. In this work only the $NV^{-1}$ is discussed.

### Electronic structure of the NV center

Diamond is an insulator with a large electronic band gap ($\sim 5.5$ eV). The NV center defect has discrete energy levels within this band gab, see figure 2.1b. The orbital ground state $^3A_2$ and the orbital excited state $^3E$ are split by 1.95 eV which corresponds to a zero phonon line (ZPL) of 637 nm. The superscript $^3$ and $^1$ refer to triplet and singlet spin states, while the $A_1, A_2$ and $E$ refer to an orbital symmetry [48]. Each orbital state is further split into a fine structure. The ground state has a zero field splitting of 2.87 GHz due to spin-spin interaction and the excited splitting is 1.42 GHz [48–51]. The nuclear spin of the nitrogen atom splits the fine structure into a hyperfine structure. This nuclear spin can be used as a quantum memory with a one second long coherence time [11]. The singlet states are separated by 1042 nm transitions [52].

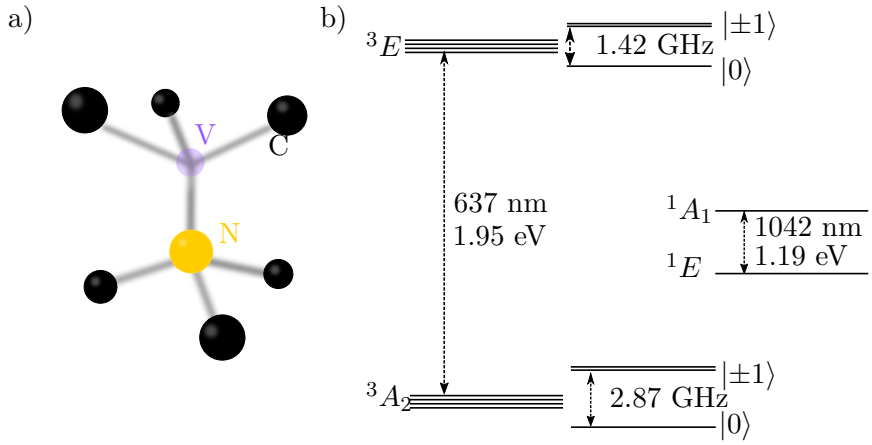


Figure 2.1: a) Atomic structure of the NV center in a diamond lattice. Yellow is a nitrogen atom, purple is a vacancy and black is carbon atoms. b) Electronic structure of the NV-center at room temperature. The ground state $^3A_2$ and excited state $^3E$ are spin triplets. The NV center has 637 nm ZPL optical transition between the excited state and the ground state. The excited state and the ground state are spin triplets, which are further split into a fine structure. $^1A_1$ and $^1E$ are spin singlet states.

### Electronic spin of the NV center

The electronic spin of NV centers can be optically initialized and resonance microwave magnetic fields can be used to coherently manipulate the electron spin state of the NV center [53]. Importantly, due to weak spin-orbit coupling the spin coherence time in the ground state is very long, even at room temperature, and limited by spin-spin interactions [54]. Furthermore, the spin state can be optically read-out due to the spin dependent fluorescence.

### Optical properties of the NV center

The emission spectrum from the NV center is very broad $\sim$ 100 nm. Only 3 % of the emission goes into the ZPL at 637 nm, i.e the Debye-Waller factor is $\alpha \sim 3\%$ [55]. This means that most of the emission occurs in the phonon side band (PSB). For quantum information purposes, only light emitted into the ZPL is useful, since

the phonon creation leads to decoherence.

The NV center has an excited state lifetime of 12 ns, which is relatively long compared to the silicon vacancy (SiV) centers and the GeV centers, which limits the photon flux from the NV center [56]. The quantum efficiency is high for the NV center. Recently, the quantum efficiency was measured for shallow implanted NV centers and was estimated to be $> 86\%$ for NV centers in a bulk diamond [57].

The dipole orientation lies in the plane perpendicular to the NV axis [58, 59], which is different compared to the SiV center [60].

### 2.1.2 The GeV center

The GeV center was first reported in 2015 [61–63]. The GeV center has a very narrow optical transition, like the SiV center, which makes it very interesting for quantum information technology.
The GeV center has been synthesized in diamond by three different techniques; ion-implantation, chemical vapor deposition (CVD) and by a high temperature high pressure (HTHP) growth technique. It has been confirmed that the GeV center is negatively charged similar to the NV center [17].

#### Atomic structure of the GeV center

The calculated atomic structure of a GeV center has a $3D_3$ symmetry and is shown in figure 2.2. The Ge atom sits in an interstitial site between two adjacent vacancies in the <111> direction [61–63]. Noticeably, the GeV center has inversion symmetry. The GeV center, therefore, has a vanishing permanent electrical dipole moment, which makes the optical transition insensitive to electric field fluctuations in the environment (the AC Stark effect). The optical coherences of the dipole transitions are protected from these external electrical fields, which gives the GeV centers low spectral diffusion and narrow linewidths [64].

#### Electronic structure of the GeV center

The ground state $^2E_g$ and excited state $^2E_u$ of the GeV center are separated by 2.06 eV and both states are two-fold degenerate in both the orbital and the spin degrees of freedom, which is partially lifted due to the spin-orbit interaction [63]. The superscript index 2 in the state names refers to the spin degeneracy and $E_{u,g}$ refer to the symmetry of the state. The spin degeneracy can be split by applying a magnetic field [17].

#### Optical properties of the GeV center

The ZPL of the GeV center is $\sim 602.5$ nm and the excited state lifetime is $\sim 6$ ns. By using Huang-Rhys model the PSB is estimated to around 40 % of the total emission [65], i.e the GeV center has a Debye-Waller factor $\alpha$=0.60, which is in contrast to the NV center's $\alpha = 0.03$.

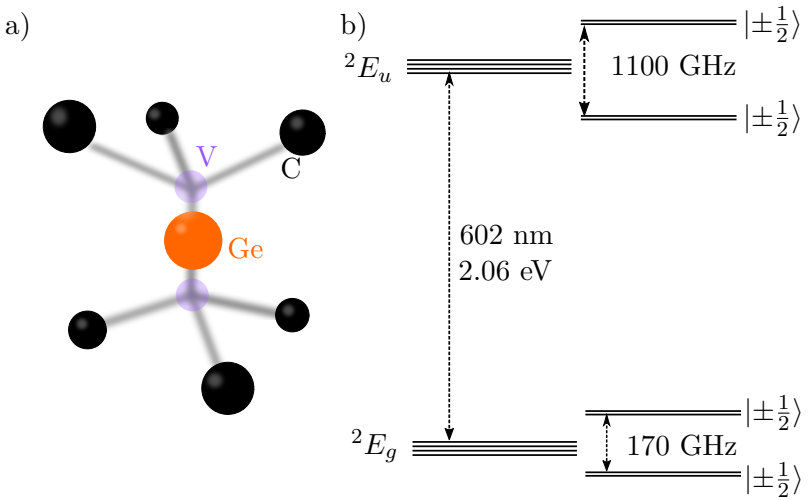


Figure 2.2: a) Atomic structure of the GeV center in a diamond lattice. Purple is a lattice vacancy, black is carbon atoms and orange is a germanium atom. b) Electronic structure of the GeV center. The excited state $^2E_u$ and the ground state $^2E_g$ are split by 2.06 eV, which corresponds to a ZPL of 602 nm. Both the excited state and the ground state are two-fold degenerate in spin and orbit degree of freedom. The degeneracy is lifted by the spin-orbit interaction.

The linewidth of the ZPL is $\sim$ 5 nm at room temperature. At cryogenic temperatures the ZPL reveals four spectral lines corresponding to the four transitions in the fine structure [63]. At cryogenic temperature the linewidth is close to lifetime limited. Also, at cryogenic temperature, mode splitting (Autler–Townes effect) has been observed at a high optical intensity indicating a stable and narrow optical transition [17].

#### Electron spin of the GeV center

Polarization and control of the electronic spin system in a single GeV center have been demonstrated at 2 K [17]. A spin coherence time of $\sim$20 ns and a relaxation time of 25 µs were also reported [17].

## 2.2 Optical Fabry-Pérot cavities

Optical cavities can be used to enhance the emission properties of color centers in diamond. Importantly, for strong interaction between the cavity mode and the color center in diamond is a small mode volume $V$ and high finesse $F$. These parameters will be described in the following section.

In an optical cavity, light can constructively interfere and build up in a confined space. This is critical for achieving high coupling to a color center. In this section, we discuss optical Fabry-Pérot cavities and introduce important parameters describing such a cavity.

Specifically, we want to understand and derive expressions for the losses of the cavity and the mode volume. We will start with the simple model of an empty cavity. Then,

we will investigate the use of dielectric mirrors and, finally, we will look into how the cavity mode changes with a diamond membrane inside the cavity.

In our model we use a monocromatic electric field, which is given by [66]:

$$\mathcal{E}(\mathbf{r},t) = \Re[\mathbf{E}(\mathbf{r})\exp(i\omega t)], \tag{2.1}$$

where $\Re$ is the real part and $\mathbf{E}(\mathbf{r})$ is the complex amplitude, which for plane waves is given by:

$$\mathbf{E}(\mathbf{r}) = \mathbf{E}_0\exp(-i\mathbf{k}\cdot\mathbf{r}), \tag{2.2}$$

where $\mathbf{k}$ is the wave vector. The simplest model of the cavity is a 1 dimensional model and therefore, we can use scalar fields. First, we consider a Fabry-Pérot cavity with two plane mirrors separated by a distance, $L$, with transmission coefficients $t_1, t_2$ and reflection coefficients $r_1, r_2$. If an incoming field $E_{\text{inc}}$ is incident at the first mirror, then the intra-cavity field $E_{\text{cav}}$ is given by [66]:

$$E_{\text{cav}} = t_1\sum_{j=1}^{\infty}\left(r_1r_2\exp(-i\phi)\right)^j E_{\text{inc}} = \frac{t_1E_{\text{inc}}}{1-(r_1r_2\exp(-i\phi))}, \tag{2.3}$$

where $\phi$ is the phase accumulation for one round trip in the cavity, which for a bare cavity is given by $\phi = 2Lk = 4\pi L/\lambda$. Here, we assume that the mirrors add a phase shift of $\pi$ each, i.e. $r_1r_2 = |r_1r_2| = \sqrt{\mathcal{R}_1\mathcal{R}_2}$, where $\mathcal{R}_{1,2}$ is the power transmission of the mirrors. The field intensity inside the cavity is then:

$$I = |E_{\text{cav}}|^2 = \frac{I_{\text{inc}}t_1^2}{(1-r_1r_2)^2+4r_1r_2\sin^2(\phi/2)} = I_{\max}\frac{1}{1+(2F/\pi)^2\sin^2(\phi/2)}, \tag{2.4}$$

where the intensity of the incoming light is $I_{\text{inc}} = |E_{\text{inc}}|^2$, the maximum intensity is $I_{\max} = \frac{I_{\text{inc}}t_1^2}{(1-r_1r_2)^2}$ and the finesse $F = \frac{\pi\sqrt{r_1r_2}}{(1-r_1r_2)}$. We see that $I = I_{\max}$ when $\sin^2(\phi/2) = 0 \Leftrightarrow \phi = 2\pi m$, where $m$ is an integer. $m$ is called the longitudinal mode number. This gives the resonant condition in length:

$$L_m = m\cdot\frac{\lambda}{2} = m\cdot L_{\text{fsr}} \tag{2.5}$$

or in frequency:

$$\nu_m = m\cdot\frac{c}{2L} = m\cdot\nu_{\text{fsr}}, \tag{2.6}$$

where the free spectral range, which defines the spacing between resonances in length and frequency, is defined by $L_{\text{fsr}} = \frac{\lambda}{2}$ and $\nu_{\text{fsr}} = \frac{c}{2L}$. The finesse is the average number of round trips in the cavity. The finesse is given by the ratio between the free spectral range and the full width half maximum (FWHM) linewidth $\Delta\nu$ of the resonances:

$$F = \frac{\nu_{\text{fsr}}}{\Delta\nu} \tag{2.7}$$

For high finesse cavities $|r_1r_2| \approx 1 \Rightarrow 1 - r_1r_2 \ll 1$ the finesse can be approximated by:

$$F \approx \tfrac{\pi}{(1-r_1r_2)} \tag{2.8}$$

Using power conservation $r_1 r_2 = \sqrt{\mathcal{R}_1 \mathcal{R}_2} = \sqrt{(1 - T_1 - \mathcal{L}_1)(1 - T_2 - \mathcal{L}_2)}$, where $T_i, \mathcal{L}_i$ are the mirror power transmissions and mirror losses, respectively. We find that:

$$F \approx \frac{2\pi}{T_1 + \mathcal{L}_1 + T_2 + \mathcal{L}_2} = \frac{2\pi}{\mathcal{L}_{\text{tot}}}, \tag{2.9}$$

where $\mathcal{L}_{\text{tot}}$ is the total losses of the cavity. This is the typical measure we will use to characterize the quality of length tunable cavities, since this measurement is independent of the cavity length. Closely related to the finesse is the quality factor $Q$:

$$Q = \frac{\nu_0}{\Delta\nu} = \frac{2L}{\lambda} F, \tag{2.10}$$

where $\nu_0$ is the frequency of the light in the cavity. Another way to understand $Q$ is as the ratio of the energy stored in the cavity to the cavity decay rate $\kappa$.

$$Q = \frac{\omega}{\kappa} = \omega\tau = 2\pi\nu_0\tau, \tag{2.11}$$

where $\omega$ is the light's angular frequency and $\tau = \frac{1}{2\pi\Delta\nu} = \frac{1}{\kappa}$ is the photon lifetime in the cavity.

Another important parameter of the cavity is the mode volume $V$. To determine $V$ we need to consider the transverse spatial mode distribution, which is the subject of the next section.

### 2.2.1 Gaussian modes

By studying the Gaussian cavity modes, we find a correction to the cavity resonance condition compared to the plane wave model above. The mode volume $V$ can be calculated for Gaussian modes. Further, we get an expression for the radius of curvature (ROC) of the concave spherical mirror as a function of the transverse mode splitting.

In our experiment, we use a cavity with one planar mirror and one concave spherical mirror to achieve a stable cavity. A Gaussian beam retraces itself if its wavefronts match the radius of curvature (ROC) of a spherical mirror. Therefore, Gaussian beams are stable modes in spherical cavities.

A Gaussian beam propagating in the $z$ direction is given by [66]:

$$E(\mathbf{r}) = \frac{E_1}{q(z)} \exp\left(-ik\frac{x^2 + y^2}{2q(z)}\right), \tag{2.12}$$

where $q(z) = z + iz_0$ is the complex $q$-parameter of the Gaussian beam and $z_0$ is the Rayleigh length. $q$ fully describes the Gaussian beam's properties: the width $W$ and the wavefronts radius of curvature $R$. The relation is:

$$\frac{1}{q(z)} = \frac{1}{R(z)} - i\frac{\lambda}{\pi W^2(z)} \tag{2.13}$$

Hermite-Gaussian beams are the full set of solutions to the paraxial Helmholtz equation and they all share the same wavefronts as the Gaussian beam and therefore, they

are also modes for the spherical mirror cavity. Since the phase of Hermite-Gaussian beams of the order ($k$, $n$) are different from the phase of the plane waves we get new cavity resonance conditions [67]:

$$\nu_{knm} = m\nu_{\text{fsr}} + (k+n+1)\nu_{\text{trans}}, \quad \nu_{\text{trans}} = \frac{\arccos(\sqrt{g_1 g_2})}{\pi}\nu_{\text{fsr}}, \tag{2.14}$$

where $g_i$ is a geometrical parameter of the cavity given by:

$$g_i = 1 - \frac{L}{R_i}, \qquad i = 1, 2, \tag{2.15}$$

where $R_i$ is the radius of curvature of mirror $i$. In our cavity we use one planar mirror and one concave mirror. For a planar mirror $g_1 = 1$ and for a concave mirror $g_2 = 1 + \frac{L}{ROC}$ with $R_2 = -\text{ROC}$ , such that the transverse mode splitting is given by:

$$\nu_{\text{trans}} = \frac{\arccos(\sqrt{1+\frac{L}{\text{ROC}}})}{\pi}\nu_{\text{fsr}} \Rightarrow \text{ROC} = L\left(1 - \cos^2\left(\frac{\nu_{\text{trans}}}{\nu_{\text{fsr}}}\pi\right)\right)^{-1} \tag{2.16}$$

This equation can be used to determine the effective ROC of our fiber mirror by measuring the $\nu_{\text{trans}}$ and the cavity length.
For a short cavity, where $L \ll \text{ROC}$, we can assume that $W(z) \approx W_0$ for the entire length of the cavity, where $W_0$ is the beam waist. For a half symmetric cavity the beam waist is given by [29]:

$$W_0 = \sqrt{\frac{\lambda}{\pi}}\left(\text{ROC}\, L\right)^{1/4} \tag{2.17}$$

The mode volume is given by integrating 2D Guassian beam times the half length of the cavity:

$$V = \pi\frac{W_0^2}{4}L = \frac{\lambda}{4}\sqrt{\text{ROC}}L^{3/2} \tag{2.18}$$

Notice that this expression is only valid for $L \ll \text{ROC}$.

All the expressions found above is for a bare cavity with perfect mirrors. When the cavities get short the electric field penetration into the dielectric mirrors becomes important. This is the subject of the next section.

### 2.2.2 Distributed Bragg reflectors

We use distributed Bragg reflectors (DBR) as mirrors for our cavity. DBR mirrors can achieve higher reflectivity than metallic mirrors at the cost of higher mode volume since the electric field penetrates into the DBR mirrors. DBR mirrors consist of alternating layers of two dielectric materials, one with high refractive index and one with low. The layer thickness is often chosen to be a quarter wavelength of the design wavelength, such that the multiple reflections from the dielectric interface interfere constructively. We use the transfer matrix method to calculate the power reflection $\mathcal{R}$, transmission $T$ and losses $\mathcal{L}$ of the dielectric layers that constitute the mirrors.

Each layer is described by its refractive index $n_i$ and thickness $t_i$. The electric field inside each layer is the sum of a forward propagating field $E_i^+$ and a backward propagating field $E_i^-$, see figure 2.3.

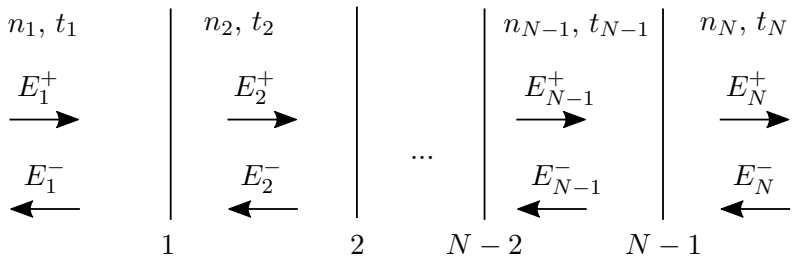


Figure 2.3: $N$ layers of dielectric materials. Layer $i$ with refractive index $n_i$ and thickness $t_i$. The electric field inside each layer is decomposed into a forward $E^+$ and a backward $E^-$ propagating component. The interfaces are labelled 1 to $N-1$.

The propagation of the fields inside the layers is given by the matrix:

$$P_i = \begin{bmatrix} \exp(i\phi_i) & 0 \\ 0 & \exp(i-\phi_i) \end{bmatrix}, \tag{2.19}$$

where the phase change is $\phi = k_0 n t_i$. The absorption losses are included in the imaginary part of the refractive in this phase contribution. The relation between electric amplitudes at interface is given by $M_i$:

$$\begin{bmatrix} E_i^+ \\ E_i^- \end{bmatrix} = M_i \begin{bmatrix} E_{i+1}^+ \\ E_{i+1}^- \end{bmatrix} \tag{2.20}$$

$$= \frac{1}{t_{i,i+1}} \begin{bmatrix} 1 & r_{i,i+1} \\ -r_{i+1,i} & t_{i,i+1}t_{i+1,i} - r_{i+1,i}r_{i,i+1} \end{bmatrix} \begin{bmatrix} E_{i+1}^+ \\ E_{i+1}^- \end{bmatrix}, \tag{2.21}$$

where $t_{i,i+1}$ and $r_{i,i+1}$ is the standard Fresnel transmissions and reflection coefficients, respectively. Scattering losses are introduced at the dielectric interface by modifying the Fresnell coefficients [68, 69]:

$$\tilde{r}_{i,i+1} = r_{i,i+1} \exp(-2(k_0 n_i \sigma_i)^2) \tag{2.22}$$

$$\tilde{r}_{i+1,i} = r_{i+1,i} \exp(-2(k_0 n_{i+1} \sigma_i)^2) \tag{2.23}$$

$$\tilde{t}_{i,i+1} = t_{i,i+1} \exp\left(-\frac{1}{2}(k_0(n_{i+1}-n_i)\sigma_i)^2\right) \tag{2.24}$$

$$\tilde{t}_{i+1,i} = t_{i+1,i} \exp\left(-\frac{1}{2}\left(k_0(n_i-n_{i+1})\sigma_i\right)^2\right), \tag{2.25}$$

where $\sigma_i$ is the surface roughness in root mean square (RMS) at interface $i$. The modified Fresnel coefficients are replaced by the standard coefficient in equation 2.21. The total dielectric stack is a concatenation of each of the basic element matrices:

$$M_{total} = M_1 P_2 M_2 P_3 ... M_{N-1} P_N = \prod_{i=1}^{N-1} M_i P_{i+1} \tag{2.26}$$

The relation between the incoming field and the outer layer is:

$$\begin{bmatrix} E_0^+ \\ E_0^- \end{bmatrix} = M_{total} \begin{bmatrix} E_N^+ \\ E_N^- \end{bmatrix} = \begin{bmatrix} M_{11} & M_{12} \\ M_{21} & M_{22} \end{bmatrix} \begin{bmatrix} E_N^+ \\ E_N^- \end{bmatrix} \tag{2.27}$$

From this, we can calculate $\mathcal{R}, T$ and $\mathcal{L}$ by:

$$\mathcal{R} = \left|\frac{M_{21}}{M_{11}}\right|^2 \tag{2.28}$$

$$T = \frac{n_N}{n_1}\left|\frac{1}{M_{11}}\right|^2 \tag{2.29}$$

$$\mathcal{L} = 1 - R - T \tag{2.30}$$

We used DBR mirrors with alternating layers of $SiO_2$, with a low refractive index $n_l$, and $Ta_2O_5$, with a high refractive index $n_h$. The thickness $t_i$ of each layer is a quarter wavelength of a target wavelength $\lambda_t$, i.e. $t_i = \frac{\lambda_t}{4n_i}$ for $i = l, h$. An example of a transmission curve for a mirror design with a design wavelength of $\lambda_t = 615$ nm is shown in figure 2.4. Here, we neglect absorption and scattering losses. From figure 2.4 it is seen that very low transmissions, and therefore very high reflectivities, can be achieved with the DBR mirrors.

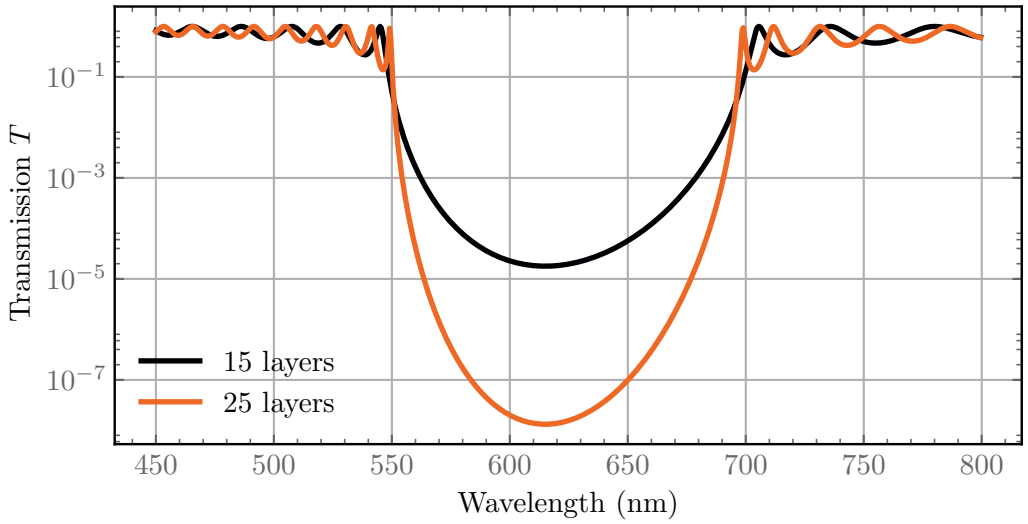


Figure 2.4: Transmission curves for DBR mirrors with 15 and 25 layers of $SiO_2$ and $Ta_2O_5$ for normal incident light. Each layer has a thickness $t_i = \frac{615\text{nm}}{4n_i}$. The bandwidth of the mirror is mostly determined by the contrast in refractive index of the dielectric coating materials [66].

The field distribution inside the DBR mirror is shown in figure 2.5. From 2.5, it can be seen that the field is exponentially decaying inside the mirror. This field penetration is important for short cavities where a substantial fraction of the mode volume is in the mirrors. For this high index terminated mirror there is a node at the air mirror interface, whereas for a low index terminated mirror there will be an antinode at the interface.

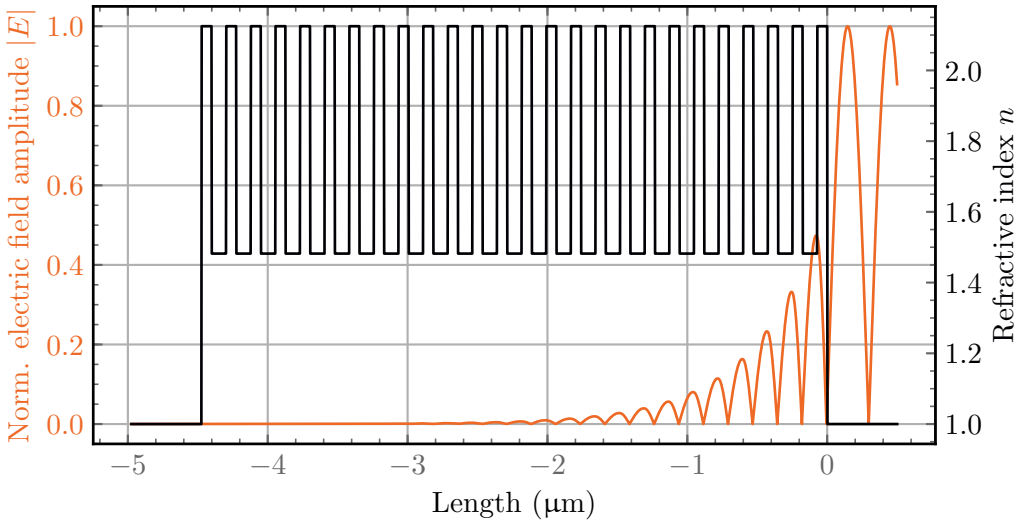


Figure 2.5: Electric field distribution inside the DBR mirror with 26 layers of $Ta_2O_5$ and 25 layers of $SiO_2$. The electric field, with $\lambda = 615$ nm, is incident from the the right and has a node at air interface when the mirror is high index terminated.

### 2.2.3 Cavity modes with a diamond membrane

When a diamond membrane is introduced inside the cavity it adds an extra, partly reflective, diamond air interface inside the cavity. It is instructive to first look at a 1D model with perfect high index terminated mirrors to see how the resonance condition changes. For a cavity with a diamond membrane thickness of $t_d$ and an air gap thickness of $L - t_d$ the resonance condition is given by [43]:

$$(1 + n_d) \sin\left(\frac{2\pi\nu_m}{c}\left[L + t_d(n_d - 1)\right]\right) = (1 - n_d) \sin\left(\frac{2\pi c}{\lambda}\left[L - t_d(n_d + 1)\right]\right), \quad (2.31)$$

where $n_d$ is the refractive index of diamond. The solution for the hybrid cavity resonances are shown in figure 2.6. Resonances with a field distribution only in diamond and only in air, respectively, are also shown in the figure. The diamond modes are independent of $L$ since the diamond membrane thickness is fixed. The air modes are linear as for the bare cavity. Depending on the energy distribution inside the cavity the hybrid modes are said to be either diamond-like or air-like. For air-like resonances, a large fraction of the electric field intensity is in the air gap of the cavity and the resonant wavelength is more sensitive to length changes of the air gap. For diamond-like modes, the field intensity is higher in the diamond membrane than in the air gap and therefore, the resonant wavelength is not as sensitive to length changes compared to the air-like mode.

A higher field intensity in the diamond membrane is typically preferable for higher coupling strength to the color centers in diamond. Only if scattering losses from the diamond membrane surface become too high, can an air-like mode become preferable [70].

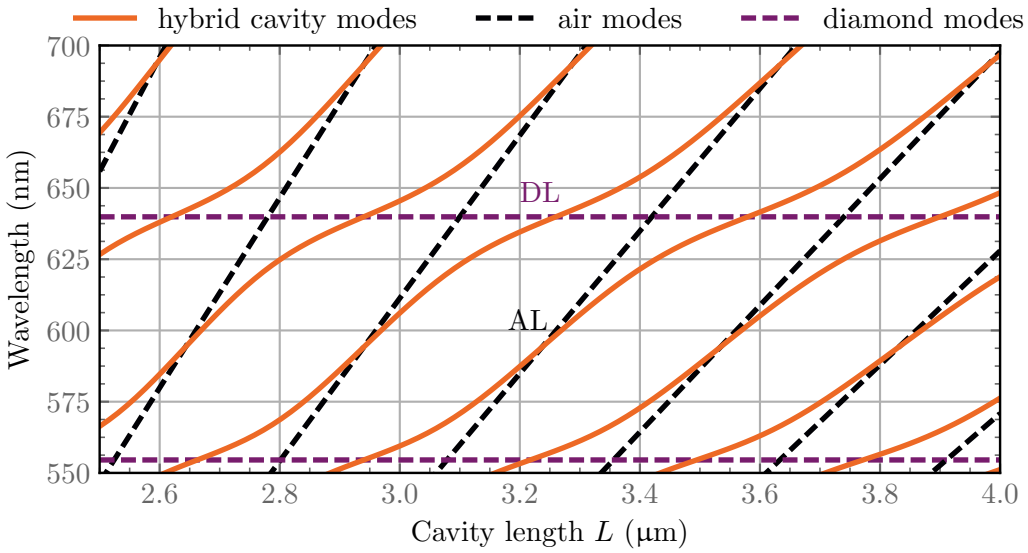


Figure 2.6: Resonance models for a hybrid diamond-air cavity (orange) with a diamond thickness $t_d = 860$ nm. Resonance models for a bare cavity (black) and for the diamond membrane (purple) with a fixed length are shown. When the hybrid mode intersects with the air the hybrid mode is said to be air-like (AL) and when the hybrid mode intersects with the diamond mode the hybrid mode is said to be diamond-like (DL).

For short cavities, however, the field penetration into the DBR mirrors becomes critical in order to calculate the correct mode volume and the coupling strength of the cavity mode to the GeV centers.
Therefore, we will now describe the two DBR mirrors, $M_d$ and $M_a$, which we used in our experiments. The $M_d$ mirror is low index terminated and is holding a diamond membrane of thickness $t_d$ and the $M_a$ mirror is high index terminated, see figure 2.7.

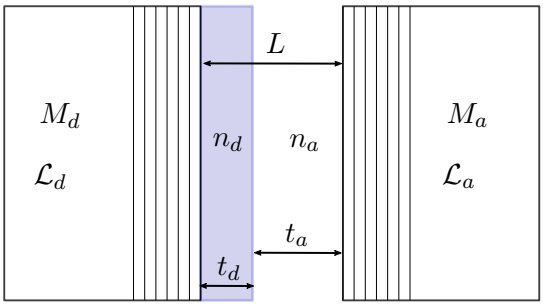


Figure 2.7: 1 dimensional cavity model for our micro-cavity. The low index terminated mirror holding the diamond $M_d$ has the total losses $\mathcal{L}_d$. The other high index terminated mirror $M_a$ has the total losses $\mathcal{L}_a$. The total length of the cavity $L$ is the sum of the diamond thickness $t_d$ and the air gap $t_a$. $n_d$ is the diamond membrane refractive index and the refractive index of air is $n_a = 1$.

For a hybrid cavity, the picture of a photon bouncing back and forth between the two mirrors is no longer valid, since the photon is sometimes reflected at the diamond air interface. This means that the definitions of the cavity finesse and the free spectral range, which are defined from the inverse of the round-trip losses and the inverse

of the round-trip time, respectively, are not well defined for a hybrid diamond air cavity. However, the decay rate $\kappa$ is still well defined as the loss rate per unit time. To calculate the linewidth $\Delta\nu = \frac{\kappa}{2\pi}$ it is useful to introduce an effective cavity length $L_{\text{eff}}$ and an effective cavity loss $\mathcal{L}_{\text{eff}}$ per round trip. We use the formalism for these effective quantities given by Dam, Ruf, and Hanson [70].

The effective length $L_{\text{eff}}$ of the hybrid cavity, taken in reference to the speed of light in diamond $c/n_d$, is therefore a measure of the cavity length if it only consisted of diamond. The effective length is given by:

$$L_{\text{eff}} = \frac{\int_{\text{cav}} n(z)^2 \left|E(z)\right|^2 \mathrm{d}z}{n_d^2 \left|E_{\text{max,d}}(z)\right|^2 /2}, \tag{2.32}$$

where $E_{\text{max,d}}(z)$ is the maximum electric field inside the diamond membrane. The factor of 2 in the denominate is introduced such that $L_{\text{eff}}$ is the effective geometrical length, whereas the effective round-trip length is $2L_{\text{eff}}$, as for the bare cavity. Notice that this definition of the effective cavity length includes the field penetration into the DBR mirrors. The effective length can be calculated using the transfer matrix method, see section 2.2.2.

The linewidth in frequency can be calculated using the effective length:

$$\Delta\nu = \frac{c/(2L_{\text{eff}})}{2\pi/\mathcal{L}_{\text{eff}}}, \tag{2.33}$$

where the effective losses are the losses in an effective round trip:

$$\mathcal{L}_{\text{eff}} = \frac{I_{\text{max,a}}}{I_{\text{max,d}}}\mathcal{L}_a + \mathcal{L}_d = \frac{\mathcal{L}_a}{\zeta} + \mathcal{L}_d, \tag{2.34}$$

where $\mathcal{L}_a$ and $\mathcal{L}_d$ are the total losses from each mirror, including transmission $T$. The ratio $\zeta = \frac{I_{\text{max,d}}}{I_{\text{max,a}}}$ is the ratio of the maximum intensity in the diamond membrane $I_{\text{max,d}}$ to the maximum intensity in the air gap $I_{\text{max,a}}$. The ratio is determined by the diamond membrane thickness only. $\zeta$ can be calculated using the transfer matrix method. We calculate the electric field distribution for the DBR mirror $M_d$ with a diamond membrane and an air gap on top. We calculate $\zeta$ by:

$$\zeta = \frac{n_d \left|E_{\text{max,d}}(z)\right|^2}{\left|E_{\text{max,a}}(z)\right|^2}, \tag{2.35}$$

where $E_{\text{max,d}}$ and $E_{\text{max,a}}$ are the maximum electric field amplitude in the diamond membrane and air gap, respectively. The calculated results of $\zeta$ are shown in figure 2.8. From the figure it is seen that $\zeta$ oscillates between maximum $n_d$, for a diamond like mode, and minimum $1/n_d$, for an air-like mode. We found a position on the membrane with thickness $t_d = 860$ nm, such that the hybrid cavity mode was almost fully diamond-like.

From this, we can now determine the linewidth $\Delta\nu$ in equation 2.33 and therefore also the cavity decay rate $\kappa = 2\pi\Delta\nu$. Furthermore, we can calculate the escape efficiency through our out-coupling mirror, which, in our case, is $M_d$:

$$\varepsilon_{flat} = \frac{T_d}{L_{\text{eff}}}, \tag{2.36}$$

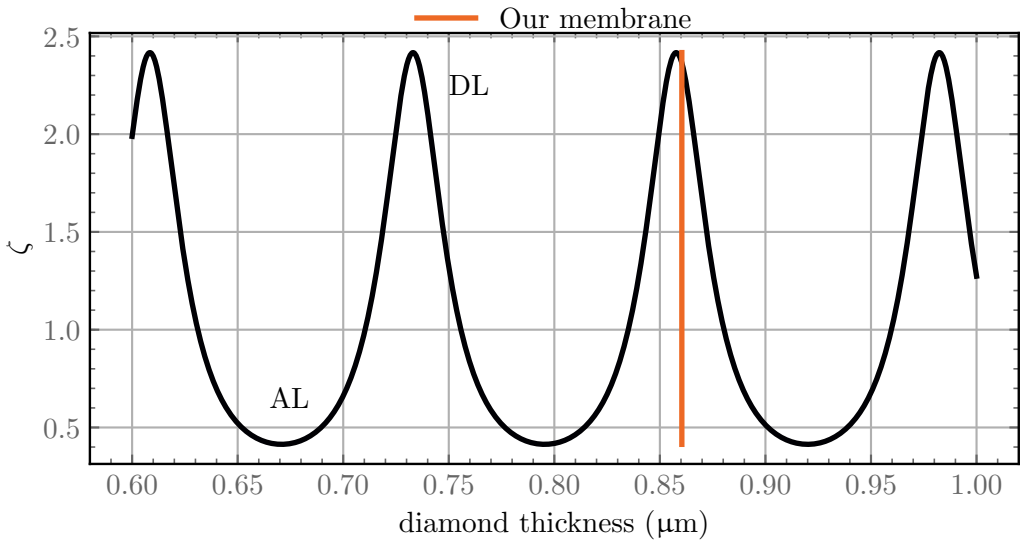


Figure 2.8: $\zeta$ is the ratio between maximum intensity in the diamond membrane $I_{\mathrm{max,d}}$ and the maximum intensity in the air gap $I_{\mathrm{max,a}}$. $\zeta$ oscillates between $n_d$ and $1/n_d$ depending on whether the cavity mode is diamond-like (DL) or air-like (AL). The diamond membrane that we use in these experiments is 860 nm, which means that the cavity mode is diamond-like.

where $T_d$ is the transmission of the diamond terminated flat mirror. This is useful for calculating the overall collection efficiency in our experiment.

Next, we can use the effective length to calculate the mode volume. The mode volume is given by [71, 72]:

$$V = \frac{\int_{\mathrm{cav}} |E(\mathbf{r})|^2 \, n(\mathbf{r})^2 \mathrm{d}^3\mathbf{r}}{|E_{\mathrm{max,d}}|^2 \, n_d^2} \tag{2.37}$$

This expression can be simplified to:

$$= \frac{\pi W_0^2}{2} \frac{\int n(z)^2 \, |E(z)|^2 \, \mathrm{d}z}{|E_{\mathrm{max,d}}|^2 \, n_d^2} \tag{2.38}$$

$$= \frac{\pi W_0^2}{4} L_{\mathrm{eff}}, \tag{2.39}$$

where we have used the two dimensional Gaussian integral for a mode with a constant mode radius $W_0$, i.e. we have assumed that the cavity length is much shorter than the ROC. We recognize the similarity with equation 2.18, where the effective length has taken the place of the geometrical length.

To calculate the beam waist $W_0$ we use the ABCD law for Gaussian beams [66]. The law states that an incident Gaussian beam $q_1$ is transformed through a paraxial optical system described by A,B,C,D to a transmitted Gaussian beam by the relation:

$$q_2 = \frac{Aq_1 + B}{Cq_1 + D} \tag{2.40}$$

For the cavity to be stable, the $q$-parameter should be the same after the beam has propagated through each element of the cavity. Therefore, we can look for solutions where $q1 = q2 = q$:

$$q = \frac{Aq + B}{Cq + D} \Rightarrow \tag{2.41}$$

$$q = \frac{A - D \pm \sqrt{(D - A)^2 + 4BC}}{2C} \tag{2.42}$$

For the solutions to be valid they must hold that $\Im(q) > 0$, where $\Im$ is the imaginary part. By setting up the system's ABCD matrix for the cavity with the diamond membrane, the waist can be determined by:

$$W_0 = \sqrt{\Im(q)\frac{\lambda}{n\pi}}, \tag{2.43}$$

where $n$ is the refractive index. This concludes the cavity characterization and the next section describes how the GeV center interacts with the cavity mode.

## 2.3 Cavity quantum electrodynamics

In this section, we will start by introducing the coupling between a two level system and a single cavity mode in a closed system. Then, we will introduce dissipation in the system, which naturally introduces a strong and weak coupling regime. Further, we introduce the important quantities $\beta$ and $F_p$ for the weak coupling regime. $\beta$ is the probability for GeV emission into the cavity mode upon excitation and the Purcell factor $F_p$ describes the enhancement of the spontaneous emission.
This discussion draws inspiration from the PhD thesis by Roland C. Albrecht [73] and the PhD thesis by Daniel Riedel [74].

We model the quantum emitter (QE) as a two level system. The two levels are a ground state $|g\rangle$ and an excited state $|e\rangle$, which are split by the energy $\hbar\omega_e$. A photon in the cavity mode has the energy $\hbar\omega_c$. The Hamiltonian describing the system is the Jaynes–Cummings Hamiltonian, which, for our system, is given by:

$$\hat{H}_{JC} = \hbar\omega_e\hat{c}^\dagger\hat{c} + \hbar\omega_c\hat{a}^\dagger\hat{a} + \hbar g\left(\hat{c}^\dagger\hat{a} + \hat{c}\hat{a}^\dagger\right), \tag{2.44}$$

where $\hat{c}^\dagger, \hat{c}$ are the fermionic creation and annihilation operators for the two level system and $\hat{a}^\dagger, \hat{a}$ are the bosonic creation and annihilation operators for the cavity mode. $g$ is the coherent coupling rate between the quantum emitter and the cavity mode. Here, we have used the rotating wave approximation. The coupling rate is given by:

$$g = \sqrt{\frac{\mu^2\omega}{2\hbar\varepsilon_0 V}} = \sqrt{\frac{3c\lambda^2\gamma}{8\pi n^3 V}}, \tag{2.45}$$

where $\mu$ is the dipole moment of the emitter transition and $V$ is the mode volume of the cavity mode. The last expression is found using equation 2.62. This system exhibits Rabi oscillations, which are coherent transfer of the energy between the cavity mode and the QE. The eigenstates of the Jaynes–Cummings Hamiltonian are the dressed states.

In a real system there is dissipation of energy and dephasing. Therefore, we introduce the density operator $\rho$ and use the master equation formalism to calculate the time evolution of the system. The quantum emitter dissipates energy at a rate $\gamma$ by non-radiative decay channels or by emission of a photon into optical modes other than the cavity mode. Furthermore, dephasing of the quantum emitter occurs due to inelastic phonon scattering with a rate $\gamma^\star$. The cavity decay rate $\kappa$ includes transmission, scattering and absorption losses. Figure 2.9 show the modelled system and the dissipation processes.

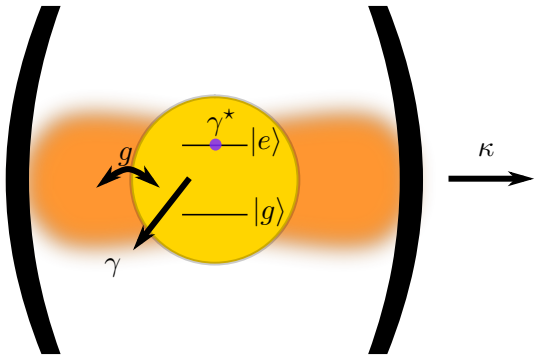


Figure 2.9: Model of a two level system coupled to a cavity mode with dissipative channels. The two level system has a decay rate of $\gamma$ and due to phonon scattering it exhibits pure dephasing at a rate of $\gamma^\star$. The two level system couples to the cavity mode at a rate $g$ and photons in the cavity mode leaks out of the cavity at a rate $\kappa$.

The time evolution of the system can be described by the Lindblad master equation. We consider the time evolution for an initial excitation of the QE while the cavity is in the vacuum state. Using the notion from Grange et al. [75] we can write the master equation as:

$$\frac{\mathrm{d}\hat{\rho}}{\mathrm{d}t} = \frac{i}{\hbar}\left[\hat{\rho}, \hat{H}_{JC,R}\right] + \hat{\mathcal{L}}_{\mathrm{QE}} + \hat{\mathcal{L}}_{\mathrm{cav}} + \hat{\mathcal{L}}_{\mathrm{dephasing}}, \tag{2.46}$$

where $\hat{\rho}$ is the reduced density operator of the cavity quantum emitter system:

$$\hat{\rho}(t) = \begin{bmatrix} \rho_{ee}(t) = \langle \hat{c}^\dagger(t)\hat{c}(t)\rangle & \rho_{ec}(t) = \langle \hat{c}^\dagger(t)\hat{a}(t)\rangle \\ \rho_{ce}(t) = \langle \hat{a}^\dagger(t)\hat{c}(t)\rangle & \rho_{cc}(t) = \langle \hat{a}^\dagger(t)\hat{a}(t)\rangle \end{bmatrix} \tag{2.47}$$

The Jaynes–Cummings Hamiltonian in a rotating frame $\hat{H}_{JC,R}$ and the dissipative terms are given by:

$$\hat{H}_{JC,R} = \begin{bmatrix} 0 & g \\ g & \delta \end{bmatrix} \tag{2.48}$$

$$\hat{\mathcal{L}}_{\mathrm{QE}} = -\gamma \begin{bmatrix} \rho_{ee} & \rho_{ec}/2 \\ \rho_{ce}/2 & 0 \end{bmatrix} \tag{2.49}$$

$$\hat{\mathcal{L}}_{\mathrm{cav}} = -\kappa \begin{bmatrix} 0 & \rho_{ec}/2 \\ \rho_{ce}/2 & \rho_{cc} \end{bmatrix} \tag{2.50}$$

$$\hat{\mathcal{L}}_{dephaing} = -\gamma^\star \begin{bmatrix} 0 & \rho_{ec}/2 \\ \rho_{ce}/2 & 0 \end{bmatrix}, \tag{2.51}$$

where the detuning is $\delta = \omega_c - \omega_e$. The dynamic of the emitter cavity system is often divided into two regimes: the strong coupling regime and the weak coupling regime. The emitter cavity rate is faster than the dissipative rates, i.e. $2g \gg \gamma + \kappa + \gamma^\star$ in the strong coupling regime. In this regime the system exhibits damped Rabi oscillations. In the weak coupling regime the dissipation rates are much faster than the emitter cavity coupling, i.e $2g \ll \gamma + \kappa + \gamma^\star$. In the solid state, quantum emitters experience a high dephasing rate due to phonon interaction. This means that QE emitters in the solids states coupled to a cavity always will be in the weak coupling regime at room temperature. This is also the case in our experiment.

### 2.3.1 Weak coupling regime

In the weak coupling regime the coherent terms can be adiabatic eliminated [75] and the population of the excited QE $\rho_{ee}$ and of the excited cavity mode $\rho_{cc}$ are then given by:

$$\frac{\mathrm{d}\rho_{ee}}{\mathrm{d}t} = -(\gamma + R)\rho_{ee} + R\rho_{cc} \tag{2.52}$$

$$\frac{\mathrm{d}\rho_{cc}}{\mathrm{d}t} = -(\kappa + R)\rho_{cc} + R\rho_{ee}, \tag{2.53}$$

where $R$ is the incoherent exchange rate between the cavity and the QE:

$$R = \frac{4g^2}{\kappa + \gamma + \gamma_i^\star} \frac{1}{1 + \left(\frac{2\delta}{\kappa+\gamma+\gamma^\star}\right)^2} \tag{2.54}$$

The efficiency of emission into the cavity mode $\beta$ can be calculated by:

$$\beta = \kappa \int \rho_{cc}(t)\mathrm{d}t = \frac{\kappa R}{\kappa R + \gamma(\kappa + R)} \tag{2.55}$$

The weak coupling regime can further be divided into two regimes: the bad cavity regime and the good cavity regime.

#### The bad cavity regime

In the bad cavity regime the $\kappa > \gamma + \gamma^\star$. In this regime the Purcell enhancement can be observed. This can be seen by eliminating the population of the cavity in equation 2.52, since the relaxation of the cavity population is much faster compared to the other dynamics of the system. This means that the effective decay of the quantum emitter is:

$$\rho_{ee}(t) = \exp(-(\gamma + R)t) \tag{2.56}$$

Here we can see that the decay rate of the emitter is enhanced compared to in free space where the emitter decay is $\gamma$. We can introduce the Purcell factor $F_p$ as:

$$\rho_{ee}(t) = \exp\left(-\gamma\left(1 + \frac{R}{\gamma}\right)t\right) \tag{2.57}$$

$$= \exp\left(-\gamma\left(1 + F_p\right)t\right), \tag{2.58}$$

where $F_p = \frac{4g^2}{\gamma\kappa}$ is the limit where $\kappa > \gamma + \gamma^\star$.
Alternatively, the Purcell factor can be obtained using Fermi's golden rule, where insight into the enhancement of the emission rates can be gained. Fermi's golden rule states that the transition rate between two states is:

$$\gamma = \frac{2\pi}{\hbar}|M_{12}|^2\varrho(\omega_e), \tag{2.59}$$

where $\varrho(\omega)$ is the optical density of states. $M_{12}$ is the transition matrix element $M_{12} = \langle 1|\,\hat{\mathbf{d}}\cdot\hat{\mathbf{E}}_{\text{vac}}\,|2\rangle$, where $\mathbf{E}_{\text{vac}}$ is the vacuum field which drives the spontaneous emission. In free space it can be shown that:

$$\varrho(\omega) = \frac{\omega^2 V}{\pi^2(c/n)^3} \tag{2.60}$$

$$M_{12}^2 = \frac{\mu_{12}^2\hbar\omega_e}{6\epsilon_0 V}, \tag{2.61}$$

where $\mu_{12} = \langle 1|\,\hat{d}\,|2\rangle$ is the dipole moment. Therefore, the free space emission is given by:

$$\gamma = \frac{\mu_{12}^2\omega_e^3}{3\pi\epsilon_0\hbar(c/n)^3} \tag{2.62}$$

This expression can be compared to the emission rate into a cavity mode. The density of states for the cavity is given by:

$$\varrho(\omega) = \frac{2Q}{\pi\omega_e}\frac{\kappa^2}{4(\omega-\omega_c)^2+\kappa^2},$$

where $Q$ is the quality factor of the cavity. The cavity also alters the amplitude of the vacuum field. We introduce $\xi = \frac{|\boldsymbol{\mu}\cdot\mathbf{E}(\mathbf{r}_0)|}{|\boldsymbol{\mu}||\mathbf{E}_{\max}|}$ to account for angular and spatial overlap between the emitter at position $\mathbf{r}_0$ and the cavity mode. $\mathbf{E}_{\max}$ is the maximum field amplitude in the cavity, i.e. the amplitude at an antinode. $\xi = 1$ for an emitter placed in an electric field antinode with a dipole aligned with the cavity electric field. The transition matrix for the cavity is given by:

$$M_{12}^2 = \xi^2\frac{\mu_{12}^2\hbar\omega_e}{2\epsilon_0 V} \tag{2.63}$$

Therefore, the emission rate into the cavity mode is given by:

$$\gamma_{\text{cav}} = \frac{2Q\mu_{12}^2}{\hbar\epsilon_0 V}\xi^2\frac{\kappa^2}{4(\omega_e-\omega_c)^2+\kappa^2} \tag{2.64}$$

Now, we can compare the emission of the emitter in free space with the emission into the cavity mode:

$$\frac{\gamma_{\text{cav}}}{\gamma} = \frac{3Q(\lambda/n)^3}{4\pi V}\xi^2\frac{\kappa^2}{4(\omega_e-\omega_c)^2+\kappa^2} \tag{2.65}$$

When the cavity is on resonance with the dipole transition and $\xi = 1$, we find the well known expression for the Purcell factor:

$$F_p = \frac{\gamma_{\text{cav}}}{\gamma} = \frac{3Q(\lambda/n)^3}{4\pi V} \tag{2.66}$$

This expression is identical with the one found in equation 2.58. The total emission in the cavity is the sum of the emission rate into the cavity $\gamma_{\text{cav}}$ and the emission rate into free space $\gamma$. The efficiency of emission into the cavity mode $\beta$ is given by:

$$\beta = \frac{\gamma_{\text{cav}}}{\gamma + \gamma_{\text{cav}}} = \frac{F_p}{1 + F_p} \tag{2.67}$$

which approaches unity for $F_p \gg 1$. The lifetime of the emitter in the cavity $t_{\text{tot}}$ is reduced by a factor $1 + F_p$:

$$\frac{\tau_{\text{tot}}}{\tau_{\text{free}}} = \frac{\gamma}{\gamma + \gamma_{\text{cav}}} = \frac{1}{1 + F_p}, \tag{2.68}$$

where $t_{\text{tot}}, \gamma_{\text{tot}}$ is the lifetime and decay rate of the emitter coupled to the cavity mode and all free space modes. From this, we can see that increasing the Purcell factor will both increase the total emission rate of the emitter and direct the light into the cavity. This is typically the regime for low temperature solid state emitters, however, at room temperature the dephasing rate is typically so high that the emitter linewidth is much broader than the cavity linewidth. This regime is called the good cavity regime.

**The good cavity regime**

In the good cavity regime the linewidth of the emitter is much broader than the cavity linewidth $\kappa < \gamma + \gamma^\star$. In this regime there is no Purcell enhancement since only a fraction $\frac{\kappa}{\gamma+\gamma^\star}$ of the emission lies within the linewidth of the cavity. However, in this regime photons are funneled into the narrow cavity mode [75, 76]. Funneling means that the cavity effect goes beyond simple filtering of the emission spectrum and that the cavity effect increases the spectral density. Funneling has already been shown for NV centers [31, 32]. The good cavity regime is useful for generating highly indistinguishable photons from a solid state emitter at room temperature.

The emitter cavity exchange rate can be simplified to:

$$R = \frac{4g^2}{\gamma_i^\star} \frac{1}{1 + \left(\frac{2\delta}{\gamma^\star}\right)^2} \tag{2.69}$$

Solid state emitters typically have one or more transitions where the photon emission is accompanied by a photon creation. To account for more than one optical transition we generalize the efficiency of the emission into the cavity mode for $n$ transitions [31]:

$$\beta = \frac{\sum_{j=1}^{n} R_j}{\gamma + \sum_{j=1}^{n} R_j} \tag{2.70}$$

We can measure $\beta$ in our experiment by comparing the emission rate in free space with the emission rate in the cavity. In our free space measurement we have to account for the fraction of light, which is collected by our objective. Therefore, we have to determine the dipole emission of the GeV centers, which is the subject of the next section.

## 2.4 Dipole emitters near dielectric interfaces

To estimate the collection efficiency of our experimental setup we want to determine the directional emission of the GeV center in our (100)-cut diamond membrane. In this section we use a 2 dimensional model of our system to calculate the radiative power for a dipole near the dielectric interfaces.

For quantum emitters, where the emitter size (the electron orbitals) is much smaller than the wavelength of the emitted light, we can use the dipole approximation. It can be shown that the normalised emission from a classical dipole and the normalised spontaneous emission from a quantum emitter are the same in an inhomogeneous environment if the electron orbitals are unchanged by the environment [77]. For a GeV center in a diamond membrane near a dielectric mirror both conditions are fully valid.

The dipole orientation of the GeV center is at the time of writing unknown. By symmetry, we know that the dipole orientation has to be along the [111] axis or in the (111) plane perpendicular to the [111] axis.
There are four transitions contributing to the ZPL at room temperature. Each radiative transition can have different dipole orientations and rates, which is the case for SiV [60].

We use the formalism from [78] to calculate the angular emission pattern for a point dipole near a dielectric interface.
We model a point dipole, which sits at h=125 nm above the diamond-mirror interface. The diamond thickness is $t_d$=1.250 µm at an angle $\theta$ to the z-axis, see figure 2.10. The DBR mirror is made of 50 thin films of alternating $SiO_2$ and $Ta_2O_5$. Each layer has a unique layer thickness, $t_i$. The coating sits on a fused silica substrate.

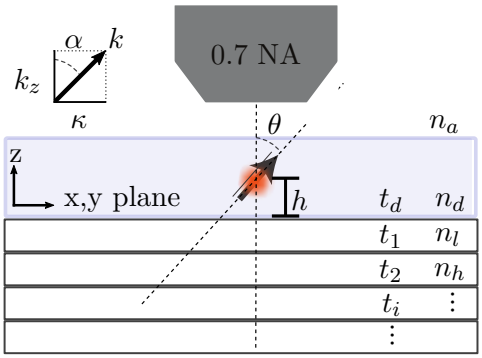


Figure 2.10: Structure of light emitting dipole on a bragg mirror. Each layer has a thickness $t_i$ and a refractive index $n_i$. The dipole sits at a height $h$ and is making an angle $\theta$ with the z axis.

The model can be divided into three layers; top layer (+), emitter layer (e) and bottom layer (-), i.e the air layer, the diamond membrane and the DBR stack, respectively. The reflection coefficients $r_+^{\mathrm{TM,TE}}, r_-^{\mathrm{TM,TE}}$ and transmission coefficients $t_+^{\mathrm{TM,TE}}, t_-^{\mathrm{TM,TE}}$ are calculated, for both the transverse magnetic (TM) and the transverse electric (TE) polarization and for the top and bottom layer, as a function of the in-plane wave vector $\kappa$. Then, we use the analytical expressions to calculate the power density $K$ per unit $\mathrm{d}\kappa^2$. The power density is normalized to the emission power in an finite

medium with refractive index $n_e$:

$$F = \int_0^\infty K(\kappa) \mathrm{d}\kappa^2, \tag{2.71}$$

where $F$ is the normalized total radiated power. $F = 1$ if there is no Purcell enhancement.

The power density depends on both the dipole orientation and on the polarization. For a horizontal dipole, i.e. parallel to the x,y plane, and for TM modes the power density is given by:

$$K_H^{\mathrm{TM}} = \frac{3}{4} \Re \left[ \frac{\kappa^2}{k_e^3 k_{z,e}} \frac{(1 + a_+^{\mathrm{TM}})(1 + a_-^{\mathrm{TM}})}{1 - a^{\mathrm{TM}}} \right], \tag{2.72}$$

where $k_e$ is the wave vector in the emitter layer, $k_{z,e}$ is the z-component of the wave vector in the emitter layer and $a$ is the reflection coefficient referenced to the dipole location:

$$a_-^{\mathrm{TM}} = r_-^{\mathrm{TM}} \exp(2ik_{z,e}z_+) \tag{2.73}$$

$$a_+^{\mathrm{TM}} = r_+^{\mathrm{TM}} \exp(2ik_{z,e}z_-) \tag{2.74}$$

$$a^{\mathrm{TM}} = a_+^{\mathrm{TM}} a_-^{\mathrm{TM}}, \tag{2.75}$$

where $z_- = h$ and $z_+ = t_d - h$. Any dipole angle $\theta$ the power density $K_{theta}$ can be calculated using:

$$K_{theta} = K_V \cos(\theta)^2 + K_H \sin(\theta)^2 \tag{2.76}$$

where $K_V$ is the power density for an vertical dipole. The power density $P$ per unit solid angle can be found from the power density $K$ by:

$$P(\alpha_+) = \frac{k_+ \cos(\alpha_+)}{\pi} K_{+,T} \left( k_+ \sin(\alpha_+) \right), \tag{2.77}$$

where $\alpha_+$ is the angle of the wave vector with respect to normal in the top layer, $k_+$ is the wave vector in the top layer and $K_{+,T}$ is the power density transmitted trough the top layer.

A dipole along the [111] axis in diamond makes an angle of $\theta = 54.7°$ with the (100) plane, and this is true for all of the four orientations in the $\langle 111 \rangle$ family. We use two dipole vectors to span the (111) plane. One dipole vector is horizontal, and the other dipole vector is at an angle of $\theta = 35.3°$. Here, we calculate four dipole orientations: vertical, horizontal, along the [111] axis and at an angle of $\theta = 35.3°$.

For $\frac{\kappa}{k_0} < 1$ the modes are propagating in the z direction and for $\frac{\kappa}{k_0} > 1$ the light is evanescently decaying in the z direction. In these modes the light stays inside the diamond layer due to total internal reflection. Here, we refer to these modes as diamond modes, which can be seen in figure 2.11.
In general we find that a large fraction of the emitted light for all dipole orientations couples into diamond modes. All results are shown in table 2.1.

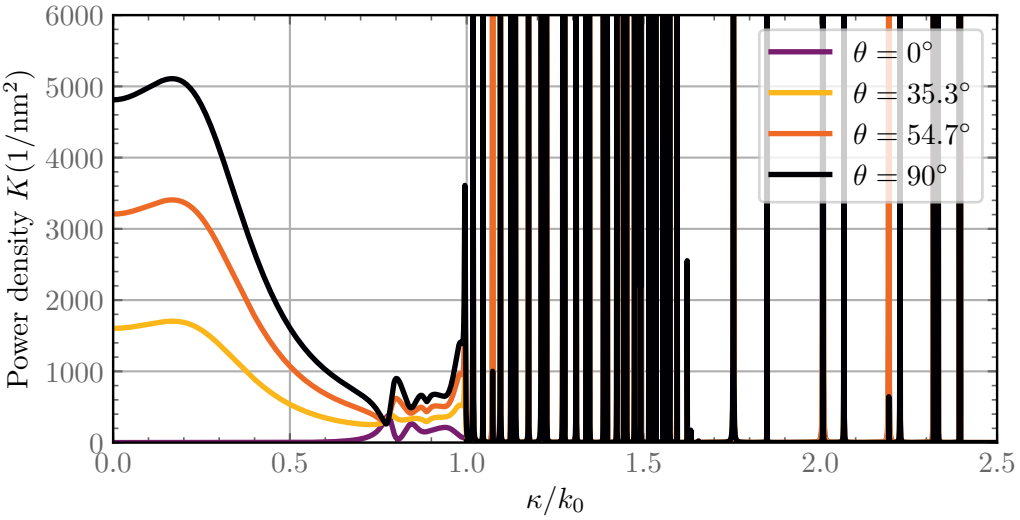


Figure 2.11: Power density as a function of $\kappa$ for four different dipole orientations.

Taking the average of the collection efficiency from the two dipole vectors that span the (111) plane gives 7.5%, which is the same as for the [111] dipole. 7.5% will be our best estimation for the collection of emitted light into the objective.

| Dipole $\theta$ | Diamond modes (%) | -z dir. (%) | Not collected (%) | Collected (%) |
|---|---|---|---|---|
| 0° | 95.9 | 3.4 | 0.6 | 0.0 |
| 35.3° | 86.5 | 8.4 | 1.3 | 3.8 |
| 54.7° | 77.5 | 13.2 | 1.9 | 7.5 |
| 90° | 68.8 | 17.7 | 2.5 | 11.0 |

Table 2.1: Directional emission of four different dipole orientations. The directions are divided into four categories; diamond modes, light traveling in the negative z-direction (and therefore into the mirror), light traveling in the positive z-direction but not into the objective and light collected by the objective.

Horizontal dipoles give the best collection efficiency into the objective. The NA of the objective is 0.7, which corresponds to a collection angle of 44° in air. Figure 2.12 shows the power density going in the positive z direction. From figure 2.12 we can see that we have collected the main parts of the emitted light that leaves the diamond in the upwards direction. Figure 2.13 shows that we are getting a collection efficiency of 7.5% out of the 9.4% possible with a $\pi/2$ NA objective. Figure 2.14 shows the emission of a horizontal dipole in polar coordinates.

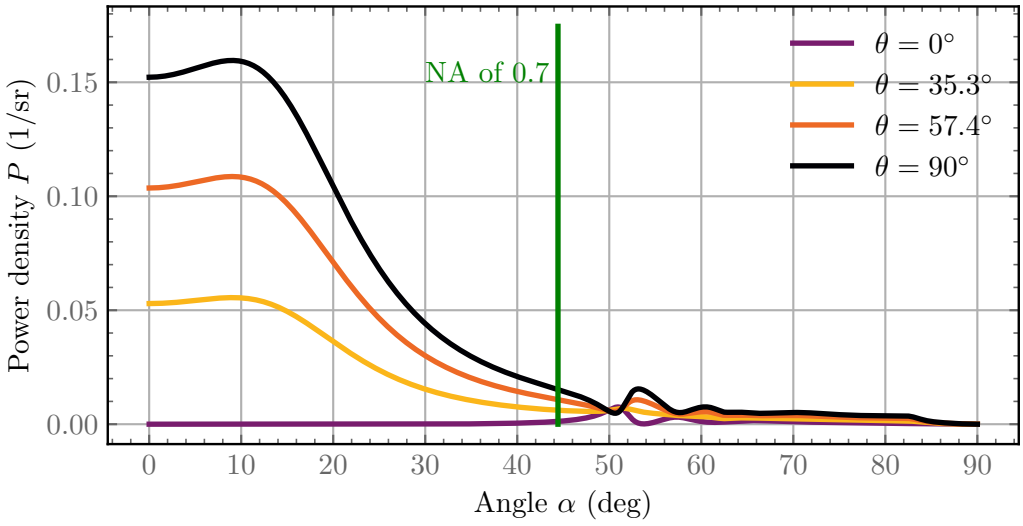


Figure 2.12: Power density in the positive z direction as a function of $\alpha$ for four different dipole orientations. All light with an angle smaller than 44° is collected by the objective.

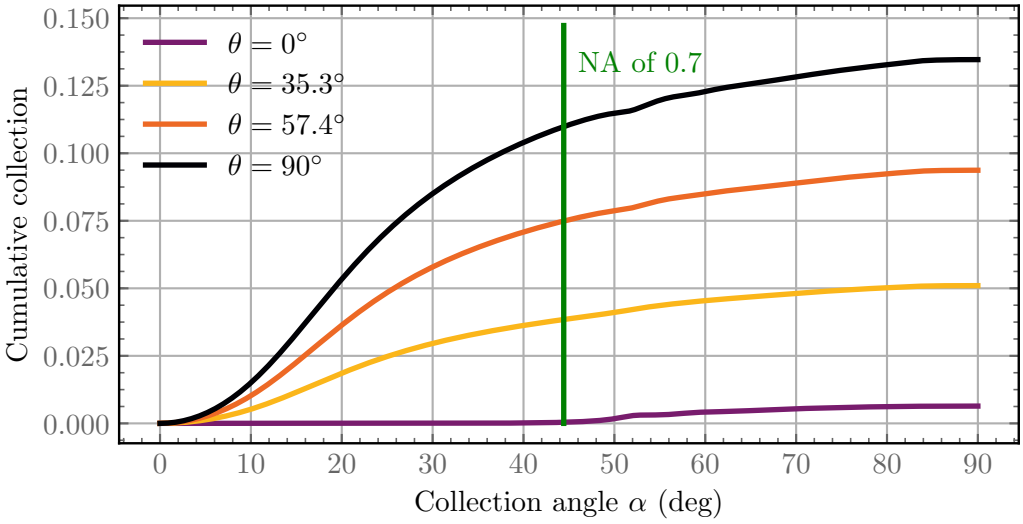


Figure 2.13: The collection efficiency of a dipole at different orientations in the diamond. All light with an angle smaller than 44° is collected by the objective.

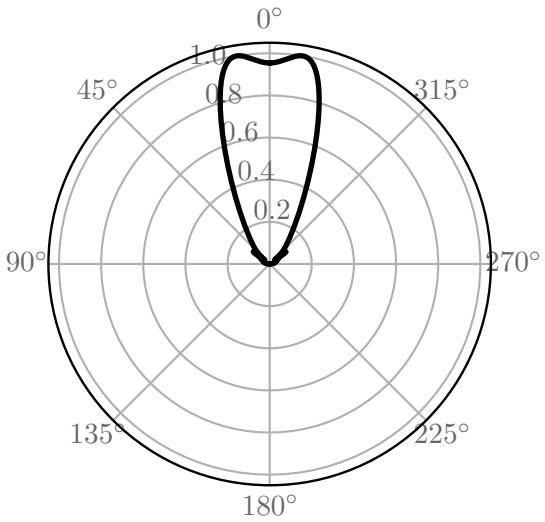


Figure 2.14: Normalized dipole emission pattern for a horizontal dipole on a DBR mirror stack.

# Chapter 3

# Experimental techniques

This chapter introduces how the experiment was designed, built and operated.

## 3.1 Micro-cavity design

Our design goal was to create a stable high finesse micro-cavity that could facilitate a diamond membrane containing bulk-like emitters and that could function at room and at cryogenic temperatures. We chose a fiber based Fabry-Pérot cavity as shown in figure 3.1. Using a fiber mirror, as one of the mirrors of the cavity, allows for good coupling efficiency between the cavity mode and the fiber mode, since both are Gaussian modes. Further, the fiber is an excellent waveguide, which makes it easy to direct the light into a detector. The small footprint of the fiber end-facet (125 µm) allows for stable and short cavity lengths (small mode volumes of a few $\lambda^3$) even with imperfect tip/tilt angle alignment compared to the bulk flat mirror.

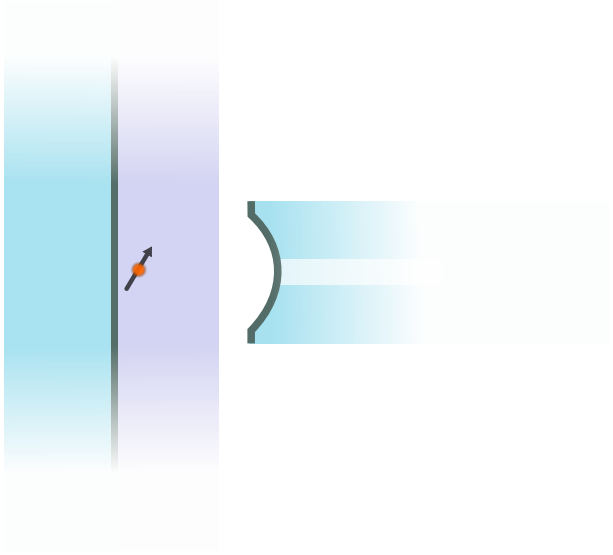

Figure 3.1: Fiber based Fabry-Pérot cavity. A bulk mirror is shown in blue on the left with a diamond membrane in purple. The GeV center is shown as an arrow in the diamond membrane. A concave fiber mirror is shown on the right.

The reason for using a bulk flat mirror as the other mirror of the cavity, as opposed to two fiber mirrors, is that the large surface of the flat mirror allows for easy incorporation of the relatively large (∼1×1 mm) diamond membrane. The diamond membrane was simply bonded to the mirror by van der Waals forces. To have a stable cavity mode we made one of the mirrors concave. We chose to make the fiber mirror concave such that our GeV center would be positioned in the focus of the beam, which optimizes the coupling between the GeV center and the cavity mode. Our super-polished substrates and fibers were coated, using state of the art coating technology, which enabled micro-cavities with very high finesse (>100000) [29].

## 3.2 Fiber mirror fabrication and characterization

The fiber mirror is critical for the performance of the entire experiment. The shape of the mirror is important for the spatial cavity mode and therefore for the mode volume. The smoothness of the surface together with the coating quality determine the achievable finesse.

We used a $CO_2$ laser to make Gaussian shaped ablations on the end-facet of our fibers. The technique was first reported by the Riegel group [29, 30]. By using short high power laser pulses we produced concave surfaces on the end-facet of the fibers with low radius of curvature (ROC) and smooth surfaces. Other techniques have also been used to make very small ROC mirrors, such as focused ion beam (FIB) milling [28, 73].

The shape of the fiber mirror is characterized by the radius of curvature of the mirror and the ablation depth, see figure 3.2. The ROC determines the focus of the Gaussian mode and the ablation depth determines the minimum cavity length.

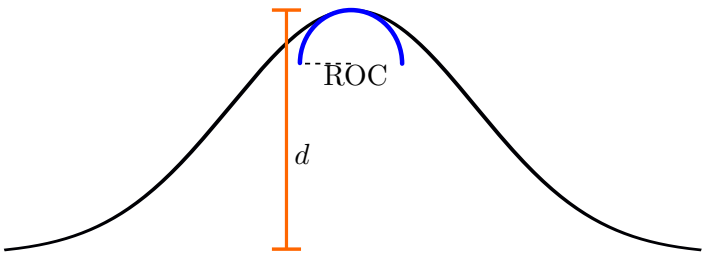


Figure 3.2: Shape of a Gaussian ablation, black curve. Definition of radius of curvature (ROC), see dashed line, and ablation depth $d$, see red line.

There is a trade-off between the ablation depth ($d$) and ROC when using a $CO_2$ laser to create the concave ablation in fiber glass [30]. If one tries to make a shallow (small $d$) ablation the ROC typically becomes larger and vice versa.
We used the bare 630HP fiber from Thorlabs together and our general protocol to make the fiber mirrors. The steps in the protocol were:

1. Prepare ∼ 40 bare fibers for structuring by stripping and cleaving the fibers.
2. Laser machine concave structures on end-facet of the fibers.
3. Characterize the surface with white light interferometry.
4. Coat fibers with dielectric high reflective (HR) coating.

### Preparation of the fibers

The fibers were prepared by stripping off their protective dual acrylate coating to avoid contaminating the coating chamber. Initially, we only stripped the tip of the fiber which was exposed in the chamber. Keeping the protective layer on most of the fiber made the fiber less fragile and easier to handle. However, the remaining protection layer of the dual acrylate coating material was melting during the coating process, which meant that the fibers were sticking together and had to be mechanically pulled apart. This broke many of the fibers and resulted in a low yield of functional fibers.

To avoid that the fibers melted together we tried to use fibers with a protective metallic coating. However, the metallic coated fibers were hard to work with, since they did not relax structurally. The best strategy was to strip the entire acrylate coated fibers in terms of highest yield and handling. The cleaving was done with a standard fiber cleaver with a diamond blade. The first contact point of the blade was often seen on images of the fiber end-facet. During the fiber preparation a lot of care was taken into maintaining a clean environment.

### $CO_2$ laser ablation of the fiber end-facets

Glass has a high absorption coefficient at the emission wavelength ($\lambda_{CO_2} = 10.6\mu m$) of a $CO_2$ laser. Short high intensity laser pulse trains evaporate and melt glass. The melting of glass gives smooth surfaces well suited for high reflectivity coatings. We used a Firestar $CO_2$ air-cooled pulsed laser with custom made PID powerlock for the ablation. The $CO_2$ laser beam was expanded with a telescope before reaching a focusing lens, which created a tight focus onto the fiber surface. A modified hard drive was used as a fast shutter to chop the $CO_2$ beam into short ($\sim ms$) pulses. A custom microscope was used to position the fibers in the center of the beam.
More advanced protocols have also been used to obtain a smaller ROC, ablation depth [79] and a smaller mode volume by tapering the fiber tip [34].

### Fiber surface characterization

To characterize the shape of the ablation we used a white light interferometer, which was a fast way to characterize many fibers compared to atomic force microscope (AFM) measurements. However, the AFM measurement was useful to determine the RMS surface roughness. For the white light interferometry, a special interferometric objective (Nikon Objective CF Plan DI 20xA) with an internal reference plane was used to image the fibers. The images were fitted using a fitting algorithm that extracts radius of curvature, ablation depth, ellipiticity and offset from the center of the fiber [80].

### Dielectric mirror coating of fibers and bulk flat substrates

Thin film deposition of dielectric materials was used to make high reflective DBR mirrors. The coating consisted of alternating layers of high refractive index and low refractive index materials, $TA_2O_5$ and $SiO_2$, respectively. The layer thicknesses of the thin films were determined from design parameters. We designed our flat mirror coatings to be transmissive for our excitation wavelength of 532 nm. The fiber mirror was highly reflective for 532 nm to prevent high power in the fibers leading to

unwanted fluorescence [73].

Both the flat and the fiber mirrors were designed to be highly reflective for the color center emission wavelength. The mirrors can be chosen to be asymmetric by design to ensure that light is either going through the fiber mirror or the flat mirror depending on the experiment. The finesse should be chosen such that other cavity losses, e.g. scattering and absorption losses, do not become the dominating loss channel. If these losses are too high no photons will escape from the cavity.

Another important consideration is whether the mirror should be low index terminated or high index terminated, i.e. if the last layer of the coating should be $TA_2O_5$ or $SiO_2$. The best choice depends on the mode type and on the type of losses in the cavity [70]. We chose a low index terminated flat mirror such that the diamond membrane increased the reflectivity of the flat mirror. This also meant that we were very sensitive to scattering losses at the surface of the diamond membrane, since there was an electric field antinode at the mirror diamond interface.

The fibers were shipped to a coating company for high reflectivity coating. The fiber container was first shipped empty for pre-coating and was then loaded with fibers. It is important that the fibers are clean before the coating run to avoid contamination of the chamber and to avoid dust particles during the coating. Some of our coating runs gave a low yield of useful fibers due to contamination of the fibers, see figure 3.3. At DTU, we used Layertec in Germany as a coating company, but so far with poor results in our coating runs. The reason is still unclear. At McGill University, they used LaserOptik in Germany and their coating runs matched the expectations.

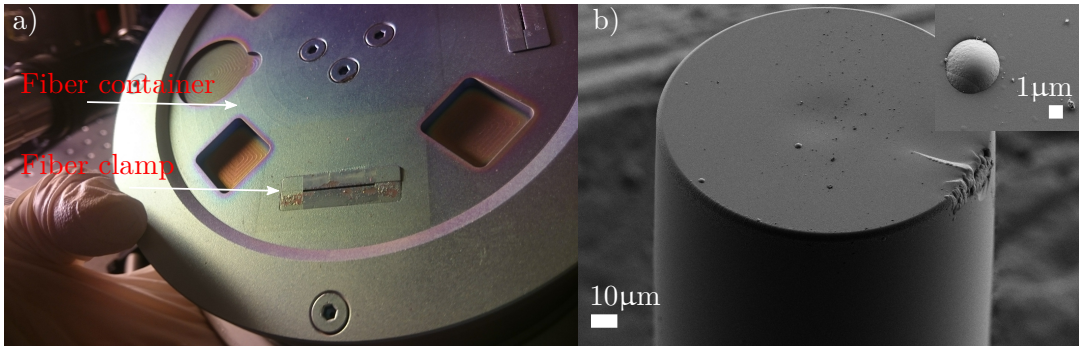


Figure 3.3: a) Fiber container with coating scraped of near the fibers in the fiber clamp. b) Scanning electron microscope (SEM) picture of a coated fiber that was contaminated with dust and has lumps. The insert shows one of these lumps.

After the mirror coatings, the fibers and flat mirrors were annealed for 5 hours under atmospheric conditions at 300°C to reduce absorbtion and scattering losses in the coating [81].

### Connectorizing fibers

Often, it is very convenient to have a connector at the end of the cavity fiber to connect to other fibers, fiber coupled phase modulators, fiber coupled avalance photo diodes (APDs), etc. Initially, we manually connectorized our fibers to fiber coupler angle physical contact (FC/APC) fiber connectors. This was done by gluing the fiber

in the ferule with epoxy and afterwards polishing the end-facet for excess glue. The advantage of this technique is that it does not add any loss in the fiber. The polishing process requires the moving of a fiber connector with a puck over polishing paper several times. To do this movement, while protecting the fiber mirror on the opposite end of the fiber, was challenging. We quickly found out that this process was impractical with our short (∼20 cm) coated fibers.

Instead, we used a fusion splicer and spliced our cavity fibers to a short commercial FC/APC connectorized fiber (also known as a pigtail). This method was faster and more convenient. The typical loss in a splicing was around 0.02 dB. Others have also found that this method is optimal to minimize reflection from the end-facet [42].

**Handling and cleaning of the fibers**

The striped fibers were fragile and broke easily. We found out that moving the fibers in a V-groove fiber clip (Thorlabs -VHM100), by holding on the clip and not the fiber, made the handling easier. Sometimes, unwanted dust particles contaminated the fiber mirror. Most of the times we could remove the dust by carefully swiping lens paper with ethanol across the fiber tip.

## 3.3 Diamond membrane fabrication

The diamond membrane fabrication was done by our collaborator Erika Janitz from McGill University, Canada. The diamond membrane should be very thin in order to obtain a small mode volume. The diamond surface should be ultra smooth to avoid that scattering losses became our dominant loss channel in the micro-cavity.

The diamond membrane used in the following experiment was made from an $< 100 >$-cut electronic grade bulk diamond purchased from Element 6. The diamond was laser cut into ∼20 µm thick membranes and polished by Diamond Delaware Knifes. A Piranha solution was used to clean the membranes, which were then transferred on to sapphire wafer. The thin membranes were bonded via Van der Waals forces on the wafer. The ∼20 µm membranes were then thinned down to ∼4 µm using a cycled $ArCl_2$ and $O_2$/Ar dry etch [82–84]. This etching was done to relieve strain at the surface of the diamond and to smoothen the surface to around 0.3 nm RMS.

The diamond membranes were shipped to Innovion Corp. for Ge implantation in order to create GeV centers in the diamond membrane. The implantation depth was chosen such that it coincided with the first antinode of the electric field in the cavity: $\frac{\lambda}{2n_d} \approx 125$ nm, where $n_d$ is the refractive index in diamond and $\lambda$ is the emission wavelength of the GeV center. The implantation energy was 330 keV and the dose was $1 \cdot 10^9$ ions/cm$^2$ for the diamond that we used in the micro cavity. The implantation dose and energy were calculated using the SRIM software [85] to ensure an implantation depth of $125 \pm 20$ nm of the Ge ions. Triacid cleaning was done using equal amounts of sulfuric, nitric and perchloric acids to remove any graphitization. Annealing was done at three different temperatures, which has been shown to improve conversion efficiency and spectral diffusion [25].

Another triacid cleaning was done before the final etch. The diamond membranes were flipped and etched on the side without the GeV centers to around $\approx 1$µm using

the same cycling dry etch procedure as described above.

The thin membranes, with very smooth surfaces, bonded strongly to the sapphire wafer. Boiling piranha was used to unbound the membranes, which were then rinsed in DI water. One membrane was then transferred to the flat mirror in a water droplet since it was too fragile to move with tweezers. We looked at the diamond membrane on the flat mirror in an optical microscope to make sure that the implanted side was down towards the mirror. Residual water from the droplet was removed by blow drying with nitrogen.

Examples of fabricated membranes are seen in figure 3.4. The membranes sometimes appear rough on large millimeter scale. The diameter of the cavity mode in our experiment was $\sim$ 3 µm, which means that the roughness of the sample should be judged on this micrometer scale.

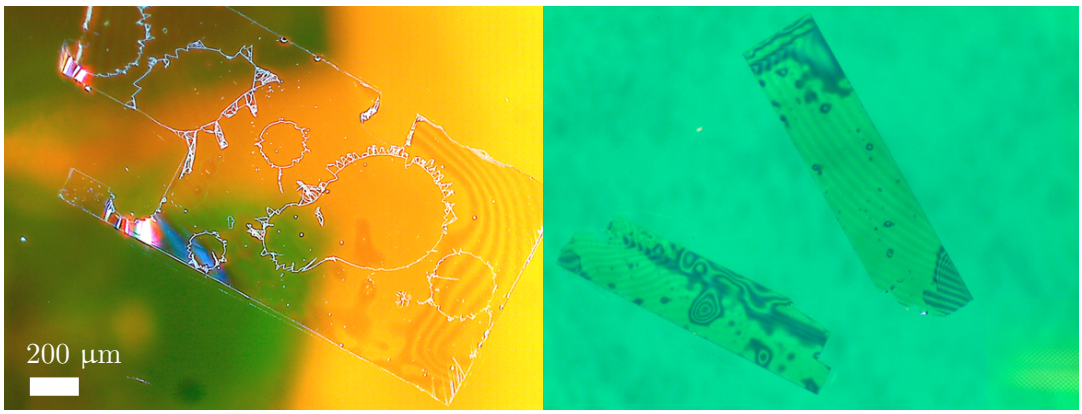


Figure 3.4: Diamond membranes on DBR mirrors imaged using an optical microscope.

## 3.4 Confocal microscopy

To show the change in the GeV center emission when it is coupled to the micro-cavity, we first investigated the GeV center in free space using a confocal microscope. In this work, a GeV center in free space means a GeV center outside the cavity, but still in the diamond membrane on the flat mirror. The design of our home-made confocal microscope was chosen such that minimal changes needed to be performed when switching back and forth between the cavity setup and the confocal microscope setup. The confocal mircoscope setup is shown in figure 3.5.

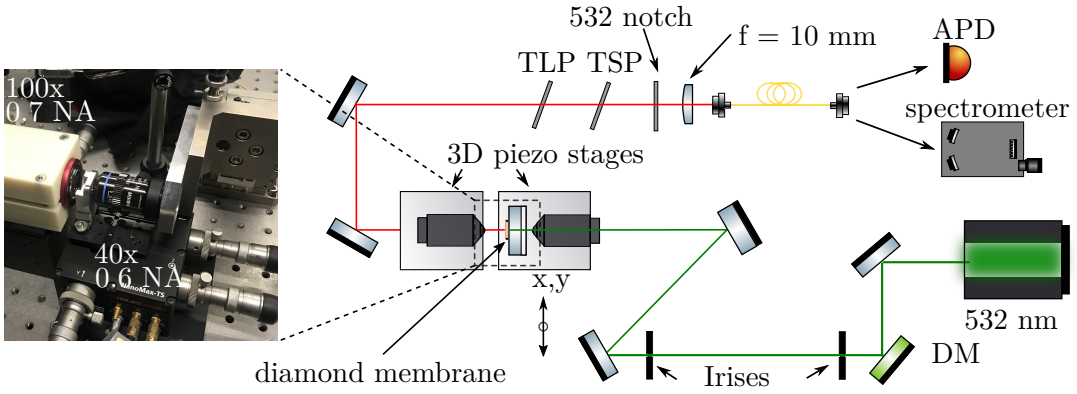


Figure 3.5: Experimental setup of the confocal microscope, which we used for studying GeV centers in free space. TLP: tunable long pass, TSP: tunable short pass, DM: dichoric mirror, APD: avalanche photo diode.

The flat mirror with the diamond membrane was mounted on a custom designed 1/2-inch aluminium mirror mount (jig). The jig and the collection objective were mounted on 3D piezo stages (Thorlabs NanoMAX 311D/M). The GeV centers were excited with a 532 nm laser from the backside through the flat mirror. We used a 40x 0.6 NA Olympus (LUCPLFLN 40x) objective with a 2 mm correction collar to focus the excitation light on the diamond membrane. The collection of the emission light was done from the front side of the flat mirror using a long working distance 100x 0.7 NA objective from Mitutoyo (Plan Apo NIR HR). We used two tunable filters (Semrock TLP01-628, TSP01-628) to bandpass filter the emission light and a 532 nm notch filter (Semrock NF01-532U-25) to ensure that none of the excitation light was going into the detector. We used an achromatic lens with a focal length of 10 mm (Thorlabs AC060-010-A) to focus the emission light down into a single mode (SM - 630HP) or multimode (MM) fiber. This collection fiber acted as the pinhole in our confocal microscope. The emission light could both be directed to one or two APDs (Micron Photon Devies - PD050CTE) or to a spectrometer (Andor SR500i with a Newton Newton DU970N-FI camera), which enabled us to do both spectral and photon counting measurements.

We used the modular software package Qudi [86] to control all the hardware: National Instruments (NI) data acquisition card (PCIe-6323), spectrometer, camera and oscilloscope (Keysight DSOX3024T Oscilloscope). Qudi logic modules were developed to connect to multiple hardwares to enable fully automated measurements. Furthermore, Qudi graphical user interfaces (GUIs) were developed for easy control of the experiment.

We have both used an SM and an MM fiber in the collection path. More light was collected with the MM fiber at the expense of resolution, since the fiber functioned as a pinhole in the confocal microscope and therefore defined the collection volume. Typical confocal images are shown in figure 3.6. From figure 3.6 it is clear that the GeV centers are better resolved when using the SM fiber in the collection path compared to using the MM fiber.

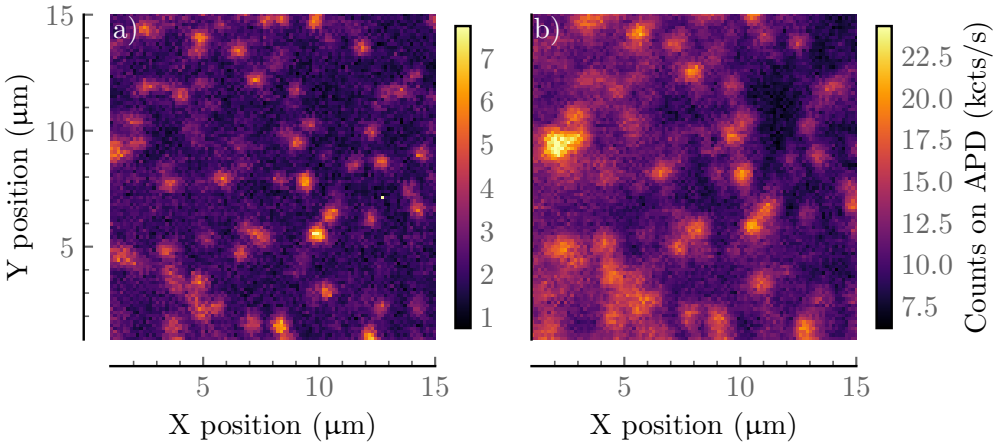


Figure 3.6: Confocal images of the diamond membrane on the flat mirror. a) With single mode collection fiber and 5 mW of excitation power. b) With multimode collection fiber and 4 mW of excitation power.

We studied several GeV centers with saturation measurements, lifetime measurements, $g^{(2)}$-measurements and spectral characterization using the configuration with the SM fiber in the collection path.

### 3.4.1 Saturation measurements

A saturation measurement maps out the population of the excitation state of the GeV center. The measurement was done by changing the excitation power from 0 to 19 mW in 1 mW intervals by using a half wave plate and polarizing beamsplitter. The saturation measurement was done for the GeV center as well as for the background. For each excitation power 350 measurement points were taken with an integration time of 20 ms each. We used the average and one standard deviation as the result.

### 3.4.2 Dynamical investigations

For lifetime and second order correlation measurements we used a pulsed 532 nm laser with a repetition rate of 5 MHz. The pulsed laser was co-aligned with the 532 nm continuous wave (CW) laser and the typical pulsed length was 4-6 ps, which is much shorter than the GeV excited state lifetime. First, we took a confocal image with the pulsed laser to make sure that we were still addressing the same GeV center. Often, the confocal images were shifted ∼1 µm due to different alignment of the pulsed and CW lasers.

To measure the excited state lifetime, we needed to get a trigger that was synchronized with the excitation of the GeV center. To get an excitation pulse time reference, we tapped off some of the pulsed excitation light with a beamsplitter and measured the tapped off light with a photodetector (PD). The signal from the PD was sent to a fast counter (PicoHarp 300) and was our start signal.The signal from the APD, that detected the GeV center emission, was our stop signal. The time difference between the start and the stop signal would be binned into 256 ps intervals and we created

a histogram with the events. By fitting the histogram the excited state lifetime was determined.

For our second order correlation measurements the GeV emission was split with a 50:50 beamsplitter and sent to two APDs. The APDs were connected to the PicoHarp, but they had different lengths of electrical cables which introduced a time offset. The signal from one APD was the start signal and the signal from the other APD was the stop signal. Again, the time difference was recorded and binned. We found that it was necessary to use FC/APC fibers in our collection path to avoid reflections in the fibers. Reflection in the fibers led to unwanted peaks in our histogram that were correlated to the fiber length.

### 3.4.3 Spectral measurements

We used a fiber connected spectrometer with an electron-multiplying CCD (EMCCD) camera that was cooled to -75°C. To calibrate the spectrometer we used an attenuated narrow linewidth laser with a well known wavelength and we adjusted the fiberport until the right wavelength was measured. Noise was removed by subtracting a measurement where the input fiberport was blocked. An example of such measurement is shown in figure 3.7.

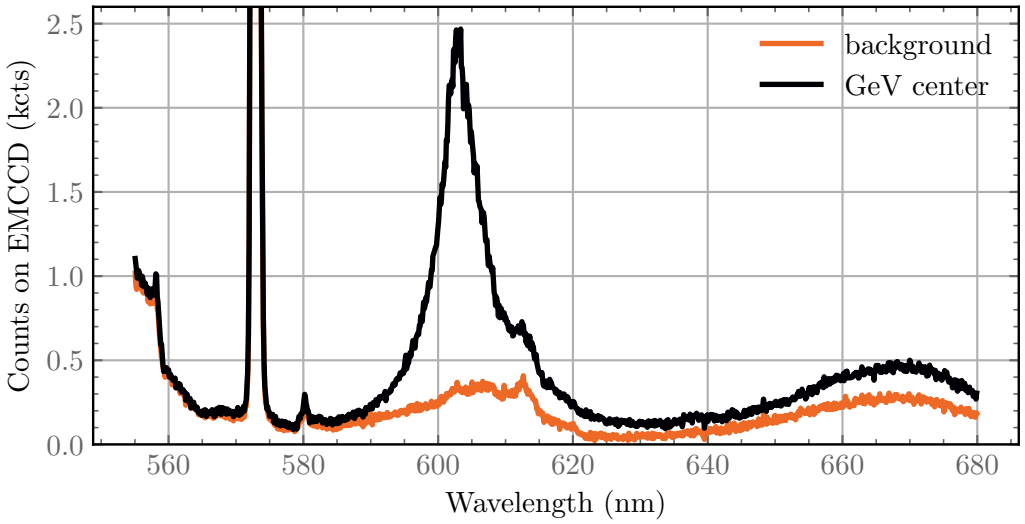


Figure 3.7: Spectrum measurement of a GeV center and a background measurement next to the GeV center in the confocal setup. A sharp Raman peak is seen at 572 nm and the GeV emission is seen around 603 nm.

These two measurements were taken with five acquisitions of 300 seconds and 19 mW of green power. We used a 532 nm notch filter to make sure that none of the high power excitation light was going into the spectrometer. In figure 3.7, the diamond Raman peak at 572 nm is clearly visible [61, 87] and the GeV center has a clear spectral peak around $\sim$ 603 nm.

## 3.5 Cavity experiments

The optical experimental setup for our cavity measurements is shown in figure 3.8. Compared to the confocal setup we have switched the collection objective with the mirror coated fiber in the cavity setup.

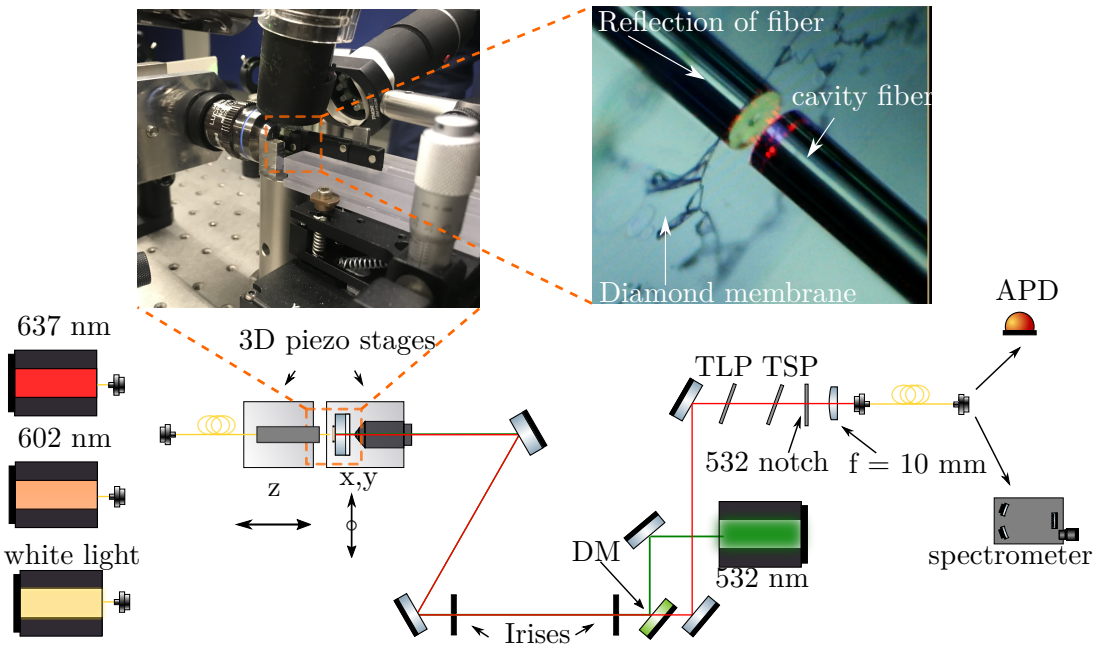


Figure 3.8: Experimental optical setup for the fiber cavity experiments. TLP: tunable long pass, TSP: tunable short pass, DM: dichoric mirror, APD: avalanche photo diode. The fiber was scanned in the z-direction to change the cavity length, and the flat mirror with the diamond membrane was scanned in the x and y direction to position a GeV center inside the cavity mode.

The fiber was mounted with a fiber V-grooves clip on a NanoMax piezo stage with a tip tilt stage. We used two USB microscopes, one from the top and one from the side, to align the tip and tilt angle of the fiber. This was done by placing a ruler on the computer screen and make sure that the fiber and its reflection lined up, see figure 3.9. A strain gauge reader was connected to the Nanomax piezo stage to track the piezo position and to correct for any non-linearity of the piezo.

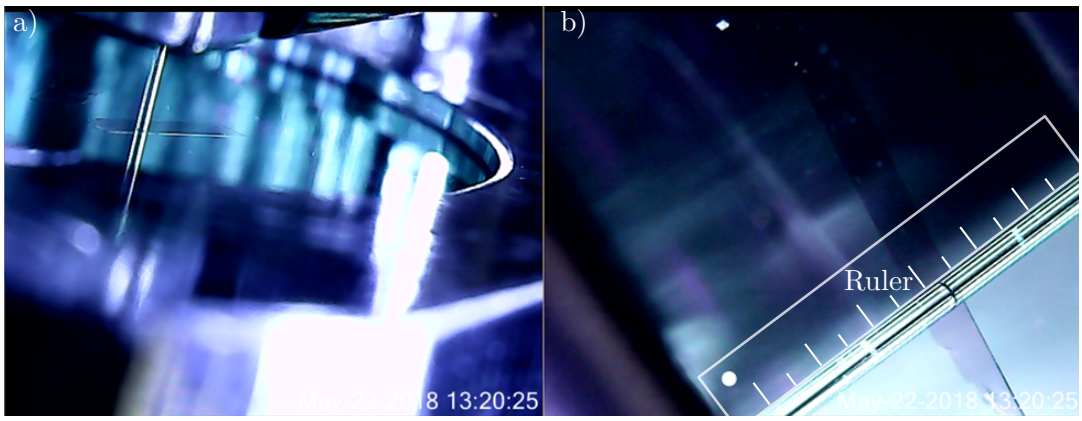


Figure 3.9: A screenshot of the images from two USB microscopes. We used a mircoscope from the side of the cavity (figure a) and from the top of the cavity (figure b). We adjusted the angle of the fiber with a tip and tilt stage. A ruler on the computer screen was used to achieve good alignment.

The GeV emission was not collected through the fiber, as originally intented, since too much parasitic fluorescence was generated in the fiber at the emission wavelength of the GeV center [31]. The fiber transmission was ∼0.1% for 532 nm light, which meant that the cavity fiber would guide up to 10 µW of 532 nm light during our cavity experiments. Impurities and doping in the fiber were excited by the green light which generated light at the emission wavelength of the GeV center. Therefore, the GeV emission light drowned in background. As a results, we chose to collect the emission light from the flat mirror.

We used a dichroic mirror (DM) to separate the excitation light from the emission light. Afterwards, the emission light was guided into the same detection path as we used in the confocal setup. We used three different light sources, which we fiber coupled such that we could easily connect them to the cavity fiber. A white light source (NKT SuperK COMPACT) was used to study the cavity modes and align the detection path. A home-build 602 nm light source was used to measure the finesse at the emission wavelength of the GeV center. A 637 nm laser (Toptica) was primarily used for alignment purpose.

Aligning the green excitation laser to the center of the fiber was challenging. The rough alignment was done by defocusing the objective and looking at the reflected green light. We used a piece of paper with a hole and placed it in front of the objective rear aperture to ensure that the green light did not get blocked, see figure 3.10. We could see the membrane and the fiber from the back reflection of the green light. Thereby, we kept track of which areas on the membrane we were investigating, i.e if we were in a bonded region or not. Afterwards, we sent white light trough the cavity fiber and aligned it to the back reflected green light in the far field. Last step was to connect the cavity to a power meter and optimize the green power in the fiber while scanning the fiber.

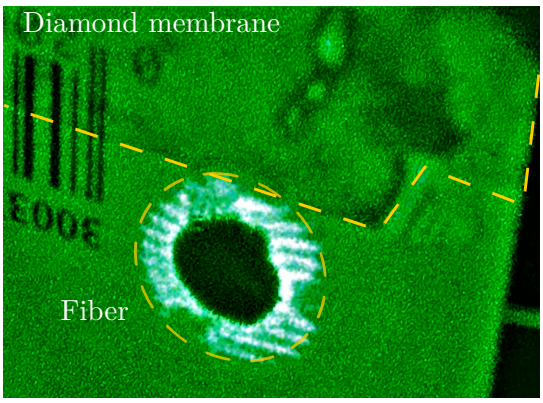


Figure 3.10: Green reflection from the fiber and the diamond membrane. A piece of paper with a hole in it was used to see the relative position of the fiber to the membrane. Furthermore, we could keep track of which part of the membrane we investigated.

When the fiber and the green excitation light were aligned we wanted to find a low loss area where the diamond membrane surface was smooth. This was done by moving the flat mirror with the diamond membrane in the x,y direction while scanning the cavity length and looking at the resonance contrast in reflection using a 637 nm laser (due to logistical challenges, the 602 nm laser was not available at all times). When we found an area with high resonance contrast we moved to white light measurements.

### 3.5.1 White light measurements

White light measurements were carried out to determine the diamond thickness and the cavity length. We filtered the white light from 600 to 700 nm and sent it through the cavity fiber and removed the tunable filters. We scanned the fiber while recording the spectrum. We used an NI card to synchronize the white light measurements. The NI card sent TTL signals to the spectrometer, read an analog input signal from the strain gauge reader and send analog output signals to the piezo controllers. All these signals used the same hardware clock, which allowed for fast measurements. An example of a white light measurement is shown in figure 3.11. We fitted the data to our transfer matrix model and then determined the cavity length and diamond thickness. It was also clear from such a measurement if the fiber touched the diamond membrane.

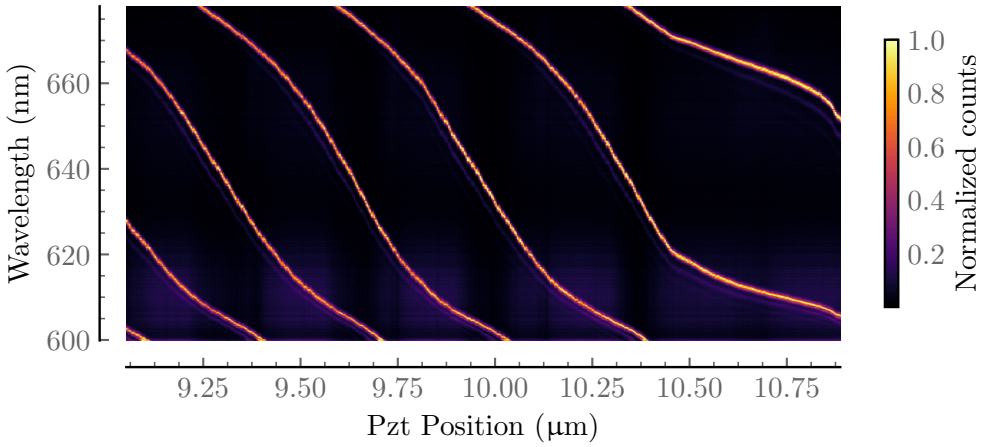


Figure 3.11: Example of a white light measurement. The piezo (pzt) position is read from a strain gauge. Higher position corresponds to a shorter cavity. At around 10.4 µm the fiber touched the diamond membrane. The nonlinear resonances are due to the hybrid diamond air cavity.

### 3.5.2 Cavity linewidth and finesse characterization

Two methods were used to determine the cavity linewidth. We measured the linewidth in length $\Delta L$ and in frequency $\Delta\nu$.
We measured $\Delta L$ by scanning the cavity length over at least one free spectral range and recorded the transmission of the cavity with a PD, which was connected to an oscilloscope. We used the free spectral range $\frac{\lambda}{2}$ as a reference length to convert the time scale on the oscilloscope into a length scale. Then $\Delta L$ and the finesse in length $F_L = \frac{\lambda}{2\Delta L}$ were determined. This measurement was sensitive to instability of the cavity length over the measurement time ($\sim$ 1 sec). Therefore, special care was taken into scanning the fiber at a frequency that did not excite any mechanical modes of the fiber.

The cavity linewidth in frequency was measured much faster ($\sim$10 µs) and was therefore less sensitive to low frequency cavity length fluctuations. A phase modulator was used to generate sidebands on the laser carrier. We measured the transmission and scanned the cavity length across a resonance. An example of a linewidth measurement is shown in figure 3.12. The sidebands are resonant at a slightly different length than the carrier, which creates three peaks in the transmission of the cavity resonance. Since the modulation frequency $\nu_m$ was known we could use this as a frequency reference. The linewidth was then determined by comparing the distance between the carrier to a sideband.
Unfortunately, our phase modulator had a narrow bandwidth and we could only use it for our 637 nm laser and not for our 602 nm laser.

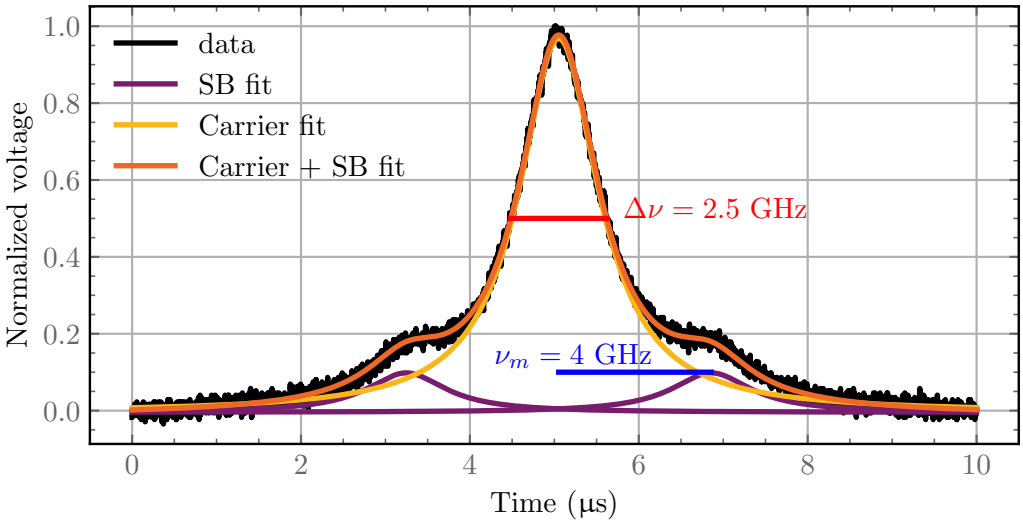


Figure 3.12: Example of linewidth in frequency measurement. The 637 nm laser was modulated with a phase modulator at a modulation frequency $\nu_m$ of 4 GHz which created two sidebands (SB). The sidebands were used as frequency reference to obtain the linewidth. The transmission of the cavity was measured while scanning the cavity length across resonance.

### 3.5.3 Spectrum of a GeV center in a micro-cavity

To obtain the spectrum of the GeV center inside the cavity we had to scan the cavity length while recording the spectrum. We used our white light technique as described above. However, we had to increase the integration time at each cavity length step to accumulate enough counts. Being more sensitive to cavity length drift, we often ran these measurements at night, where the cavity drift was minimal. An example of a spectrum of a GeV center taken with an MM detection fiber is shown in fig 3.13. All the higher order modes, which the GeV center also couples to, became visible with the MM detection fiber.

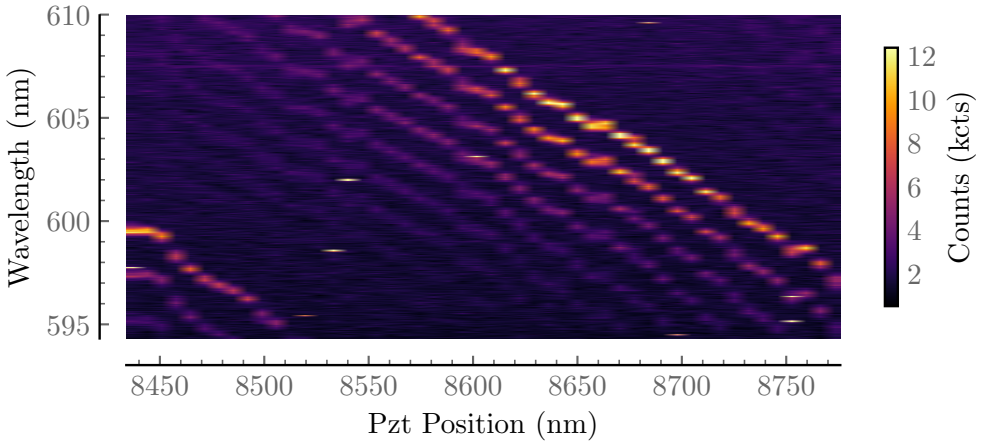


Figure 3.13: Spectrum from a GeV center coupled to cavity modes. An MM fiber was used in the detection path, which makes all the higher order cavity modes visible. The spectrum was recorded while the cavity length was scanned.

### 3.5.4 3D cavity scans

Since we were collecting the emission signal from the backside of a highly reflective mirror there would not be an emission signal from the GeV centers unless the cavity was on resonance with the GeV emission. For NV centers the broad PSB can be detected for wavelengths outside the bandwidth of the mirror coatings. This is, however, not possible for the GeV center since the entire emission spectrum lies within the bandwidth of the mirror coating. Here, we used a 3 dimensional scanning to detect the GeV center. For each x,y position the cavity length was scanned one free spectral range. An example of such a length scan is shown in figure 3.14.

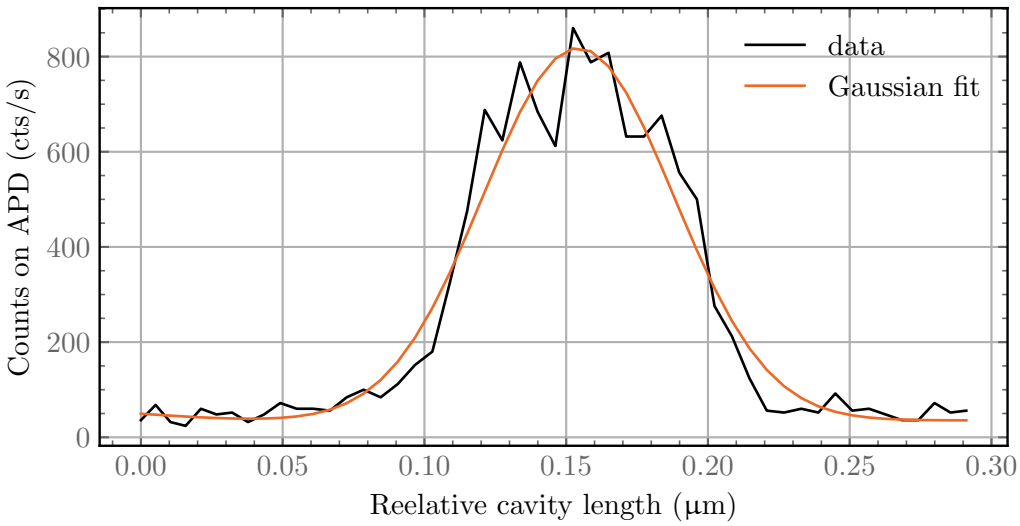


Figure 3.14: Example of cavity length scan with 19 mW of green excitation. The position is read as an analog signal from a strain gauge reader.

The integration time for each measurement position was 250 ms and we typically used a step size of 6 nm. To make sure that we stayed on the same longitudinal mode number we fitted each length scan to a Gaussian function, and then corrected the following length scan for any drift and mirror tilt by centering the next length scan on the center of the previous Gaussian function. There were significant cavity length drifts during the measurement time, which typically lasted several hours.
The contrast (the maximum-minimum) of length scan is shown as a single pixel in a 3D scan image, see figure 3.15.

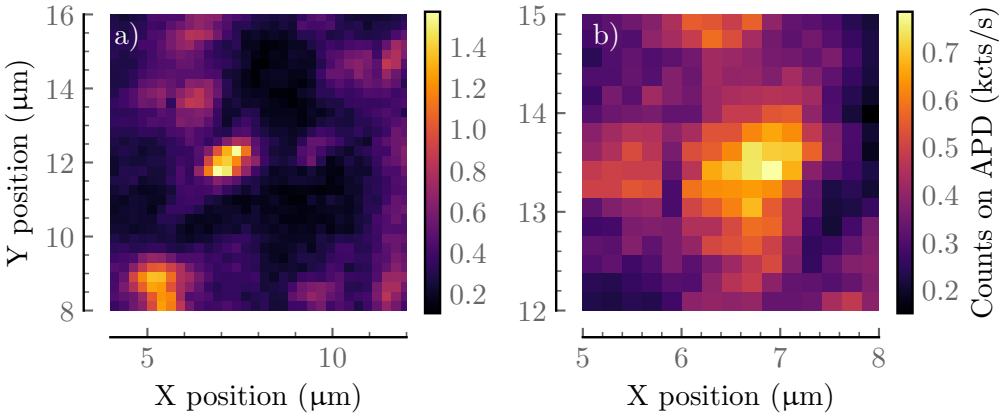


Figure 3.15: 3D scans of the diamond membrane taken at 19 mW of green excitation power. Each pixel is the maximum-minimum of a cavity length scan. a) Large scan over 8 µm x 8 µm. b) Small 3D scan with higher resolution of a single GeV.

The lateral resolution of the 3D scan was given by the excitation mode volume, which was in contrast to the confocal setup where the lateral resolution was given by the collection volume. The spot size of the green excitation on the diamond membrane is given by:

$$\text{Spot size} = \frac{1.22\lambda_{ex}}{\text{NA}} \approx 1\mu\text{m} \tag{3.1}$$

where $\lambda_{ex} = 532nm$ is the excitation wavelength and NA is the numerical aperture of the objective. The collection volume for the cavity configuration was given by the cavity mode diameter, which is $\sim 3\mu$m.

### 3.5.5 Saturation measurements of the GeV center in the micro-cavity

To measure a saturation curve of a GeV center coupled to a cavity we scanned the cavity length while exciting the GeV center. For each excitation power the cavity length was scanned across three resonances. An example of such a measurement is shown in figure 3.16. The count rates of a resonance corresponds to the dark counts rates. The integration time for each point was typically 250 ms

The signal was a filtered convolution between the GeV emission and the cavity linewidth. The filtering was done with the tunable filters. Each mode was fitted

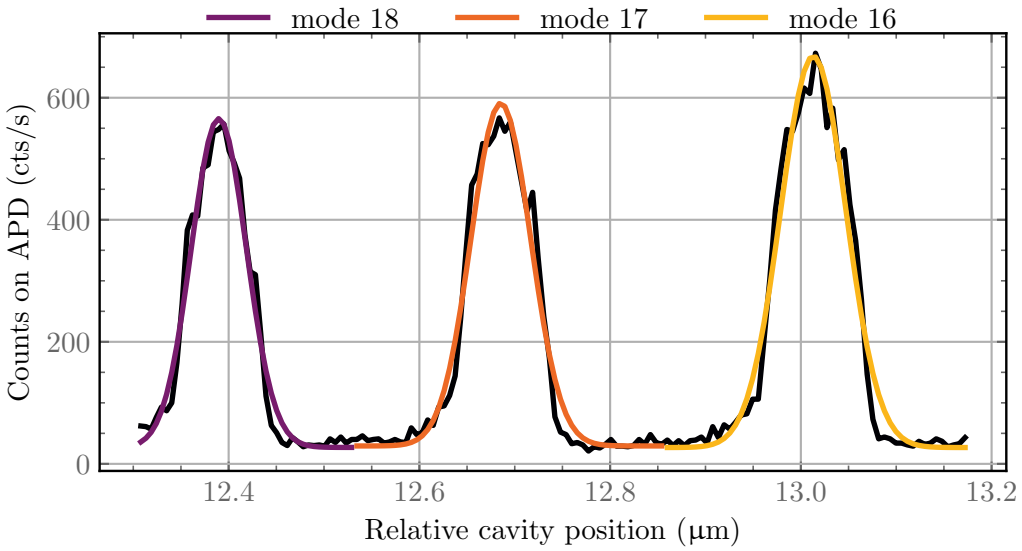


Figure 3.16: Saturation scan at 14 mW of 532 nm excitation.

with a Gaussian function, which is an approximation of the signal. The amplitude of the Gaussian function was used as the count rate for the GeV center at the given power.

# Chapter 4

# Cavity-funneled photon emission from a single GeV center in a diamond membrane

In this section we will describe the photon emission from a single GeV center. We studied the same GeV center in a free space experiment and when it was coupled to a fiber based micro-cavity. By comparing the emission in these two cases we found that photons were being funneled into the cavity mode and we were able to predict the Purcell enhancement factor at cryogenic temperature.

First, the mirrors that we used for our micro-cavity are characterized, which is followed by a characterisation of the diamond membrane containing the single GeV centers. A single GeV center in the diamond membrane was studied in a confocal microscope, which we refer to as the free space experiment. Afterwards, we investigate the properties of the cavity and the cavity mode. Finally, we study the same emitter inside the micro-cavity.

The emission from the GeV center is analyzed and compared between the confocal and the micro-cavity setup to show the observed funneling effect and measure the coupling efficiency to the cavity mode. From our results, we predict the expected Purcell enhancement factor for a similar experiment carried out at cryogenic temperature.

## 4.1 Mirror characterization

We used two dielectric mirrors in the micro-cavity, one concave fiber mirror and one flat macroscopic mirror. The fibers, that we used for our fiber mirror, were the 630HP fibers from Thorlabs. The fibers were ablated using the technique described in section 3.2. An interferometric image of the end-facet of the fiber mirror is shown in figure 4.1. This image is fitted with a parabolic fit and we found that the ROC was 38 μm.

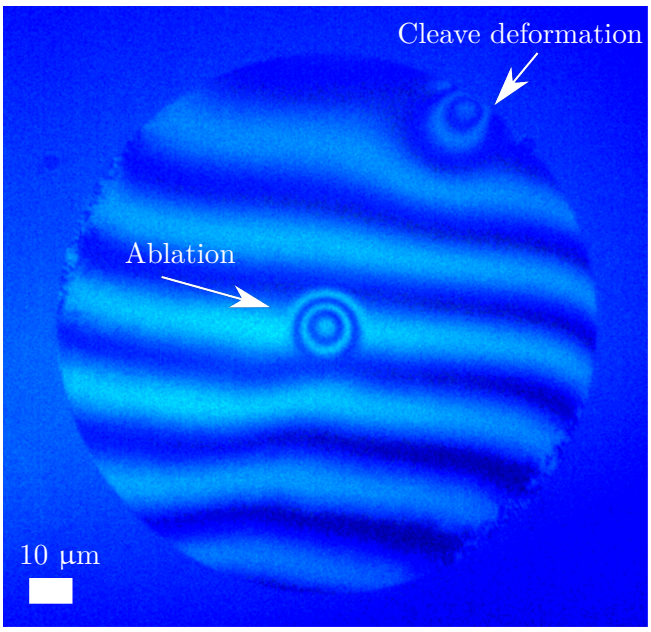


Figure 4.1: White light interferometric image of the fiber mirror. Rings in the center of the fiber shows the $CO_2$ ablation. The deformation of the fiber in the top right corner was from the cleaving process.

The other mirror in our cavity was a flat macroscopic mirror. The flat mirror was made on a 1/2-inch super-polished substrate from Coastline Optics [88]. The substrate was 2 mm thick and had an RMS roughness less than 0.1 nm ensuring low scattering losses.

The fiber and flat substrate were coated with DBR mirrors by Laseroptik [89]. The dielectric layer thicknesses of the DBR mirrors have been numerically optimized such that the two mirrors had the same transmission (70 ppm) for light with a wavelength of 602 nm. Using the transfer matrix method described in section 2.2.2 we calculated the transmissions for the fiber and the flat mirror, which is shown in figure 4.2. The transmission of the flat mirror was calculated with both diamond termination ($\text{flat}_d$) and air termination ($\text{flat}_a$), which corresponds to the bare cavity and the cavity with the diamond membrane configurations, respectively. The transmission of the fiber mirror was only calculated with air termination, because this mirror did not contain the diamond membrane. The coatings were matched, i.e. the flat and the fiber mirrors had the same transmission at the emission wavelength for the GeV center, which is 602 nm. The coating was also matched for 650 nm, which is useful when working with the NV center's PSB emission. Therefore, this coating can be used for both color centers, if needed. The matched coatings enabled collection of the emission, which could be done through both the flat and the fiber mirror.

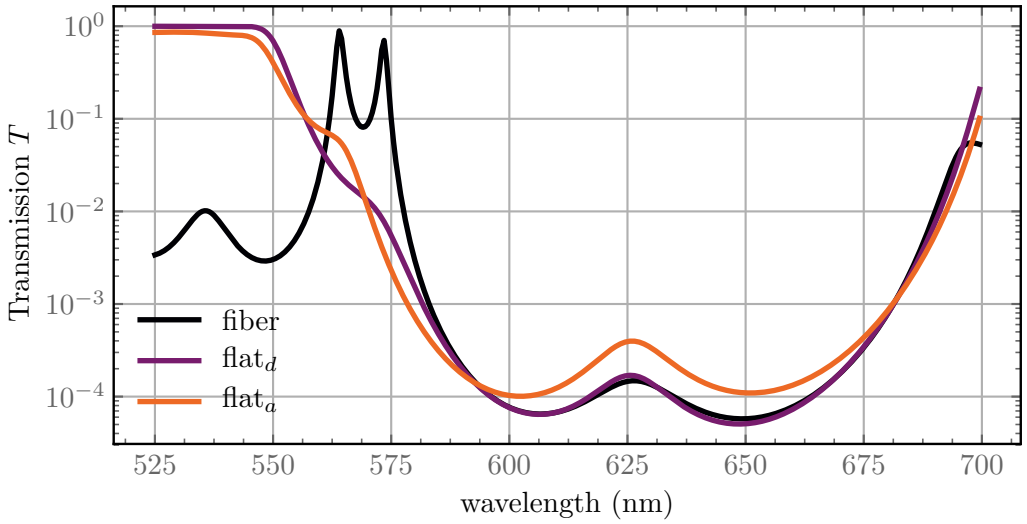


Figure 4.2: Calculated transmissions of the fiber and the flat mirror. The transmissions of the flat mirror are both shown with air termination flat$_a$, and diamond termination flat$_d$. The fiber mirror and the diamond terminated flat mirror are matched at the GeV emission wavelength, 602 nm, so the transmission is the same. The figure shows that the flat mirror is transmissive for the excitation wavelength 532 nm, while the fiber is reflective at the same wavelength to avoid fluorescence being generated in the fiber.

The mirror coatings had low absorption and scattering losses. However, for high finesse cavities these small losses become increasingly important. Here, we estimate the mirror losses from bare cavity finesse measurements at 637 nm, where the total losses $\mathcal{L}_{\text{tot}}$ of the cavity were determined:

$$\mathcal{L}_{\text{tot}} = \frac{2\pi}{F} \tag{4.1}$$

We introduce absorption loss in our simulation to match the measured $F$. Figure 4.3 shows the finesse of a cavity consisting of the fiber mirror and the flat mirror. Two cavity configurations are shown; one for the flat mirror being diamond terminated and one for the flat mirror being air terminated. Figure 4.3 also shows two cases for the total losses $\mathcal{L}_{\text{tot}}$ of the cavity; one where the total loss is only the transmission through the mirrors, $\mathcal{L}_{\text{tot}} = T$ and one where the total losses are the transmission through the mirrors and mirror losses, i.e. scattering and absorption losses $\mathcal{L}_{\text{tot}} = T + \mathcal{L}$. Importantly, when the diamond is introduced in the cavity it changes the power distribution inside the cavity. The power on each mirror varies depending on the diamond thickness. The effective finesse is therefore not necessarily the values on figure 4.3, which is assuming that the power on each mirror is the same.

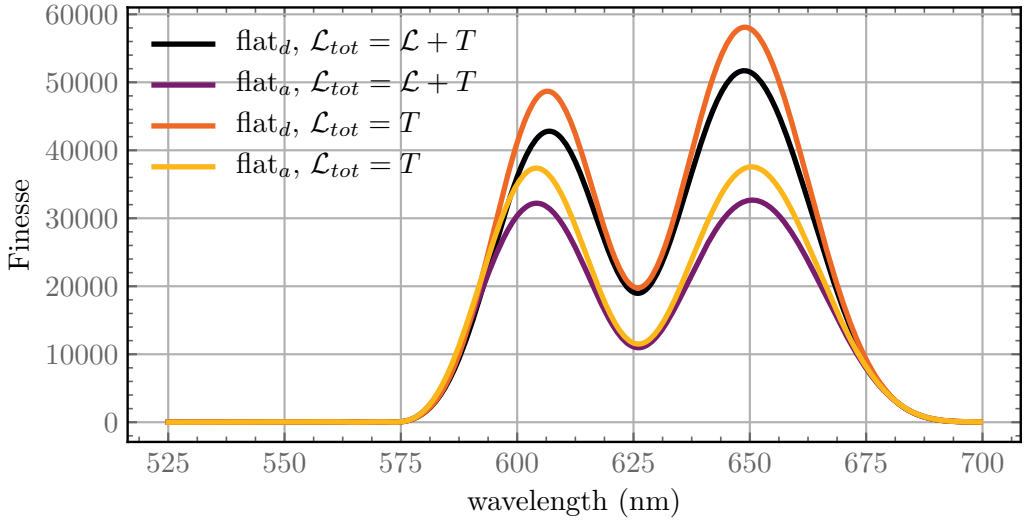


Figure 4.3: Calculated finesse for the fiber mirror and the flat mirror. For a bare cavity the flat mirror is air terminated, flat$_a$. When the diamond is present in the cavity the flat mirror is diamond terminated, flat$_d$. The total losses of the cavity, $\mathcal{L}_{\text{tot}}$, are either shown as only transmission $T$ or as transmission and mirror losses $T + \mathcal{L}$.

Further losses were also introduced from scattering losses at the surface of the diamond membrane, which is characterized in the following section.

## 4.2 Diamond membrane characterization

The diamond membrane on the flat mirror is shown in figure 4.4. From figure 4.4 it can be noticed that the surface of the membrane is very smooth, since it is completely transparent in some regions. Large parts of the membrane are bonded well to the mirror, which can be seen by the lack of interference patterns. The position of the GeV center, which we later investigate in detail, is marked by an arrow in figure 4.4. Furthermore, there are some unwanted small particles, which are thinly spread over the sample. These were most likely residuals from the water droplet. The dark contours reveal damage across the sample, which is most likely a results of graphitization during etching.

Using an AFM, the surface roughness was estimated to be 0.3 nm RMS. Confocal microscope measurements revealed a density of 0.6 GeV centers/$\mu$m$^2$, which means that we had a conversion efficiency of 6% of the Ge ion into GeV centers with this sample. The GeV center was studied in free space, which is the subject of the next section.

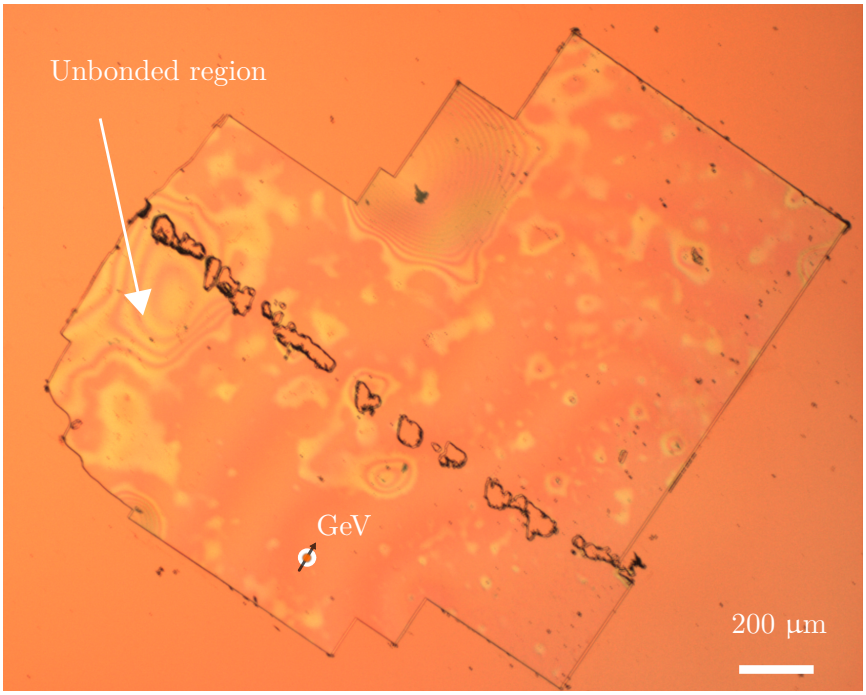


Figure 4.4: Diamond membrane bonded to the flat mirror imaged using an optical microscope. In some regions the diamond membrane is not bonded, which is seen by an interference pattern. The GeV center, which we studied in the following experiment, was in a well bonded region and is marked by an arrow on the image.

## 4.3 Single GeV centers in free space

We took confocal images of the diamond membrane to identify single GeV centers. Here, we show a full characterization of a single GeV center. These measurements were performed to ensure that we studied a single GeV center and as a reference to the micro-cavity measurements. In the confocal microscope we measured a saturation curve, lifetime, second order correlation function and spectrum from a single GeV center. These measurements are presented in the next section.

### Confocal microscope images

To study the GeV centers in free space we built a confocal microscope, see section 3.4. A confocal image of the diamond membrane is shown in figure 4.5. After bleaching the sample, i.e. scanning the sample several times at low speed with high excitation power (19 mW) of 532 nm light, bright GeV centers appeared. The bleaching was necessary due to surface contamination of the diamond membrane, which most likely occured during the water droplet transfer. The signal to noise ratio (SNR) was up to $\approx 12$ for the brightest GeV centers, however, the count rates were relatively low considering that the GeV centers have an excited state lifetime of $\approx 6$ ns. Our collection efficiency was low, which will be described in detail in section 4.6. Furthermore, the quantum efficiency is still an open question for GeV centers. For comparison, GeV centers in nano- and micro- crystalline diamonds the Qquantum efficiency was measured to $3 \pm 1\%$ and a measurement of a single GeV center in a nanophotonic waveguide yielded a lower bound of quantum efficiency $> 40\%$ [65].

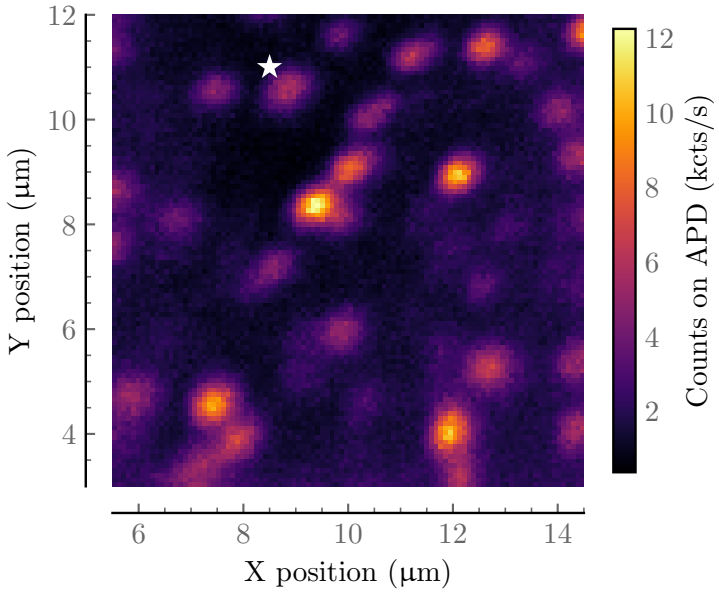


Figure 4.5: Confocal image of the diamond membrane with GeV centers at 19 mW of 532 nm excitation power. The emission signal was filtered in a narrow spectral band at around 600-605 nm. The white star marks the GeV center that we investigated in detail.

### Saturation measurements

We measured the saturation of the GeV centers to determine the emission count rate at infinite power, which we used to determine the efficiency of the photon emission into the cavity mode. Unfortunately, we were unable to saturate some of the emitters. However we found a single well isolated GeV center with good saturation behavior. This GeV center is marked with a white star in figure 4.5 and it is the GeV center which we studied in detail in the rest of this thesis.
The saturation measurement results for the GeV center are shown in figure 4.6 and fitted with the following saturation function:

$$I(P) = I^{\infty}\frac{P}{P + P_{sat}} + b_{bg}P + c_{dc}, \tag{4.2}$$

where $I^{\infty}$ is the count rate at infinite power, $P_{sat}$ is the saturation power, $P$ is the excitation power, $b_{bg}$ is the proportional factor for the background and $c_{dc}$ is the dark counts of the APD. The background measurement was fitted to a linear function:

$$I_{bg}(P) = b_{bg}P + c_{dc}, \tag{4.3}$$

where $I_{bg}$ is the emission count rate from the backgound.

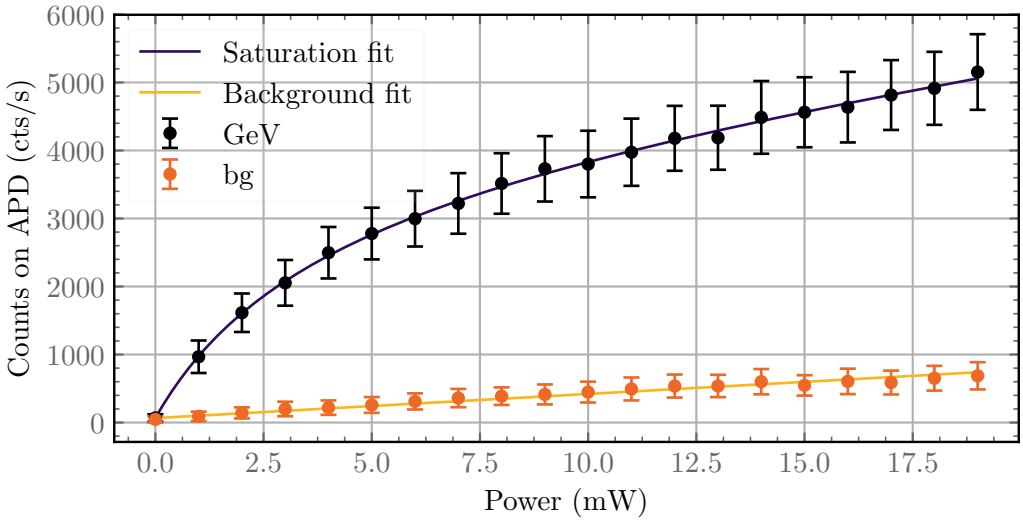


Figure 4.6: Saturation measurement for the GeV center and the background next to the GeV center. The mean and standard deviation of the emission count rate $I$ are shown. The measurement data was fitted with equation 4.2 and equation 4.3 for the GeV center and the background, respectively.

The fitting results are shown in table 4.1. The emission count rate $I^{\infty}$ at infinite power was found to be 4000 cts/s. We use this number to compare with the cavity count rate in order to show the cavity effect on the emission. Furthermore, we noticed that the dark counts for both the GeV center and the background were the same, as expected. The linear background term was twice as big for the GeV center as for the background, which can be attributed to local variations in background.

| | $I^{\infty}$ (cts/s) | $P_{sat}$ (mW) | $b_{bg}$ (cts/(s mW)) | $c_{dc}$ (cts/s) |
|---|---|---|---|---|
| GeV center | $4000 \pm 200$ | $3.9 \pm 0.3$ | $88 \pm 8$ | $67 \pm 6$ |
| Background | - | - | $36 \pm 1$ | $65 \pm 9$ |

Table 4.1: Fitting results of saturation curve for the GeV center and the background.

### Lifetime measurements

We measured the excited state lifetime of the GeV center. The resulting photon arrival histogram is shown in figure 4.7. The data was fitted to a single exponential function:

$$I = A\exp(-t/\tau) + C \tag{4.4}$$

which resulted in a lifetime $\tau = 6.0 \pm 0.1$ ns, as expected.

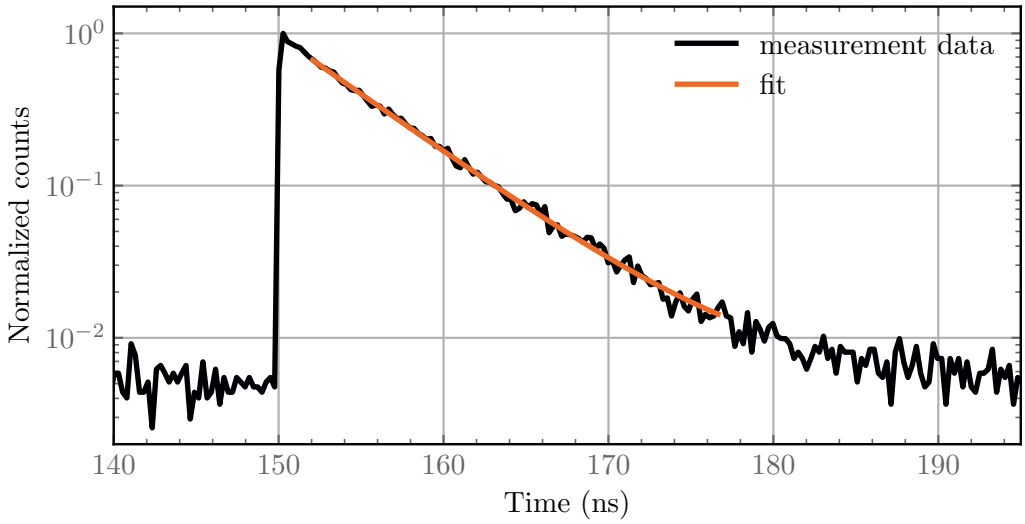


Figure 4.7: Lifetime measurement of the excited state of the GeV center.

### Second order correlation measurements

To show that we were interrogating a single GeV center we performed second order correlation measurements to show single photon emission. For this measurement, we used 19 mW of continuous wave (CW) 532 nm excitation light. Due to low count rates the measurement time was 60 minutes. The results are shown in figure 4.8. The results were fitted, including a Poissonian background [90], with the following three level model:

$$g^2(\tau) = \left(1 - (1+a)\cdot e^{-\frac{|\tau|}{\tau_1}} + a\cdot e^{-\frac{|\tau|}{\tau_2}}\right)\sigma^2 + 1 - \sigma^2 \tag{4.5}$$

where $\sigma = \frac{S}{S+B}$ is the ratio of the signal $S$ to the combined signal and background $B$. From the fitting we obtained $\tau_1 = 6.0 \pm 0.4$ ns, $\tau_2 = 1.19 \pm 0.010$ ms, $a = 2.2 \pm 0.4$, and $\sigma^2 = 0.75 \pm 0.16$. At zero delay $g^2(0) = 0.25 \pm 0.16$ there was clear antibunching, which demonstrates that we were studying a single GeV center. The curve was normalized to 1 in the long time limit, see figure 4.9. Furthermore, there was clear bunching, which showed that there was a third level with a lifetime of $\approx 1$ ms.

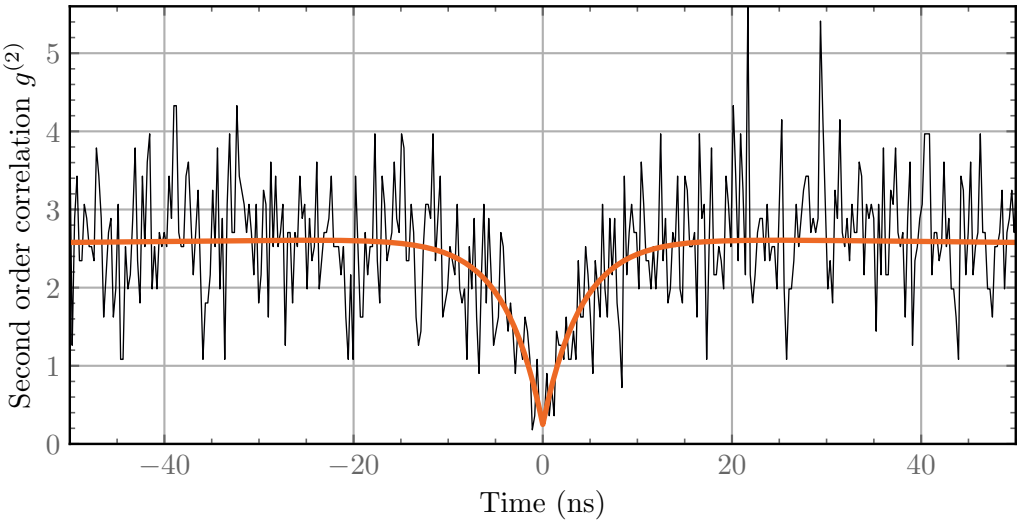


Figure 4.8: Second order correlation on a short time scale. Clear antibunching is seen, which is evidence of a quantum emitter. Since $g^{(2)}(0) < 0.5$ we can conclude that we are collecting light from a single GeV center.

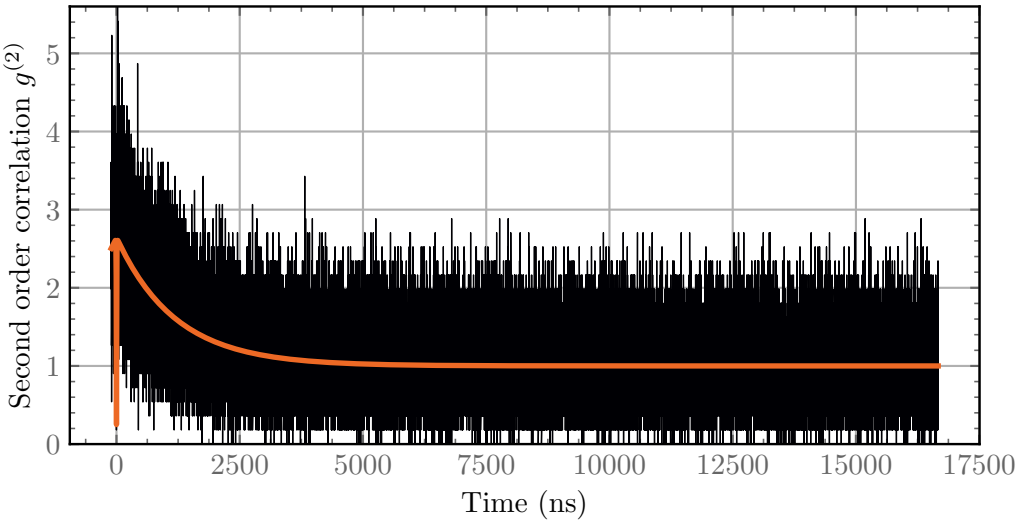


Figure 4.9: Second order correlation on a long time scale. Clear bunching is seen, which is evidence of a third level with a long lifetime.

### Spectral measurements

The spectral investigation was done with a spectrometer in order to investigate the linewidth of the ZPL and PSB. We measured the spectrum from the GeV center and from the background next to the GeV center. Each spectrum was measured for 5 x 300 seconds with 19 mW of excitation power going into the objective. The excitation power had local variations due to interference effects in the diamond membrane. To correct for power variations, we normalized the spectra from the GeV center and the background so that the integrated power in the diamond Raman peak was the same, see section 3.4.3. Then, the background was subtracted from the GeV signal to get the pure signal from the GeV center, which is shown in figure 4.10.

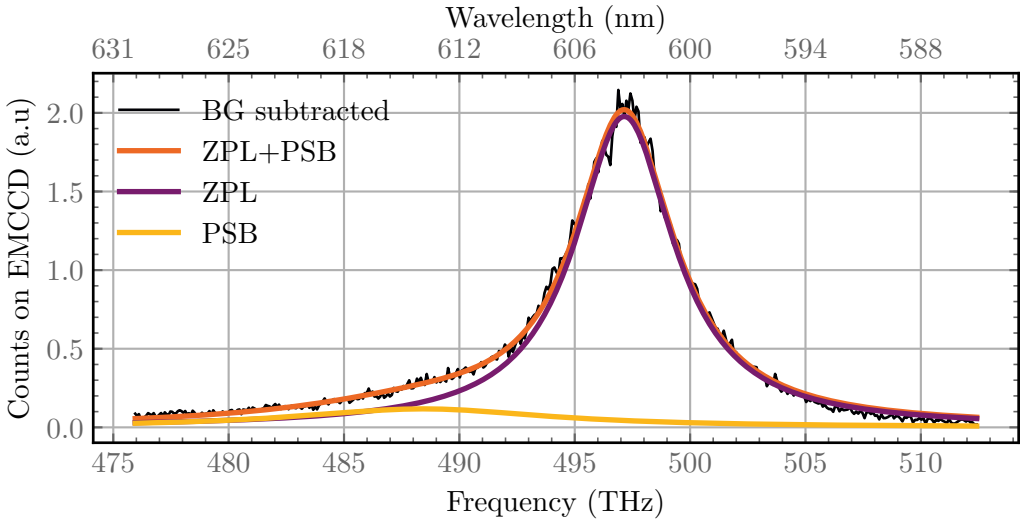


Figure 4.10: Spectrum from the GeV center in the confocal microscope. The background subtracted signal (BG subtracted) is shown and fitted with two Lorentzian functions for the zero phonon line (ZPL) transition and the phonon side band (PSB) transition.

To fit the data we used the sum of two Lorentzian functions, one for the ZPL and one for the PSB. Each Lorentizian function is given by:

$$I(\nu) = A\frac{(\gamma^*/4\pi)^2}{(\gamma^*/4\pi)^2 + (\nu - \nu_0)^2} \tag{4.6}$$

Where $I$ is the count rate as a function of frequency $\nu$, $A$ and $\frac{\gamma^*}{2\pi}$ is peak and the FWHM of the Lorentzian functions, respectively. $\nu_0$ is the central frequency of the transition. The PSB transition (centered around ~615 nm) corresponds to a local vibrational mode of the GeV center at 45.2 meV with respect to the ZPL [62]. The fitting results are shown in table 4.2.

The measured branching ratio $\varepsilon_m$, i.e. the relative intensity of each transition, was found to be 13% going into the PSB. This was lower than expected from the litterature. The Huang-Rhys factor for the GeV center is approximately 0.5 [63], which corresponds to a branching ratio of $A = 60\%$ into ZPL [62]. Therefore, we assume that part of the PSB occured at a higher wavelength and were not collected. To calculate how much of the PSB that was not collected we divided the emission into

| | ZPL | PSB |
|---|---|---|
| A (a.u.) | 1.98±0.01 | 0.118± 0.008 |
| $\gamma^*/2\pi$ (THz) | $5.21 \pm 0.05$ | $13.3 \pm 0.2$ |
| $\nu_0$ (THz) | 497.15±0.01 | $488.4 \pm 0.6$ |
| $\varepsilon_m$ (%) | 87 | 13 |

Table 4.2: Fitting parameters from confocal spectrum.

three branches: $A, B, C$. $A$ is the branching ratio into the ZPL and $B$ is the measured part of the $PSB$. The part of the PSB $C$ that was not collected was determined with the knowledge:

$$\frac{A}{A+B} = \varepsilon_{\text{ZPL}}, \qquad A + B + C = 1.0 \tag{4.7}$$

where $A$ is the branching ratio into the ZPL and $B$ is the collected part of the PSB and $\varepsilon_{\text{ZPL}} = 0.87$. Then $C$ can be determined by:

$$C = 1 - \left(1 + \frac{1 - \varepsilon_{\text{ZPL}}}{\varepsilon_{\text{ZPL}}}\right) A = 0.31 \tag{4.8}$$

Therefore, we conclude that 31 % of the phonon side band was not collected since it occurred at a higher wavelength.

This measurement finalized our characterization of the GeV center in free space. In the following section we will first characterize the micro-cavity with the diamond membrane inside and then the single GeV center that was coupling to the cavity mode.

## 4.4 Micro-cavity with a diamond membrane

This section describes how we found the same GeV center inside the micro-cavity as we studied in the confocal setup. We studied the cavity modes to obtain the diamond thickness and the cavity length. A measurement of the finesse in length was performed to obtain the cavity linewidth in frequency before we moved on to study a single GeV center.

#### 3D cavity scan

We identified the same GeV center in the cavity setup, as we studied in free space, by comparing a 3D cavity scan image with a confocal image. The 3D scan image is shown in figure 4.11.

There was a clear correlation between our confocal scans and the 3D scans, and we were able to locate the same isolated emitter as we characterized in our free space configuration. To clearly show this correlation, we overlaid the contour plot of the confocal image on the 3D scan in figure 4.12. It is seen that some of the GeV centers do not couple to the cavity, which can be explained by the GeV center sitting in a node of the cavity field. However, there were strong spatial correlation and we therefore conclude that we studied the same GeV center as in the confocal microscope.

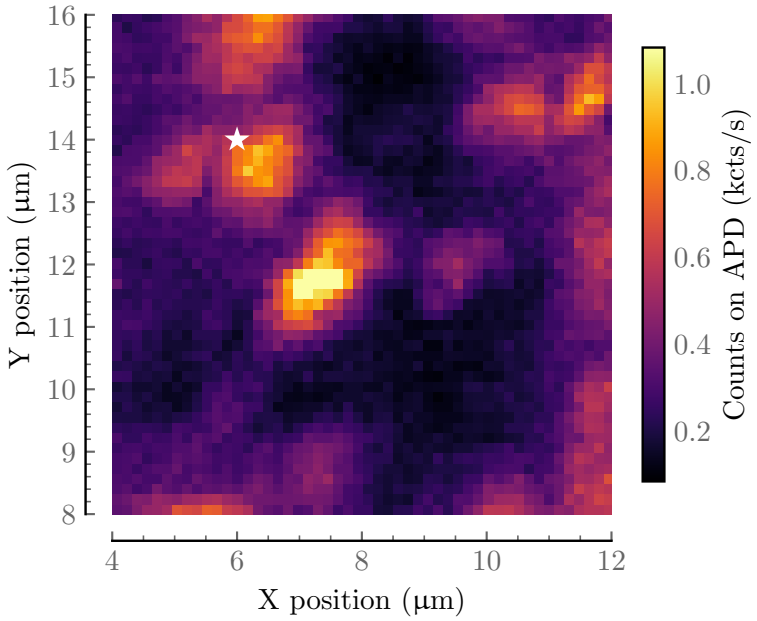


Figure 4.11: 3D cavity scan of the diamond membrane at 19 mW of 532 nm excitation power. The bright spots are GeV centers. The studied GeV center is marked with a white star on the plot.

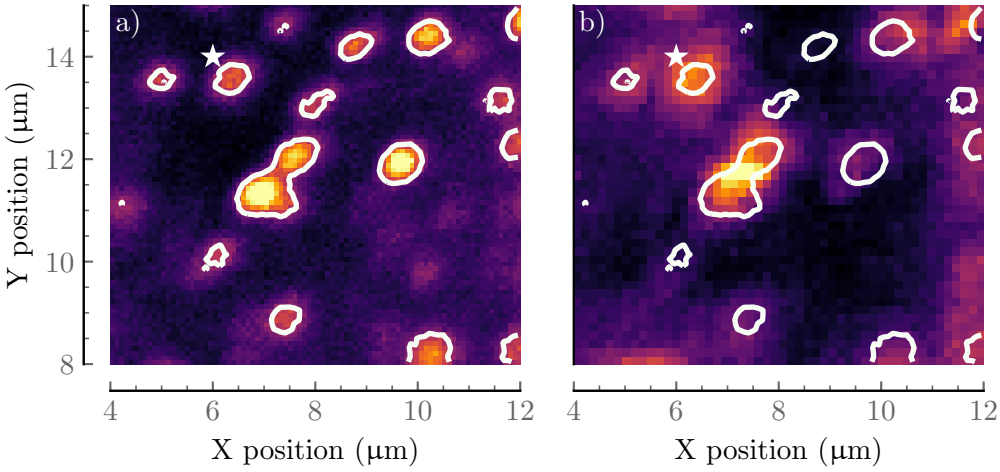


Figure 4.12: a) Confocal image of the diamond membrane with contour lines (4 kcts/s) around the GeV center. b) 3D scan image of the diamond membrane with the contour lines from the confocal image to show spatial correlation.

### White light measurements

We studied the cavity modes by scanning the fiber while sending white light through the cavity, see figure 4.13. Due to the diamond membrane the cavity modes have a wave pattern. The fundamental cavity modes are extracted from the measurement and then fitted to our 1D transfer matrix model, see section 2.2.2. From the fit the mode number, cavity length and diamond thickness were determined. We found the diamond thickness to be 860.4 ±0.4 nm and the shortest mode cavity number $m$ to be 16. A shorter cavity would cause the fiber mirror to touch the diamond membrane on flat mirror.

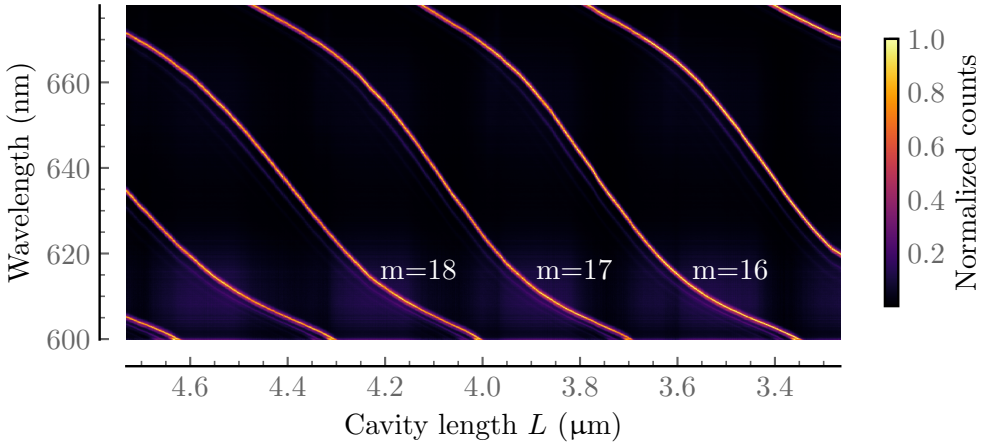


Figure 4.13: White light measurement of the cavity with the diamond membrane inside. The pzt position is read with a stain gauge. The higher the position the shorter the cavity.

### Finesse measurements

We measured the finesse $F$ in length of the cavity at the position of the studied GeV center. This was done by sending 602.5 nm light through the cavity while scanning the cavity length. The transmission of the cavity was measured by a photodetector and the result is shown in figure 4.14. The linewidth in length was determined by fitting the resonances with Lorentzian functions. The finesse, $F$ could then be determined by:

$$F_L = \frac{L_{\text{fsr}}}{\Delta L}, \tag{4.9}$$

where $L_{\text{fsr}}$ is the free spectral range in length and $\Delta L$ is the linewidth in length. From this measurement we found $F_L = 11000 \pm 2000$ based on the four cavity resonances with cavity linewidths of $\Delta L = 28 \pm 4$ pm. The linewidth may vary slightly with mode number size, since the transverse mode size changes, but we found this to be less than the uncertainty in the measurement. By using the magnitude of the resonance slope for mode $m = 16$ around 603 nm the linewidth in frequency can be determined:

$$\Delta\nu = \left|\frac{\mathrm{d}v}{\mathrm{d}L}\right| \Delta L = 1.1 \pm 0.2 \text{ GHz}, \tag{4.10}$$

where we have determined the magnitude of the slope to be $40 \pm 2$ THz/μm from the white light measurement.

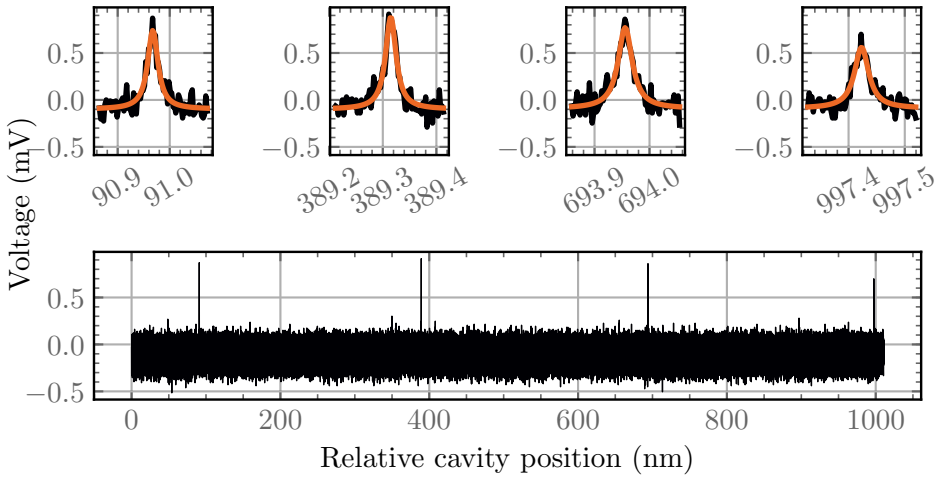


Figure 4.14: Linewidth measurement of the cavity. The cavity length was scanned across four resonances and the linewidth of each resonance was fitted with a Lorentzian function.

## 4.5 GeV center coupled to a cavity mode

The measurements in this section were done with a single GeV center inside the cavity. First we looked at the spectrum from the GeV center inside the micro-cavity. We then measured the emission rates from the GeV center coupled to the cavity.

### Spectral measurements

Beside the spatial correlation, we further confirmed that the emission signal collected from the cavity was actually from a single GeV center by measuring the spectrum from the cavity. The diamond membrane was illuminated with 19 mW of 532 nm light and the cavity length was scanned while measuring the spectrum. The result is shown in figure 4.15b. We used an optical bandpass filter for $605 \pm 15$ nm, which did not filter the spectrum shown in these plots. The clear window around the resonance indicates an integration window of 30 nm, which was used for figure 4.15a. Figure 4.15a shows the position integration counts for each wavelength. The raw integrated signal has oscillations due to noise on the detector and due to instability in the cavity length. A low count rate means that the integration for each cavity length position was 10 seconds. Thermal drifts and mechanical instability led to the cavity length not being scanned linearly. This is seen in the figure around 597 and 609 nm, where the cavity was moved back. Furthermore, there was a broken pixel near 610 nm, which has been removed from plot 4.15a. The orange line shows the smoothed integrated counts. This smoothed signal has the shape of the spectrum from a GeV center.

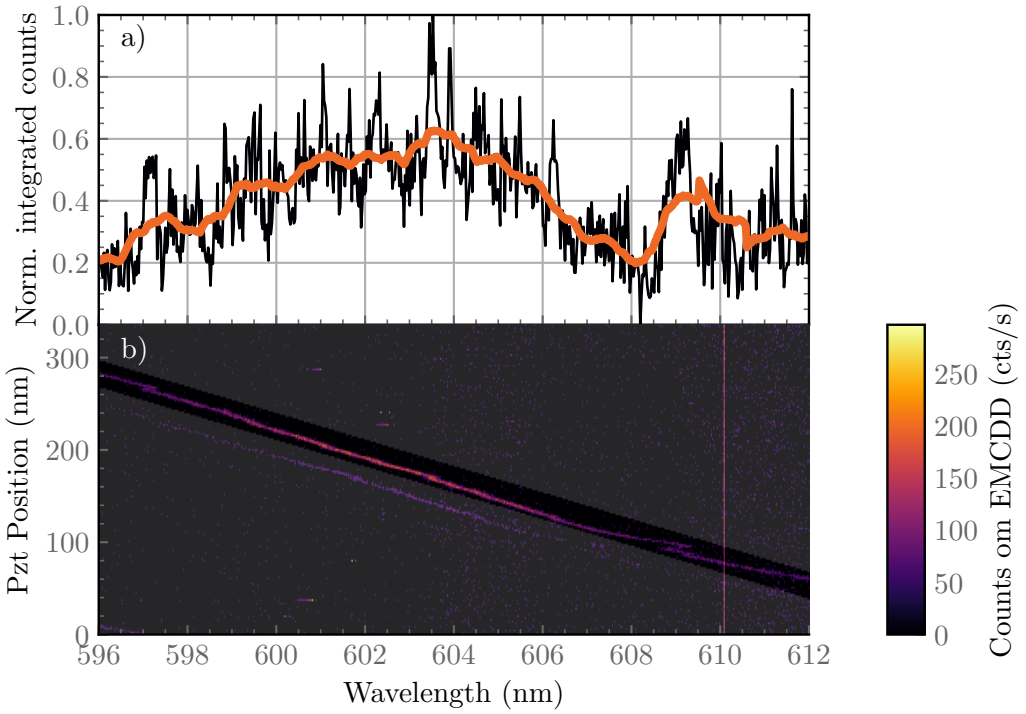


Figure 4.15: Spectrum from a GeV center coupled to the cavity. 19 mW green excitation was used while the cavity length was scanned. a) Integrated spectrum of data (clear window) around the resonances. The orange line shows the smoothed raw data. b) Thermal drift and mechanical instability led to non-linear scanning of the cavity length, which is clearly seen around 597 and 609 nm. Further, cosmic rays and common noise have been removed.

### Saturation measurements

A saturation measurement in the cavity was done for three longitudinal cavity modes. The mode numbers were first determined by measuring and fitting the white light scan shown in figure 4.13. Afterwards, the count rates for 20 different excitation powers of 532 nm were measured on the GeV center and on the background near the GeV center. The emission light was filtered with two tunable filters, which gave a spectral window in the range of 600-605 nm. A saturation behaviour was observed for the GeV center, see figure 4.16. The data was fitted with the function given in equation 4.2 without the dark count term. The dark count was not included in the fit, since the dark count corresponds to the baseline of the Gaussian fit, see section 3.5.5. The background was fitted to the function in equation 4.3 also without the dark count term.

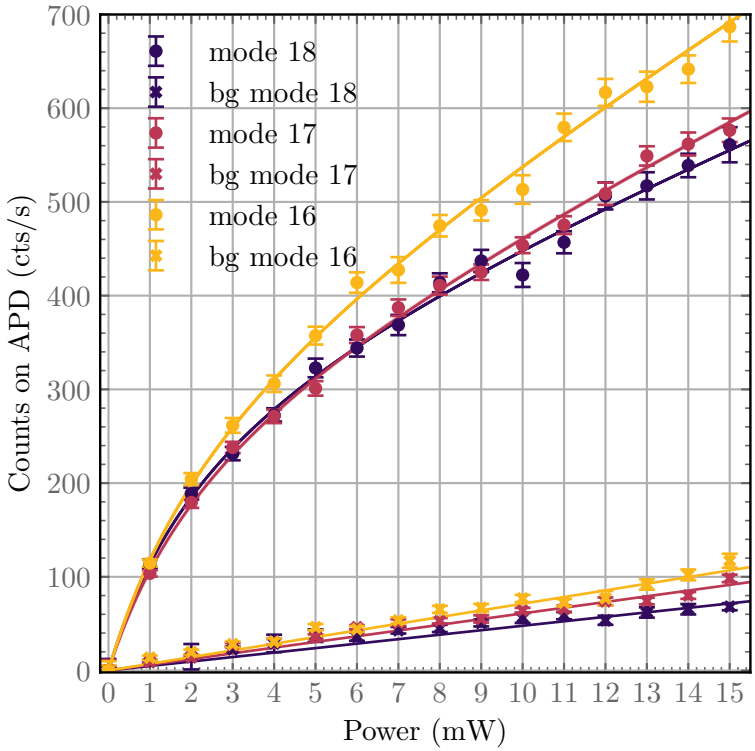


Figure 4.16: Saturation for the GeV center and for the background near the GeV center were measured for three modes.

The fitting results are shown in table 4.3. The count rates at infinite excitation power, $I^{\infty}$, were similar for all modes within one standard deviation. The background counts increased with decreasing mode number. This can be explained by the cavity linewidth in frequency, which increased with shorter cavity lengths.

| | $I^{\infty}$ (cts/s) | $P_{sat}$ (mW) | $b_{bg}$ (cts/(s mW)) |
|---|---|---|---|
| GeV center | | | |
| mode 16 | $350 \pm 30$ | $2.8 \pm 0.4$ | $27 \pm 2$ |
| mode 17 | $320 \pm 30$ | $2.7 \pm 0.4$ | $21 \pm 1$ |
| mode 18 | $340 \pm 30$ | $2.6 \pm 0.4$ | $18 \pm 2$ |
| Background | | | |
| mode 16 | - | - | $7.1 \pm 0.2$ |
| mode 17 | - | - | $6.1 \pm 0.1$ |
| mode 18 | - | - | $4.8 \pm 0.2$ |

Table 4.3: Fitting results of the saturation curve for the GeV center and the background in the cavity.

## 4.6 Comparison of GeV emission in and out of the micro-cavity

In this section we will determine the coupling efficiency $\beta$ from the GeV center to the micro-cavity mode and then we will determine the spectral enhancement of the GeV center in the cavity compared to when the GeV center is out of the cavity..

### 4.6.1 $\beta$-factor

The $\beta$-factor and the peak spectral density characterize the coupling of the GeV center to the micro-cavity at room temperature. The experimentally determined efficiency of the emission into the cavity mode $\beta_{\text{exp}}$ was measured to [23, 35]:

$$\beta_{\text{exp}} = \frac{I^{\infty}_{\text{cav}}}{I^{\infty}_{\text{free}}} = 0.22 \pm 0.09\% \tag{4.11}$$

where $I^{\infty}_{\text{cav}}$ is the intensity into the cavity mode at infinite excitation power and $I^{\infty}_{\text{free}}$ is the emission count rate into all modes at infinite excitation power when the GeV center is in free space. The measured $\beta_{\text{exp}}$ will be compared to a simulated $\beta_{\text{sim}}$ in section 4.6. We corrected our measured emission count rates for collection efficiency to the total count rates from the GeV center:

$$I^{\infty}_{\text{cav}} = \frac{I^{\infty}_{m,\text{cav}}}{\eta_{\text{cav}}\eta_{\text{com}}} = 4.4 \pm 0.9 \text{ kcts/s} \tag{4.12}$$

where $I^{\infty}_{m,\text{cav}}$ is the measured saturating count rate. In free space we also correct the count rate with the collection efficiency:

$$I^{\infty}_{\text{free}} = \frac{I^{\infty}_{m,\text{free}}}{\eta_{\text{con}}\eta_{\text{com}}} = 2.0 \pm 0.7 \text{ Mcts/s} \tag{4.13}$$

The efficiencies were determined to be $\eta_{\text{con}} = 0.006 \pm 0.002$, $\eta_{\text{cav}} = 0.26 \pm 0.04$ and $\eta_{\text{com}} = 0.33 \pm 0.02$, see section 4.6.3. This $I^{\infty}_{\text{free}}$ is low for an emitter with a 6 ns lifetime. The expected count rate for a two level system is up to 170 Mcts/s. If we assume a quantum efficiency of 3%, we should measure $I^{\infty}_{\text{free}} = 5.3$ Mcts/s, which is not the case. From the $g^{(2)}$ measurement we know that there is a third level that limiting the emission rate. Other limiting effects could be blinking, which has been observed at low temperature [17] and charge state switching to a neutral GeV center has also been suggested [91].

### 4.6.2 Spectral density of the GeV center emission

At room temperature cavity funneling can be observed as a sign of coupling between the micro-cavity and the GeV center [31, 75, 76, 92, 93]. Therefore, we calculated the peak spectral density (PSD) to show this effect. The PSD of the GeV center in the confocal and in the cavity experiment were measured and compared. We corrected the measured count rates with the collection efficiency.

First, the peak spectral density was defined as:

$$\text{PSD} = \max_{\nu \in [\nu_1, \nu_2]} \{\text{SD}(\nu)\} \tag{4.14}$$

where $\nu_1, \nu_2$ is the edges of the emission frequencies. The spectral density $\mathrm{SD}(\nu)$ is related to the saturated count rate $I^\infty$ by:

$$I^\infty = \int_{\nu_1}^{\nu_2} \mathrm{SD}(\nu)\mathrm{d}\nu \tag{4.15}$$

We did not measure the SD directly but we know the spectral shape $\sigma(\nu)$, which we can get from the spectrum measurement, see figure 4.15, for the confocal setup and from the linewidth $\Delta\nu$ for the cavity experiment. The spectral shape is related to the SD by:

$$\sigma(\nu) = \frac{\mathrm{SD}(\nu)}{I^\infty} \tag{4.16}$$

where:

$$\int_{\nu_1}^{\nu_2} \sigma(\nu)\mathrm{d}\nu = 1 \tag{4.17}$$

therefore, the PSD can now be calculated:

$$\mathrm{PSD} = \max_{\nu\in[\nu_1,\nu_2]}\{\sigma(\nu)\}I^\infty \tag{4.18}$$

Now, we start by calculating the PSD of the emission from the GeV center in the cavity using the expression above. For the cavity experiment the spectral shape is a Lorentzian function. The maximum of a normalized Lorentzian function is:

$$\max_{\nu\in[\nu_1,\nu_2]}\{\sigma(\nu)\} = \frac{2}{\pi\Delta\nu} \tag{4.19}$$

From equation 4.12 we know the corrected saturated count rate, and the linewidth was determined to $1.1 \pm 0.2$ GHz, see equation 4.10. With this we can calculate the PSD for the GeV emission in the cavity:

$$\mathrm{PSD}_{\mathrm{cav}} = \frac{2I^\infty_{\mathrm{cav}}}{\pi\Delta\nu} = 2500 \pm 700 \text{ cts/(s GHz)} \tag{4.20}$$

This PSD can now be compared to the PSD of the emission from the GeV center when it is in free space.

We start by correcting the saturated count rate by the collection efficiency:

$$I^\infty_{\mathrm{con,corr}} = \frac{I^\infty_{m,\mathrm{free}}}{\eta_{\mathrm{con}}\eta_{\mathrm{com}}} = 550 \pm 200 \text{ kcts/s} \tag{4.21}$$

we used $\eta_{\mathrm{con}} = 0.018 \pm 0.008$ without the spectral filtering correction, see section 4.6.3. From the spectral measurement in figure 4.10 the spectral shape can be determined. In our saturation measurement the emission was filtered by the tunable filters from ∼600-605 nm. With this we can calculate the SD which is shown in figure 4.17. With this we get:

$$\max_{\nu\in[\nu_1,\nu_2]}\{\sigma(\nu)\} = 0.283 \text{ THz}^{-1} \tag{4.22}$$

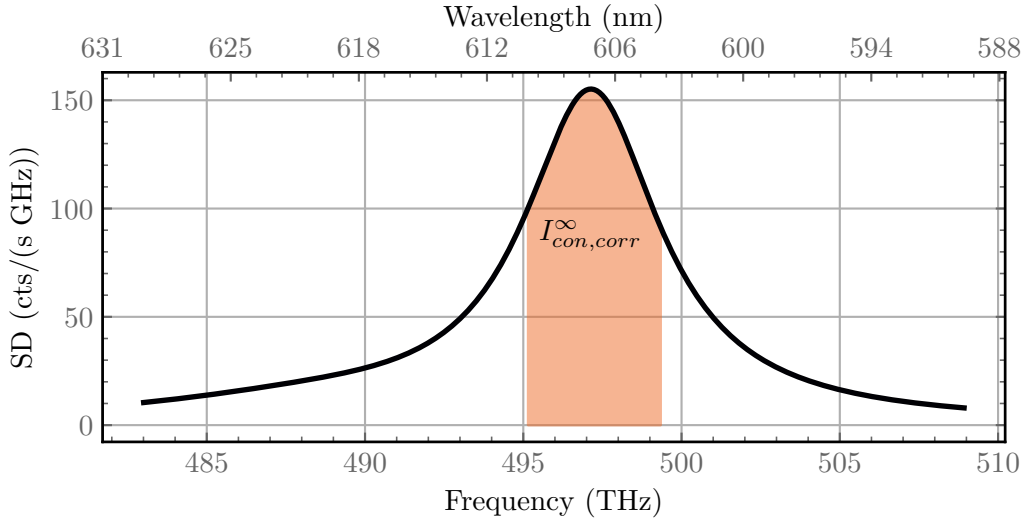


Figure 4.17: Spectral density (SD) from the GeV center in the confocal setup. The shape of the emission was measured with a spectrometer, see figure 4.6. The emission in our saturation measurement was filtered by tunable filters (∼600-605 nm), which is shown by the orange region. The area of the orange region under the SD curve corresponds to $I^{\infty}_{\mathrm{con,corr}}$.

The PSD for the GeV center emission in free space can be determined:

$$\mathrm{PSD}_{\mathrm{con}} = 155 \pm 50 \text{ cts/(s GHz)} \tag{4.23}$$

This shows that we measured a spectral enhancement of $16 \pm 7$ for the GeV center when it was in the cavity compared to when in was in free space. This spectral enhancment was expected for a GeV center coupled to a micro-cavity at room temperature.

### 4.6.3 Collection efficiencies

We corrected the count rates from the GeV center by the collection efficiencies in both the cavity and in the confocal setup. The cavity and confocal setup share parts of the same detection path which will be referred to as the common path.

In the confocal setup we modelled the GeV center as a dipole emitter, which was described in section 2.4. We found that around $7 \pm 2\%$ of the light was emitted into the objective, where the uncertainty was found using the straggle of the implantation depth. The implantation depth was $125 \pm 20$ nm. The transmission of the objective, at the wavelength of 600 nm, was $0.80 \pm 0.01$, which was estimated from the transmission curve given by the manufacturer. Two mirrors guided the collected light into the common path and we estimated the transmission from the manufacturer's specifications.

We estimated the fiber coupling in our detection path, i.e. the overlap between the collimated dipole emission from back side of the 0.7 NA objective and the Gaussian mode in the SM detection fiber. This was done by studying the difference in GeV

center count rates when using an SM and an MM fiber in the detection path. We assume that we fiber coupling efficiency was 1 with the MM mode fiber. We found that when using the SM fiber the GeV emission rates were $0.40 \pm 0.07$ of the emission rates compared to using the MM fiber. Here, we accounted for difference in background as a result of the larger collection volume with the MM fiber. We are currently working on 3D dipole simulations to confirm that the dipole emission pattern can explain our estimated fiber coupling efficiency.

The spectral filtering by the two tunable filters was determined by measuring a flat background signal from the membrane with the spectrometer while exciting with 532 nm light. We then fitted the spectral window and found the edges of the window to be 600.36 ±0.4 nm and 605.54 ±0.4 nm. Using the spectral window on the spectrum measured in figure 4.10, we found that 27% of the emission was collected. This gave a total collection efficiency of $\eta_{\text{con}} = 0.9\%$ for the confocal path. An overview of the efficiencies $\eta$, with uncertainties $\delta\eta$, is shown in table 4.4.

| optical element | $\eta$ | $\delta\eta$ |
|---|---|---|
| dipole emission | 0.07 | 0.02 |
| objective transmission | 0.80 | 0.01 |
| SM fiber coupling | 0.40 | 0.07 |
| mirrors | 0.98 | 0.01 |
| total w/o spectral filtering | 0.022 | 0.007 |
| spectral filtering | 0.27 | 0.00 |
| total w spectral filtering | 0.006 | 0.002 |

Table 4.4: Collection efficiency $\eta$ for confocal detection path with uncertainties $\delta\eta$ for the confocal path.

For the common path the collection efficiencies are given in table 4.5. All the common efficiencies are taken from the manufacturer's data. In the common path the efficiency was found to be $\eta_{\text{com}} = 33 \pm 1\%$.

| optical element | $\eta$ | $\delta\eta$ |
|---|---|---|
| short pass filter | 0.92 | 0.02 |
| long pass filter | 0.92 | 0.02 |
| 532 notch filter | 0.97 | 0.02 |
| fiber lens | 1.0 | 0.01 |
| fiber facets | 0.94 | 0.01 |
| APD telescope | 0.98 | 0.01 |
| APD efficiency | 0.45 | 0.00 |
| total | 0.33 | 0.01 |

Table 4.5: Collection efficiency, $\eta$ with uncertainties $\delta\eta$ for the detection common path.

For collection efficiencies in the cavity setup, we first calculated the escape efficiency through the flat mirror by using the transfer matrix model, described in section 2.2.2, including all scattering, absorption and transmission losses. We found that 0.29 ±

0.03 of the cavity losses escape through the flat mirror. The escape efficiency depends on the mode type. Since we are in the diamond mode, a relative large fraction of the losses occur on the flat mirror.

The fiber coupling was calculated as the overlap between two gaussian beams. We measured the beam radius of the fundamental mode after the collection objective where the beam was collimated. We sent 602.5 nm laser through the fiber mirror and scanned the cavity and then measured the transverse intensity profile with a CCD camera. We found the beam radius to be 686±6µm. This beam was focused down into the fiber with an achromatic lens with f=10 mm, which resulted in a focus diameter size of $5.6 \pm 0.6$µm. The collection fiber had a mode field diameter of $4.0 \pm 0.5$µm. The mode overlap is then given by [29]:

$$\varepsilon = \frac{4\omega_1^2\omega_2^2}{\left(\omega_1^2 + \omega_2^2\right)^2} = 0.89 \pm 0.09 \tag{4.24}$$

where $\omega_i$ is the Gaussian beam radii.

We also collected some light from high order cavity modes, which we were not interested in since they don't share the same spatial mode and frequency as light from the fundamental mode. This light was collected due to misalignment and non perfect lenses, which lead to a non zero overlap of higher order cavity and the collection fiber. This effect can be seen from the spectrum, see figure 4.18. By integrating the fundamental and first order modes, we found that 80% of the light was coming from the fundamental mode and 20% was in the first order mode. We therefore corrected our count rates with the factor 1.25, since we were over counting. The rest of the cavity collection efficiencies was determined from the manufacturer's specification.

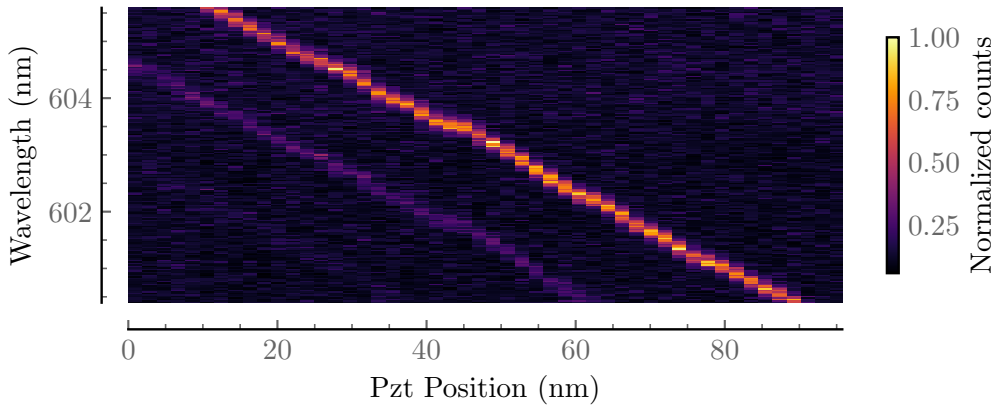


Figure 4.18: Unwanted light from higher order cavity modes were also collected. The bright resonance is the fundamental Gaussian mode and the purple resonance is the first higher order transverse mode. This measurement was taken with 532 nm excitation and the cavity length was scanned across the GeV spectrum.

The total efficiency for the cavity setup was found to $\eta_{\text{cav}} = 0.26 \pm 0.04$ and all the efficiencies are shown in 4.6

| optical element | $\eta$ | $\delta\eta$ |
|---|---|---|
| out coupling throgh flat | 0.29 | 0.03 |
| objective trans. | 0.91 | 0.01 |
| mirrors | 0.96 | 0.02 |
| dichroic mirror | 0.93 | 0.00 |
| fiber coupling | 0.89 | 0.09 |
| Higher order modes | 1.25 | 0.08 |
| total | 0.26 | 0.04 |

Table 4.6: Collection efficiency, $\eta$, with uncertainties $\delta\eta$ for the cavity detection path.

## 4.7 Simulations of $\beta$ and $F_p$

We compared the measured $\beta_{\text{exp}}$ with simulations. From the theory section 2.3.1 we found that the coupling efficiency into the cavity mode can be calculated by:

$$\beta_{\text{sim}} = \frac{R_{PSB} + R_{\text{ZPL}}}{\gamma_r + R_{PSB} + R_{\text{ZPL}}}, \tag{4.25}$$

where $R_{PSB}$ and $R_{\text{ZPL}}$ are the incoherent coupling rate to the cavity mode from the PSB and ZPL, respectively. We only consider the radiative part of the excited state decay rate, since this is the only part which couples to the cavity mode. We split the total excited state decay rate $\gamma$ into a radiative part $\gamma_r$ and a non-radiative part $\gamma_{nr}$. The quantum efficiency is defined as $\epsilon_{\text{QE}} = \frac{\gamma_r}{\gamma}$. We have used $\gamma = 1/\tau = 2\pi \times 26.5$ MHz, where $\tau$ is the measured excited state lifetime of 6.0 ns. We used $\epsilon_{\text{QE}} = 0.03$ [94], which yielded $y_r = 2\pi \times 0.8$ MHz.

The incoherent cavity coupling rates $R_i$ for PSB and ZPL are given by:

$$R_i = \frac{4g_i^2}{\kappa + \gamma_r + \gamma_i^\star} \frac{1}{1 + \left(\frac{2\delta_i}{\kappa+\gamma_r+\gamma_i^\star}\right)^2}, \tag{4.26}$$

where $g_i = \sqrt{\varepsilon_i} g$ and $\delta_i$ is the detuning of the transition $i$ to the cavity resonance. $\varepsilon_i$ is the branching ratio of the $i$ transition. For the studied GeV center we found that $\varepsilon_{\text{ZPL}} = 0.6$ and $\varepsilon_{\text{PSB}} = 0.09$. The rest of the PSB was assumed to occur at a higher wavelength and can be neglected. When the cavity is on resonance with the ZPL the contribution from the PSB is small:

$$\frac{R_{\text{ZPL}}}{R_{\text{PSB}}} = \frac{\varepsilon_{\text{ZPL}}\gamma^\star_{\text{PSB}}}{\varepsilon_{\text{PSB}}\gamma^\star_{\text{ZPL}}} \left(1 + \left(\frac{2\delta_{\text{PSB}}}{\kappa + \gamma_r + \gamma^\star_{\text{PSB}}}\right)^2\right) \approx 50 \tag{4.27}$$

We therefore neglected the contribution from the PSB:

$$\beta_{\text{sim}} = \frac{R_{\text{ZPL}}}{R_{\text{ZPL}} + \gamma_r} \tag{4.28}$$

$R_{\text{ZPL}}$ was determined from the mode volume. The vaccum electric field in the cavity has been normalized using [74]:

$$\frac{\hbar\omega}{2} = \frac{\pi W_0^2}{2} \int_{\text{cav}} \epsilon_0 n(z)^2 |E_{\text{vac}}(z)|^2 \mathrm{d}z, \tag{4.29}$$

since the vacuum state has the energy $\frac{\hbar\omega}{2}$. From the electric field distribution the effective length of the cavity was calculated using equation 2.32. For the diamond thickness of 860 nm, we found that we had an almost fully diamond-like cavity mode, which can be seen in figure 4.19. We found $L_{\text{eff}} = 1.75$ µm. The cavity beam waist was calculated using the ABCD matrix for Gaussian beams with a ROC = 38 µm of the fiber mirror. We found the cavity beam waist to be $W_0 = 1.53$µm. The mode volume was then determined to be $V = 2.7\mu\text{m}^3 \approx 170\frac{\lambda^3}{n_d^3}$. A list of all the cavity parameters is given in table 4.7. The coupling strength can then be determined:

$$g_{\text{ZPL}} = \sqrt{\epsilon_{\text{ZPL}}}\sqrt{\frac{3c\lambda^2\gamma_r}{8\pi n_d^3 V}} = 2\pi \times 162 \text{ MHz} \tag{4.30}$$

| $W_0$ | $L_{\text{eff}}$ | $V$ | $Q$ | $t_d$ | $t_a$ |
|---|---|---|---|---|---|
| 1.39 µm | 1.75 µm | 2.7 µm$^3$ | 452,000 | 0.860 µm | 2.54 µm |

Table 4.7: Cavity parameters for the GeV center in our cavity.

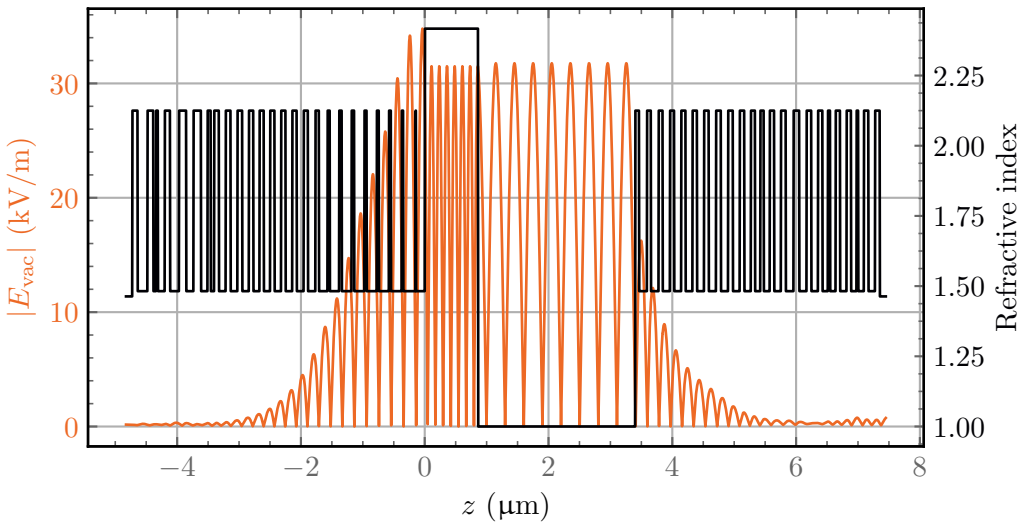


Figure 4.19: Calculated electric field distribution inside the cavity. For the diamond thickness of 860 nm the cavity is close to diamond-like.

Now we can calculate the exchange rate $R_{\text{ZPL}} = 2\pi \times 20.3$ kHz. See table 4.8 for all the rates. With this, we finally can calculate the efficiency into the cavity mode:

$$\beta_{\text{sim}} = 2.5\% \tag{4.31}$$

where we assumed a maximum angular and spatial overlap with the cavity mode, i.e $\xi = 1$. This result should be compared to the measured value $\beta_{\text{exp}} = 0.22\%$. The difference in measured and simulated values can be explained by misalignment of the dipole with the cavity field, i.e. $\xi < 1$. We calculated $\beta$ as a function of the GeV center position in the diamond membrane for different dipole orientation, see figure 4.20. Here we show the expected position of the GeV center, which was $125 \pm 20$nm. It is seen that $\beta$ has a strong dependency on both the orientation of the dipole and the position of the GeV center. The measured $\beta_{\text{exp}}$ was in the low end of the expected

values. However, the position of the GeV center and the dipole orientation can explain why we measured a low $\beta$ value.

| $\gamma_r$ | $\gamma^\star$ | $\kappa$ | $g_{\mathrm{ZPL}}$ | $R_{\mathrm{ZPL}}$ |
|---|---|---|---|---|
| $2\pi \times 0.8$ MHz | $2\pi \times 5.21$ THz | $2\pi \times 1.1$ GHz | $2\pi \times 162$ MHz | $2\pi \times 20.3$ kHz |

Table 4.8: Cavity QED parameters for the GeV center in our cavity.

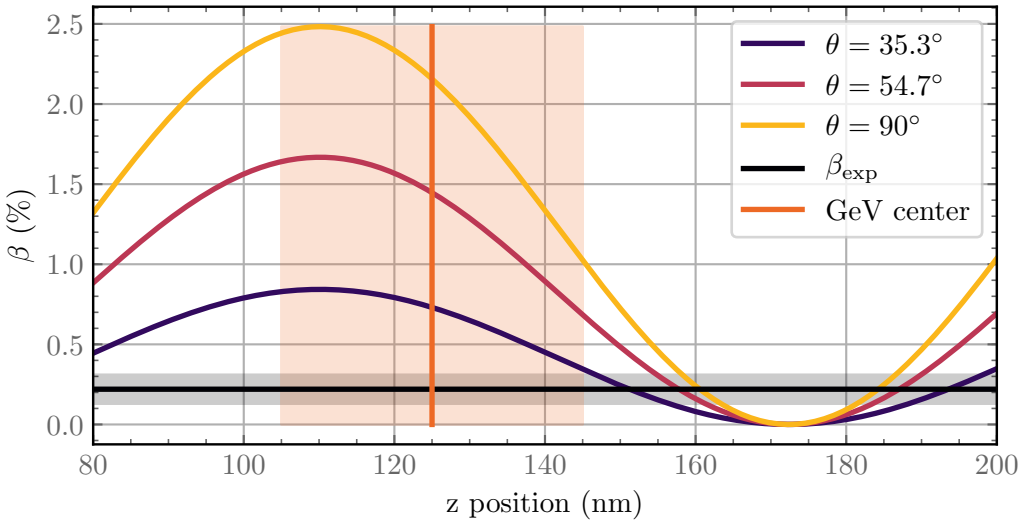


Figure 4.20: Calculated $\beta_{\mathrm{sim}}$ for different positions of the GeV center. Three different dipole orientations were calculated, where $\theta$ is the the dipole angle. An angle $\theta$ of 0° corresponds to a dipole normal to the (100) diamond surface and an angle of 90° corresponds to a dipole parallel with the (100) diamond surface. The cavity field orientation was assumed to be parallel with the diamond (100)-surface. The position of the GeV was implanted at a depth of $125 \pm 20$ nm. The measured values of $\beta_{\mathrm{exp}} = 0.22 \pm 0.09\%$ is shown in black.

We calculate the expected Purcell enhancement for a cryogenic temperature experiment with the same cavity:

$$F_p = \frac{3(\lambda/n_d)^3}{4\pi^2}\frac{Q}{V} = 200, \tag{4.32}$$

where we use the quality factor $Q = \frac{\omega}{\kappa}$. We can calculate the increase in the total decay rate of the GeV center at cryogenic temperatures:

$$\frac{\gamma_{\mathrm{tot}}}{\gamma_{\mathrm{free}}} = 1 + \eta_{\mathrm{QE}}\epsilon_{\mathrm{ZPL}}F_p = 4.6, \tag{4.33}$$

where we have used 0.03 for the quantum efficiency and 0.6 for the branching ratio into the ZPL $\epsilon_{\mathrm{ZPL}}$. This modest enhancement is mostly due to the small quantum efficiency. This can be compared to state of the art experiments for NV centers where an enhancement of 2 for the total decay rate has been observed [38].

# Chapter 5

# Conclusion and outlook

In this work we aimed to couple a single GeV center to an optical micro-cavity at room temperature to see cavity enhanced emission. We wanted to show the enhanced emission by comparing the emission from the same GeV center in and out of a micro-cavity. To quantify the interaction between the GeV center and the optical mode we measured the $\beta$-factor, which is the efficiency of the GeV emission into the cavity mode.

To achieve the above mentioned goals we built an optical micro-cavity consisting of one microscopic fiber mirror and one macroscopic flat mirror. This design of the micro-cavity was chosen such that a 860 nm thin diamond membrane could be incorporated in the cavity.

A concave mirror was fabricated on the end-facet of an SM fiber by laser ablation followed by dielectric coating. We achieved a short ROC of 38 µm, which was critical for achieving a small mode volume. The macroscopic mirror was also a DBR mirror, and the diamond membrane was bonded to the surface of the macroscopic DBR mirror. We used an electronic grade diamond, which was implanted with germanium ions and then thinned down to around ∼1 µm. Low surface roughness of 0.1 nm RMS at the diamond membrane was obtained.

We characterized the diamond membrane in the confocal microscope and found GeV centers in the diamond membrane. A single GeV center was characterized in detail using the confocal microscope, i.e. outside of the cavity. We found the excited state lifetime of the GeV center to be 6 ns and we found a ∼5 nm broad emission spectrum around ∼603 nm consistent with the literature. However, we observed modest count rates from the GeV center and we were unable to saturate many of them. The low count rates indicated a low quantum efficiency.
We made dipole simulations to calculate how much of the emission we collected and found that around ∼7% was collected by the microscope objective. Most of the light was guided in the diamond membrane and escaped at the edges.

A micro-cavity with the diamond membrane was built. Due to the low count rate from the GeV center a great effort was put into simply collecting a signal from the diamond membrane and we ended up filtering the signal in a narrow band around 600-605 nm. Unless the micro-cavity were on resonance with the GeV emission we could not collect any signal due to the high reflective mirrors. Due to fluorescence from the cavity fiber we had to collect the emission from the backside of the flat

mirror and not through the cavity.

A technique to take 3D scans was developed, where we scanned the cavity length for each lateral position. This was done to ensure that we were on resonance with the GeV emission and therefore could detect a signal. With these 3D scans we were able to find the same GeV center that we characterized out of the cavity.

We determined the cavity linewidth to 1.1 GHz at the position of the GeV center. Then, we characterized the emission spectrum and the emission rates from the GeV center in the micro-cavity. The GeV emission count rates was corrected by the collection efficiencies and compared to the emission rate out of the cavity. We found a spectral enhancement of 16, which clearly demonstrates coupling to the cavity. Furthermore, we measured the coupling efficiency to the cavity $\beta_{\text{exp}} = 0.22$, which was a bit lower than what we expected from the cavity parameter but this can be explained by sub-optimal angular and spatial overlap between the cavity mode and the GeV center.

We determined the expected Purcell enhancement to be 200 for the ZPL for future cryogenic experiments with a similar cavity. With a quantum efficiency of 3% we expect an overall change in spontaneous emission rate of 4.6, which is more than the current state of the art for NV centers where an overall change in spontaneous emission rate of 2 has been observed.
Going to cryogenic temperatures is necessary for achieving an efficient spin-photon interface. The work presented in this thesis provides insight and techniques that are useful for future micro-cavities experiments at cryogenic temperatures.
In this work we experimentally demonstrated the coupling of a single GeV center in a diamond membrane to a fiber-based optical micro-cavity at room temperature. This is the first demonstration of a single color center in a diamond membrane coupled to a fiber-based micro-cavity. It is also the first demonstration of a single GeV center coupled to a micro-cavity.

As a part of the efforts from the Center for Macroscopic Quantum States (bigQ) this work has taken important steps towards the aim of understanding and building quantum technologies with macroscopic quantum states.

# Bibliography


[1] EU Quantum Flagship. *Quantum Technology | The future is Quantum*. 2018. URL: https://qt.eu/ (visited on 01/04/2019).

[2] J. I. Cirac et al. "Quantum State Transfer and Entanglement Distribution among Distant Nodes in a Quantum Network". In: *Physical Review Letters* 78.16 (1997), pp. 3221–3224. ISSN: 0031-9007. DOI: 10.1103/PhysRevLett.78.3221. arXiv: 9611017 [quant-ph]. URL: https://link.aps.org/doi/10.1103/PhysRevLett.78.3221.

[3] H. J. Kimble. "The quantum internet". In: *Nature* 453.7198 (2008), pp. 1023–1030. ISSN: 14764687. DOI: 10.1038/nature07127. arXiv: 0806.4195.

[4] Stephanie Wehner, David Elkouss, and Ronald Hanson. "Quantum internet: A vision for the road ahead". In: *Science* 362.6412 (2018), eaam9288. ISSN: 0036-8075. DOI: 10.1126/science.aam9288. URL: http://www.sciencemag.org/lookup/doi/10.1126/science.aam9288.

[5] Kae Nemoto et al. "Photonic Architecture for Scalable Quantum Information Processing in Diamond". In: *Physical Review X* 4.3 (2014), p. 031022. ISSN: 2160-3308. DOI: 10.1103/PhysRevX.4.031022. URL: https://journals.aps.org/prx/pdf/10.1103/PhysRevX.4.031022https://link.aps.org/doi/10.1103/PhysRevX.4.031022.

[6] Valerio Scarani et al. "The security of practical quantum key distribution". In: *Reviews of Modern Physics* 81.3 (2009), pp. 1301–1350. ISSN: 0034-6861. DOI: 10.1103/RevModPhys.81.1301. URL: https://link.aps.org/doi/10.1103/RevModPhys.81.1301.

[7] P. Kómár et al. "A quantum network of clocks". In: *Nature Physics* 10.8 (2014), pp. 582–587. ISSN: 1745-2473. DOI: 10.1038/nphys3000. URL: http://www.nature.com/articles/nphys3000.

[8] T D Ladd et al. "Quantum computers". In: *Nature* 464.7285 (2010), pp. 45–53. ISSN: 0028-0836. DOI: 10.1038/nature08812. URL: http://www.nature.com/articles/nature08812.

[9] David P Divincenzo. *The Physical Implementation of Quantum Computation*. Tech. rep. 2000. URL: https://arxiv.org/pdf/quant-ph/0002077.pdf.

[10] F Jelezko et al. "Observation of Coherent Oscillation of a Single Nuclear Spin and Realization of a Two-Qubit Conditional Quantum Gate". In: *Physical Review Letters* 93.13 (2004), p. 130501. ISSN: 0031-9007. DOI: 10.1103/PhysRevLett.93.130501. URL: https://link.aps.org/doi/10.1103/PhysRevLett.93.130501.

[11] P. C. Maurer et al. “Room-Temperature Quantum Bit Memory Exceeding One Second”. In: *Science* 336.6086 (2012), pp. 1283–1286. ISSN: 0036-8075. DOI: 10.1126/science.1220513. arXiv: 1202.4379v1. URL: http://arxiv.org/abs/arXiv:1202.4379v1http://www.sciencemag.org/cgi/doi/10.1126/science.1220513.

[12] Lucio Robledo et al. “High-fidelity projective read-out of a solid-state spin quantum register”. In: *Nature* 477.7366 (2011), pp. 574–578. ISSN: 0028-0836. DOI: 10.1038/nature10401. URL: http://www.nature.com/articles/nature10401.

[13] E Togan et al. “Quantum entanglement between an optical photon and a solid-state spin qubit”. In: *Nature* 466.7307 (2010), pp. 730–734. ISSN: 0028-0836. DOI: 10.1038/nature09256. URL: http://www.nature.com/articles/nature09256.

[14] B Hensen et al. “Loophole-free Bell inequality violation using electron spins separated by 1.3 kilometres”. In: *Nature* 526.7575 (2015), pp. 682–686. ISSN: 0028-0836. DOI: 10.1038/nature15759. URL: http://www.nature.com/articles/nature15759.

[15] Peter C Humphreys et al. “Deterministic delivery of remote entanglement on a quantum network”. In: *Nature* 558.7709 (2018), pp. 268–273. ISSN: 0028-0836. DOI: 10.1038/s41586-018-0200-5. URL: http://www.nature.com/articles/s41586-018-0200-5.

[16] D. D. Sukachev et al. “Silicon-Vacancy Spin Qubit in Diamond: A Quantum Memory Exceeding 10 ms with Single-Shot State Readout”. In: *Physical Review Letters* 119.22 (2017), p. 223602. ISSN: 0031-9007. DOI: 10.1103/PhysRevLett.119.223602. arXiv: 1708.08852. URL: https://link.aps.org/doi/10.1103/PhysRevLett.119.223602.

[17] Petr Siyushev et al. “Optical and microwave control of germanium-vacancy center spins in diamond”. In: *Physical Review B* 96.8 (2017), pp. 1–5. ISSN: 24699969. DOI: 10.1103/PhysRevB.96.081201. arXiv: 1612.02947.

[18] Kerry J Vahala. “Optical microcavities”. In: *Nature* 424.6950 (2003), pp. 839–846. ISSN: 0028-0836. DOI: 10.1038/nature01939. URL: http://www.nature.com/articles/nature01939.

[19] E. M. Purcell. “Spontaneous Emission Probabliities at Radio Frquencies”. In: *Physical Review* 69 (1946), p. 681.

[20] Andrei Faraon et al. “Resonant enhancement of the zero-phonon emission from a colour centre in a diamond cavity”. In: *Nature Photonics* 5.5 (2011), pp. 301–305. ISSN: 1749-4885. DOI: 10.1038/nphoton.2011.52. URL: http://www.nature.com/articles/nphoton.2011.52.

[21] B J M Hausmann et al. “Coupling of NV Centers to Photonic Crystal Nanobeams in Diamond”. In: *Nano Letters* 13.12 (2013), pp. 5791–5796. ISSN: 1530-6984. DOI: 10.1021/nl402174g. URL: http://pubs.acs.org/doi/10.1021/nl402174g.

[22] Andrei Faraon et al. “Coupling of Nitrogen-Vacancy Centers to Photonic Crystal Cavities in Monocrystalline Diamond”. In: *Physical Review Letters* 109.3 (2012), p. 033604. ISSN: 0031-9007. DOI: 10.1103/PhysRevLett.109.033604. URL: https://link.aps.org/doi/10.1103/PhysRevLett.109.033604.

[23] Luozhou Li et al. “Coherent spin control of a nanocavity-enhanced qubit in diamond”. In: *Nature Communications* 6.1 (2015), p. 6173. ISSN: 2041-1723. DOI: 10.1038/ncomms7173. URL: http://www.nature.com/articles/ncomms7173.

[24] V. M. Acosta et al. “Dynamic Stabilization of the Optical Resonances of Single Nitrogen-Vacancy Centers in Diamond”. In: *Physical Review Letters* 108.20 (2012), p. 206401. ISSN: 0031-9007. DOI: 10.1103/PhysRevLett.108.206401. arXiv: 1112.5490. URL: https://link.aps.org/doi/10.1103/PhysRevLett.108.206401.

[25] Y Chu et al. “Coherent Optical Transitions in Implanted Nitrogen Vacancy Centers”. In: *Nano Letters* 14.4 (2014), pp. 1982–1986. DOI: 10.1021/nl404836p. URL: https://doi.org/10.1021/nl404836p.

[26] M. Trupke et al. “Microfabricated high-finesse optical cavity with open access and small volume”. In: *Applied Physics Letters* 87.21 (2005), p. 211106. ISSN: 0003-6951. DOI: 10.1063/1.2132066. URL: http://aip.scitation.org/doi/10.1063/1.2132066.

[27] T. Steinmetz et al. “Stable fiber-based Fabry-Pérot cavity”. In: *Applied Physics Letters* 89.11 (2006), pp. 1–4. ISSN: 00036951. DOI: 10.1063/1.2347892. arXiv: 0606231v1 [arXiv:physics].

[28] Philip R Dolan et al. “Femtoliter tunable optical cavity arrays.” In: *Optics letters* 35.21 (2010), pp. 3556–3558. ISSN: 0146-9592. DOI: 10.1364/OL.35.003556.

[29] D. Hunger et al. “A fiber Fabry-Perot cavity with high finesse”. In: *New Journal of Physics* 12 (2010). ISSN: 13672630. DOI: 10.1088/1367-2630/12/6/065038. arXiv: 1005.0067.

[30] D. Hunger et al. “Laser micro-fabrication of concave, low-roughness features in silica”. In: *AIP Advances* 2.1 (2012), p. 012119. ISSN: 2158-3226. DOI: 10.1063/1.3679721. arXiv: 1109.5047. URL: http://aip.scitation.org/doi/10.1063/1.3679721.

[31] Roland Albrecht et al. “Coupling of a Single Nitrogen-Vacancy Center in Diamond to a Fiber-Based Microcavity”. In: *Physical Review Letters* 110.24 (2013), p. 243602. ISSN: 0031-9007. DOI: 10.1103/PhysRevLett.110.243602. arXiv: 1303.7418. URL: http://arxiv.org/abs/1303.7418http://dx.doi.org/10.1103/PhysRevLett.110.243602https://link.aps.org/doi/10.1103/PhysRevLett.110.243602.

[32] Hanno Kaupp et al. “Scaling laws of the cavity enhancement for nitrogen-vacancy centers in diamond”. In: *Physical Review A - Atomic, Molecular, and Optical Physics* 88.5 (2013), pp. 1–9. ISSN: 10502947. DOI: 10.1103/PhysRevA.88.053812. arXiv: 1304.0948.

[33] S. Johnson et al. “Tunable cavity coupling of the zero phonon line of a nitrogen-vacancy defect in diamond”. In: *New Journal of Physics* 17.12 (2015), p. 122003. ISSN: 1367-2630. DOI: 10.1088/1367-2630/17/12/122003. arXiv: 1506.05161. URL: http://stacks.iop.org/1367-2630/17/i=12/a=122003?key=crossref.eb189333211e426b97a29b65684d0b7b.

[34] Hanno Kaupp et al. “Purcell-Enhanced Single-Photon Emission from Nitrogen-Vacancy Centers Coupled to a Tunable Microcavity”. In: *Physical Review Applied* 6.5 (2016), p. 054010. ISSN: 2331-7019. DOI: 10.1103/PhysRevApplied.6.054010. arXiv: 1606.00167. URL: https://link.aps.org/doi/10.1103/PhysRevApplied.6.054010.

[35] Julia Benedikter et al. “Cavity-Enhanced Single-Photon Source Based on the Silicon-Vacancy Center in Diamond”. In: *Physical Review Applied* 024031 (2017), pp. 1–12. ISSN: 2331-7019. DOI: 10.1103/PhysRevApplied.7.024031. arXiv: 1612.05509. URL: http://arxiv.org/abs/1612.05509.

[36] Janik Wolters et al. “Ultrafast spectral diffusion measurement on nitrogen vacancy centers in nanodiamonds using correlation interferometry”. In: *Physical Review Letters* 110.2 (2012), p. 027401. ISSN: 0031-9007. DOI: 10.1103/PhysRevLett.110.027401. arXiv: 1206.0852. URL: http://arxiv.org/abs/1206.0852{\%}0Ahttp://dx.doi.org/10.1103/PhysRevLett.110.027401.

[37] Erika Janitz et al. “Fabry-Perot microcavity for diamond-based photonics”. In: *Physical Review A* 92.4 (2015), p. 043844. ISSN: 1050-2947. DOI: 10.1103/PhysRevA.92.043844. arXiv: 1508.06588. URL: http://arxiv.org/abs/1508.06588http://dx.doi.org/10.1103/PhysRevA.92.043844https://link.aps.org/doi/10.1103/PhysRevA.92.043844.

[38] Daniel Riedel et al. “Deterministic Enhancement of Coherent Photon Generation from a Nitrogen-Vacancy Center in Ultrapure Diamond”. In: *Physical Review X* 7.3 (2017), p. 031040. ISSN: 2160-3308. DOI: 10.1103/PhysRevX.7.031040. arXiv: 1703.00815. URL: http://arxiv.org/abs/1703.00815http://dx.doi.org/10.1103/PhysRevX.7.031040https://link.aps.org/doi/10.1103/PhysRevX.7.031040.

[39] Stefan Häußler et al. “Diamond photonics platform based on silicon vacancy centers in a single-crystal diamond membrane and a fiber cavity”. In: *Physical Review B* 99.16 (2019), p. 165310. ISSN: 2469-9950. DOI: 10.1103/PhysRevB.99.165310. arXiv: 1812.02426. URL: http://arxiv.org/abs/1812.02426http://dx.doi.org/10.1103/PhysRevB.99.165310https://link.aps.org/doi/10.1103/PhysRevB.99.165310.

[40] Stefan Bogdanović et al. “Robust nano-fabrication of an integrated platform for spin control in a tunable microcavity”. In: *Citation: APL Photonics* 2 (2017), p. 126101. DOI: 10.1063/1.5001144. URL: http://aip.scitation.org/toc/app/2/12http://creativecommons.org/licenses/by/4.0/.

[41] Johannes F. S. Brachmann et al. “Photothermal effects in ultra-precisely stabilized tunable microcavities”. In: *Optics Express* 24.18 (2016), p. 21205. ISSN: 1094-4087. DOI: 10.1364/OE.24.021205. URL: https://www.osapublishing.org/abstract.cfm?URI=oe-24-18-21205.

[42] Jose Gallego et al. “High Finesse Fiber Fabry-Perot Cavities: Stabilization and Mode Matching Analysis”. In: *arXiv:1508.05289 [physics, physics:quant-ph]* (2015). DOI: 10.1007/s00340-015-6281-z. arXiv: 1508.05289. URL: http://arxiv.org/abs/1508.05289http://www.arxiv.org/pdf/1508.05289.pdf.

[43] Erika Janitz et al. “High mechanical bandwidth fiber-coupled Fabry-Perot cavity”. In: *Optics Express* 25.17 (2017), p. 20932. ISSN: 1094-4087. DOI: 10.1364/OE.25.020932. arXiv: arXiv:1703.00815. URL: https://www.osapublishing.org/abstract.cfm?URI=oe-25-17-20932.

[44] Jörg Wrachtrup and Fedor Jelezko. "Processing quantum information in diamond". In: *Journal of Physics: Condensed Matter* 18.21 (2006), S807–S824. ISSN: 0953-8984. DOI: 10.1088/0953-8984/18/21/S08. URL: http://stacks.iop.org/0953-8984/18/i=21/a=S08?key=crossref.3ebf978682f06b8bfab48217febea4e1.

[45] Gopalakrishnan Balasubramanian et al. "Nanoscale imaging magnetometry with diamond spins under ambient conditions". In: *Nature* 455.7213 (2008), pp. 648–651. ISSN: 0028-0836. DOI: 10.1038/nature07278. URL: http://www.nature.com/doifinder/10.1038/nature07278.

[46] L Rondin et al. "Magnetometry with nitrogen-vacancy defects in diamond". In: *Reports on Progress in Physics* 77.5 (2014), p. 056503. ISSN: 0034-4885. DOI: 10.1088/0034-4885/77/5/056503. URL: http://stacks.iop.org/0034-4885/77/i=5/a=056503?key=crossref.046a2a081f34fe0bfdbe8a0f7ad27a35.

[47] Sepehr Ahmadi et al. "Pump-Enhanced Continuous-Wave Magnetometry Using Nitrogen-Vacancy Ensembles". In: *Physical Review Applied* 8.3 (2017), p. 034001. ISSN: 2331-7019. DOI: 10.1103/PhysRevApplied.8.034001. URL: https://link.aps.org/doi/10.1103/PhysRevApplied.8.034001.

[48] J R Maze et al. "Properties of nitrogen-vacancy centers in diamond: the group theoretic approach". In: *New Journal of Physics* 13.2 (2011), p. 025025. ISSN: 1367-2630. DOI: 10.1088/1367-2630/13/2/025025. URL: http://stacks.iop.org/1367-2630/13/i=2/a=025025?key=crossref.8ab36e601bb08ebf4241a2745f14eb4d.

[49] G D Fuchs et al. "Excited-State Spectroscopy Using Single Spin Manipulation in Diamond". In: *Physical Review Letters* 101.11 (2008), p. 117601. ISSN: 0031-9007. DOI: 10.1103/PhysRevLett.101.117601. URL: https://journals-aps-org.proxy.findit.dtu.dk/prl/pdf/10.1103/PhysRevLett.101.117601https://link.aps.org/doi/10.1103/PhysRevLett.101.117601.

[50] L J Rogers et al. "Time-averaging within the excited state of the nitrogen-vacancy centre in diamond". In: *New Journal of Physics* 11.6 (2009), p. 063007. ISSN: 1367-2630. DOI: 10.1088/1367-2630/11/6/063007. URL: http://www.njp.org/http://stacks.iop.org/1367-2630/11/i=6/a=063007?key=crossref.511dc9aa245243a00e9079691d4b7577.

[51] Marcus W Doherty et al. "The nitrogen-vacancy colour centre in diamond". In: *Physics Reports* 528 (2013), pp. 1–45. DOI: 10.1016/j.physrep.2013.02.001. URL: http://dx.doi.org/10.1016/j.physrep.2013.02.001.

[52] L J Rogers et al. "Infrared emission of the NV centre in diamond: Zeeman and uniaxial stress studies". In: *New Journal of Physics* 10.10 (2008), p. 103024. ISSN: 1367-2630. DOI: 10.1088/1367-2630/10/10/103024. URL: http://stacks.iop.org/1367-2630/10/i=10/a=103024?key=crossref.647545a2e6145b776ed355e5ecaff205.

[53] F Jelezko et al. "Observation of Coherent Oscillations in a Single Electron Spin". In: *Physical Review Letters* 92.7 (2004), p. 076401. ISSN: 0031-9007. DOI: 10.1103/PhysRevLett.92.076401. URL: https://journals-aps-org.proxy.findit.dtu.dk/prl/pdf/10.1103/PhysRevLett.92.076401https://link.aps.org/doi/10.1103/PhysRevLett.92.076401.

[54] Gopalakrishnan Balasubramanian et al. "Ultralong spin coherence time in isotopically engineered diamond". In: *Nature Materials* 8 (2009), p. 14. DOI: 10.1038/NMAT2420. URL: www.nature.com/naturematerials.

[55] C Santori et al. “Nanophotonics for quantum optics using nitrogen-vacancy centers in diamond Related content Nanophotonics for quantum optics using nitrogen-vacancy centers in diamond”. In: *NANOTECHNOLOGY* 21 (2010), pp. 274008–274019. DOI: 10.1088/0957-4484/21/27/274008. URL: https://iopscience-iop-org.proxy.findit.dtu.dk/article/10.1088/0957-4484/21/27/274008/pdf.

[56] A Batalov et al. “Temporal Coherence of Photons Emitted by Single Nitrogen-Vacancy Defect Centers in Diamond Using Optical Rabi-Oscillations”. In: *Physical Review Letters* 100.7 (2008), p. 077401. ISSN: 0031-9007. DOI: 10.1103/PhysRevLett.100.077401. URL: https://journals-aps-org.proxy.findit.dtu.dk/prl/pdf/10.1103/PhysRevLett.100.077401https://link.aps.org/doi/10.1103/PhysRevLett.100.077401.

[57] Ilya P. Radko. “Determining the internal quantum efficiency of shallow-implanted nitrogen-vacancy defects in bulk diamond”. In: *Optics Express* 24.24 (2016), pp. 644–647. arXiv: arXiv:0906.3426.

[58] D Le Sage et al. “Efficient photon detection from color centers in a diamond optical waveguide”. In: *RAPID COMMUNICATIONS PHYSICAL REVIEW B* 85.4 (2012), pp. 121202–121203. DOI: 10.1103/PhysRevB.85.121202. URL: https://journals-aps-org.proxy.findit.dtu.dk/prb/pdf/10.1103/PhysRevB.85.121202.

[59] Jiabao Zheng et al. “Chirped circular dielectric gratings for near-unity collection efficiency from quantum emitters in bulk diamond”. In: *Optics Express* 25.26 (2017), p. 32420. ISSN: 1094-4087. DOI: 10.1364/OE.25.032420. URL: https://www.osapublishing.org/abstract.cfm?URI=oe-25-26-32420.

[60] Lachlan J Rogers et al. “Electronic structure of the negatively charged silicon-vacancy center in diamond”. In: *Physical Review B* 89.23 (2014), p. 235101. ISSN: 1098-0121. DOI: 10.1103/PhysRevB.89.235101. URL: https://link.aps.org/doi/10.1103/PhysRevB.89.235101.

[61] Takayuki Iwasaki et al. “Germanium-Vacancy Single Color Centers in Diamond”. In: *Scientific Reports* 5.1 (2015), p. 12882. ISSN: 2045-2322. DOI: 10.1038/srep12882. URL: http://www.nature.com/articles/srep12882.

[62] E. A. Ekimov et al. “Germanium–vacancy color center in isotopically enriched diamonds synthesized at high pressures”. In: *JETP Letters* 102.11 (2015), pp. 701–706. ISSN: 0021-3640. DOI: 10.1134/S0021364015230034. URL: http://link.springer.com/10.1134/S0021364015230034.

[63] Yuri N Palyanov et al. “Germanium : a new catalyst for diamond synthesis and a new optically active impurity in diamond”. In: *Nature Publishing Group* October (2015), pp. 1–8. DOI: 10.1038/srep14789. URL: http://dx.doi.org/10.1038/srep14789.

[64] A Sipahigil et al. “Indistinguishable Photons from Separated Silicon-Vacancy Centers in Diamond”. In: *Physical Review Letters* 113.11 (2014), p. 113602. ISSN: 0031-9007. DOI: 10.1103/PhysRevLett.113.113602. URL: https://link.aps.org/doi/10.1103/PhysRevLett.113.113602.

[65] M. K. Bhaskar et al. “Quantum Nonlinear Optics with a Germanium-Vacancy Color Center in a Nanoscale Diamond Waveguide”. In: *Physical Review Letters* 118.22 (2017), pp. 1–6. ISSN: 10797114. DOI: 10.1103/PhysRevLett.118.223603. arXiv: 1612.03036.

[66] Bahaa E A Saleh and Malvin Carl Teich. *Fundamentals of Photonics*. Second Edi. 2007. ISBN: 978-0-471-35832-9.

[67] Warren G. Nagourney. *Quantum Electronics for Atomic Physics and Telecommunication*. Oxford University Press, 2010.

[68] Charalambos C. Katsidis and Dimitrios I. Siapkas. "General transfer-matrix method for optical multilayer systems with coherent, partially coherent, and incoherent interference". In: *Applied Optics* 41.19 (2002), p. 3978. ISSN: 0003-6935. DOI: 10.1364/AO.41.003978. URL: https://www.osapublishing.org/abstract.cfm?URI=ao-41-19-3978http://ao.osa.org/abstract.cfm?URI=ao-41-19-3978.

[69] J. Szczyrbowski and A. Czapla. "Optical absorption in D.C. sputtered InAs films". In: *Thin Solid Films* 46.2 (1977), pp. 127–137. ISSN: 00406090. DOI: 10.1016/0040-6090(77)90055-4. URL: https://www.sciencedirect.com/science/article/pii/0040609077900554?via{\%}3Dihubhttp://www.sciencedirect.com/science/article/pii/0040609077900554http://linkinghub.elsevier.com/retrieve/pii/0040609077900554.

[70] Suzanne B van Dam, Maximilian Ruf, and Ronald Hanson. "Optimal design of diamond-air microcavities for quantum networks using an analytical approach". In: *New Journal of Physics* 20.11 (2018), p. 115004. ISSN: 1367-2630. DOI: 10.1088/1367-2630/aaec29. URL: http://stacks.iop.org/1367-2630/20/i=11/a=115004?key=crossref.399870c7b82403879b2c2ec2a6a8dcd5.

[71] Tobias Kippenberg. "Nonlinear Optics in Ultra-high-Q Whispering-Gallery Optical Microcavities". PhD thesis. California Institute of Technology, 2004.

[72] P. T. Kristensen, C. Van Vlack, and S. Hughes. "Generalized effective mode volume for leaky optical cavities". In: *Optics Letters* 37.10 (2012), p. 1649. ISSN: 0146-9592. DOI: 10.1364/OL.37.001649.

[73] Roland Albrecht. "Coupling of a Single Nitrogen-Vacancy Center in Diamond to a Fiber-based Microcavity". PhD thesis. Universität des Saarlandes, 2014.

[74] Daniel Riedel. "Engineering of the photonic environment of single nitrogen-vacancy centers in diamond". PhD thesis. University of Basel, 2017.

[75] Thomas Grange et al. "Cavity-Funneled Generation of Indistinguishable Single Photons from Strongly Dissipative Quantum Emitters". In: *Physical Review Letters* 114.19 (2015), pp. 1–5. ISSN: 10797114. DOI: 10.1103/PhysRevLett.114.193601. arXiv: 1501.00931.

[76] A Naesby et al. "Influence of pure dephasing on emission spectra from single photon sources". In: *Physical Review A* 78.4 (2008), p. 045802. ISSN: 1050-2947. DOI: 10.1103/PhysRevA.78.045802. URL: https://journals-aps-org.proxy.findit.dtu.dk/pra/pdf/10.1103/PhysRevA.78.045802https://link.aps.org/doi/10.1103/PhysRevA.78.045802.

[77] W Lukosz and R E Kunz. "Light emission by magnetic and electric dipoles close to a plane interface I Total radiated power". In: *Journal of the Optical Society of America* 67.12 (1977), p. 1607. ISSN: 0030-3941. DOI: 10.1364/JOSA.67.001607. URL: https://www.osapublishing.org/abstract.cfm?URI=josa-67-12-1607.

[78] Kristiaan A. Neyts. “Simulation of light emission from thin-film microcavities”. In: *Journal of the Optical Society of America A* 15.4 (1998), p. 962. ISSN: 1084-7529. DOI: 10.1364/JOSAA.15.000962. URL: https://www.osapublishing.org/abstract.cfm?URI=josaa-15-4-962.

[79] Daniel Najer et al. “Fabrication of mirror templates in silica with micron-sized radii of curvature”. In: *Applied Physics Letters* 110.1 (2017), pp. 1–6. ISSN: 00036951. DOI: 10.1063/1.4973458. arXiv: 1608.04527.

[80] Maximilian Ruf. “Fiber-based Fabry-Perot Microcavities”. Master Thesis. McGill Unversity, Canada, 2016.

[81] B. Brandstätter et al. “Integrated fiber-mirror ion trap for strong ion-cavity coupling”. In: *Review of Scientific Instruments* 84.12 (2013), p. 123104. ISSN: 0034-6748. DOI: 10.1063/1.4838696. arXiv: arXiv:1311.6961v1. URL: http://dx.doi.org/10.1063/1.4838696]http://aip.scitation.org/doi/10.1063/1.4838696.

[82] Birgit J M Hausmann et al. “Integrated Diamond Networks for Quantum Nanophotonics”. In: *Nano Letters* 12.3 (2012), pp. 1578–1582. DOI: 10.1021/nl204449n. URL: https://doi.org/10.1021/nl204449n.

[83] Pawel Latawiec et al. “On-chip diamond Raman laser”. In: *Optica* 2.11 (2015), pp. 924–928. DOI: 10.1364/OPTICA.2.000924. URL: http://www.osapublishing.org/optica/abstract.cfm?URI=optica-2-11-924.

[84] Patrick Appel et al. “Fabrication of all diamond scanning probes for nanoscale magnetometry”. In: *Review of Scientific Instruments* 87.6 (2016), p. 063703. ISSN: 0034-6748. DOI: 10.1063/1.4952953. URL: https://doi.org/10.1063/1.4952953http://aip.scitation.org/doi/10.1063/1.4952953.

[85] James Ziegler. *SRIM*. 2013. URL: http://www.srim.org/ (visited on 03/10/2019).

[86] Jan M. Binder et al. “Qudi: A modular python suite for experiment control and data processing”. In: *SoftwareX* 6 (2017), pp. 85–90. ISSN: 2352-7110. DOI: 10.1016/J.SOFTX.2017.02.001. URL: https://www.sciencedirect.com/science/article/pii/S2352711017300055.

[87] S. A. Solin and A. K. Ramdas. “Raman Spectrum of Diamond”. In: *Physical Review B* 1.4 (1970), pp. 1687–1698. ISSN: 0556-2805. DOI: 10.1103/PhysRevB.1.1687. URL: https://link.aps.org/doi/10.1103/PhysRevB.1.1687.

[88] Coastline. *homepage*. URL: http://www.coastlineoptics.com/ (visited on 04/04/2019).

[89] Laseroptik. *homepage*. URL: https://www.laseroptik.de/ (visited on 04/04/2019).

[90] Rosa Brouri et al. “Photon antibunching in the fluorescence of individual color centers in diamond”. In: *Optics Letters* 25.17 (2000), p. 1294. ISSN: 0146-9592. DOI: 10.1364/OL.25.001294. URL: https://www.osapublishing.org/abstract.cfm?URI=ol-25-17-1294.

[91] Disheng Chen et al. “Optical switching of resonance fluorescence from a single germanium vacancy color center in diamond”. In: (2019), pp. 1–8. arXiv: 1901.09231. URL: http://arxiv.org/abs/1901.09231.

[92] Alexia Auffèves, Jean Michel Gérard, and Jean Philippe Poizat. “Pure emitter dephasing: A resource for advanced solid-state single-photon sources”. In: *Physical Review A - Atomic, Molecular, and Optical Physics* 79.5 (2009), pp. 1–5. ISSN: 10502947. DOI: 10.1103/PhysRevA.79.053838. arXiv: 0808.0820.

[93] A. Auffèves et al. “Controlling the dynamics of a coupled atom-cavity system by pure dephasing”. In: *Physical Review B - Condensed Matter and Materials Physics* 81.24 (2010), pp. 1–10. ISSN: 10980121. DOI: 10.1103/PhysRevB.81.245419. arXiv: 1002.3753.

[94] K. N. Boldyrev et al. “Bright luminescence of diamonds with Ge-V centers”. In: *Journal of Luminescence* 193.May 2017 (2018), pp. 119–124. ISSN: 00222313. DOI: 10.1016/j.jlumin.2017.07.031. URL: http://dx.doi.org/10.1016/j.jlumin.2017.07.031.